# Dissertation

submitted to the
Combined Faculty of Mathematics, Engineering and Natural Sciences
of Heidelberg University, Germany
for the degree of

# Doctor of Natural Sciences

Put forward by


## Marcel Awenius

Born in: Munich, Germany


Oral examination: January 20$^{\text{th}}$, 2026

# Towards Highly-Accelerated Hyperpolarized $^{13}$C MRSI In Vivo: Advancing Radial EPSI as a Versatile Imaging Tool

Referees:
Prof. Dr. Mark E. Ladd
Prof. Dr. Leif Schröder

**Towards Highly-Accelerated Hyperpolarized $^{13}$C MRSI In Vivo: Advancing Radial EPSI as a Versatile Imaging Tool**

Hyperpolarized Carbon-13 magnetic resonance spectroscopic imaging ($^{13}$C MRSI) is a powerful technique for the in vivo investigation of metabolic processes in real-time.
The greatest challenge for tailored MRSI sequences is to acquire all three spatial dimensions together with full spectral information and in multiple timesteps, while being restricted in available acquisition time through rapid decay of the hyperpolarized state ($< 1$ minute).
In this work, advancements for radial echo-planar spectroscopic imaging (rEPSI) were implemented and optimized for various applications within the context of hyperpolarized $^{13}$C experiments in vivo on a clinical 3 T scanner.
Metabolic processes of hyperpolarized [1-$^{13}$C]pyruvate were monitored in vivo with high spatio-spectral resolution in just 6 seconds. A novel readout scheme with maximal $k$-space homogeneity successfully suppressed blurring due to the polarization decay and boosted the temporal resolution to the subsecond regime.
Further methodological advancements enabled the acquisition of spatially-resolved 3D in vivo spectra of hyperpolarized [1,2-$^{13}$C]pyruvate for the first time.
Moreover, a novel MR fingerprinting approach was developed using rEPSI for estimation of $B_1^+$ fields, enabling a pre-scan calibration for hyperpolarized $^{13}$C MRSI.
In conclusion, this thesis presents the developed advanced rEPSI as an effective and versatile imaging tool for hyperpolarized $^{13}$C MRSI, with enormous potential for substrates of high spectral complexity like [1,2-$^{13}$C]pyruvate.

**Hin zur hochbeschleunigten hyperpolarisierten $^{13}$C MRSI In Vivo: Weiterentwicklung radial-aufgenommener EPSI zu einer vielseitigen Bildaufnahmestrategie**

Die hyperpolarisierte Kohlenstoff-13-Magnetresonanzspektroskopie ($^{13}$C MRSI) ist ein mächtiges Verfahren zur Echtzeit-Untersuchung von Stoffwechselprozessen in vivo.
Die größte Herausforderung bei maßgeschneiderten MRSI-Sequenzen besteht darin, alle drei räumlichen Dimensionen zusammen mit vollständigen Spektralinformationen und in mehreren Zeitschritten zu erfassen, wobei die verfügbare Messzeit durch den schnellen Zerfall des hyperpolarisierten Zustands begrenzt ist ($<$ 1 Minute).
In dieser Arbeit wurde die radiale echo-planare spektroskopische Bildgebung (rEPSI) weiterentwickelt und für verschiedene Anwendungen im Zusammenhang mit hyperpolarisierten $^{13}$C-Experimenten in vivo auf einem klinischen 3-T-Scanner optimiert.
Die Stoffwechselprozesse von hyperpolarisiertem [1-$^{13}$C]Pyruvat wurden in vivo mit hoher räumlich-spektraler Auflösung in nur 6 Sekunden erfasst. Ein neuartiges Ausleseschema mit maximaler $k$-Raum-Homogenität unterdrückte erfolgreich die durch den Polarisationsabfall verursachte Unschärfe und steigerte die zeitlichen Auflösung bis in den Subsekundenbereich.
Weitere methodische Fortschritte ermöglichten erstmals die in-vivo-Erfassung räumlich aufgelöster Spektren von hyperpolarisiertem [1,2-$^{13}$C]Pyruvat in 3D.
Darüber hinaus wurde ein neuartiger MR-Fingerprinting-Ansatz zur Bemessung von $B_1^+$-Feldern durch die rEPSI entwickelt, welcher eine Kalibrierung vor der Messung für hyperpolarisierte $^{13}$C MRSI ermöglicht.
Zusammenfassend präsentiert diese Arbeit die Entwicklung einer fortschrittlichen rEPSI als eine effektive und vielseitige Bildaufnahmestrategie für hyperpolarisierte $^{13}$C MRSI mit enormem Potenzial für Substrate mit hoher spektraler Komplexität wie [1,2-$^{13}$C]Pyruvat.

# Contents

# Acronyms

**ALT** Alanine transaminase

**AUC** Area-under-the-curve

**bSSFP** Balanced steady-state free precession

**BW** Bandwidth

**CS** Compressed sensing

**CSI** Chemical shift imaging

**DA** Double-angle

**d-DNP** Dissolution dynamic nuclear polarization

**EG** Ethylene glycol

**EPI** Echo-planar imaging

**EPSI** Echo-planar spectroscopic imaging

**ETS** Echo-train-shifting

**FA** Flip angle

**FFT** Fast Fourier transformation

**FID** Free induction decay

**FOV** Field-of-view

**FT** Fourier transformation

**FWHM** Full width half maximum

**GAGA** Gapped arrangement of golden angles

**HP** Hyperpolarization

**LDH** Lactate dehydrogenase

**MR** Magnetic resonance

**MRI** Magnetic resonance imaging

**MRS** Magnetic resonance spectroscopy

**MRSI** Magnetic resonance spectroscopic imaging

**MRF** Magnetic resonance fingerprinting

**MS** Metabolite-specific

**MW** Microwave

**NA** Natural abundance

**NAD** Nicotinamide adenine dinucleotide

**NMR** Nuclear magnetic resonance

**PSF** Point spread function

**rEPSI** Radial echo-planar spectroscopic imaging

**RF** Radio frequency

**SNR** Signal-to-noise ratio

**SW** Sliding-window

**TA** Acquisition time

**TBW** Time-bandwidth product

**TR** Repetition time

**VFA** Variable flip angle

# 1. Introduction

Magnetic resonance imaging (MRI) is a major medical diagnostics tool used in hospitals worldwide. Its ability to non-invasively image soft tissues and provide additional information, like blood flow or metabolic activity, makes it a valuable modality for diagnostics of variable diseases [1].
MRI also shows how fundamental physical discoveries can aid our society, since this technique is based on the quantum-mechanical understanding of atomic nuclei and their macroscopic behavior in a magnetic field.

The journey through the history of medical physics leading to the development of MRI begins back in 1922. The foundation was laid by the Stern-Gerlach experiment, which revealed the quantization of the angular momentum for nuclei by the deflection of silver atoms within an inhomogeneous magnetic field [2]. About 15 years later, a transition between those angular momentum quantum states could be induced by application of an oscillating magnetic field to lithium chloride [3]. By finding the right oscillation frequency and observing resonance peaks specific for the used molecule, Rabi coined the term nuclear magnetic resonance (NMR). This cleared the path for the first demonstration of the NMR phenomenon in 1946 by Bloch and Purcell in solid state using paraffin and water, respectively [4,5]. Only four years after that, Proctor and Yu, as well as Dickson, noticed a dependency of the resonance frequency on the position of the nucleus within a molecule, known as the chemical shift [6,7]. This marked the birth of magnetic resonance spectroscopy (MRS), which nowadays enables the encoding of crucial in vivo information like pH or metabolic activity within the acquired temporal data [8]. In 1973, Lauterbur and Mansfield presented MRI as a method to acquire three-dimensional anatomical images by introducing magnetic field gradients to the experimental setup [9], finally making the NMR technique an indispensable tool in the field of medicine.

All of these historical milestones show the complexity of MRI and MRS, techniques that thrive on constant advancement, even until today. And invention and improvement of scanner hardware, acquisition schemes and contrast methods is still ongoing. The combination of magnetic resonance (MR) anatomical imaging and spectroscopic methods to MR spectroscopic imaging (MRSI) enables the localized investigation of metabolic activity, increasing its clinical value further and further [8].

A novel approach to investigate metabolism-altering diseases is the hyperpolarized MRI of the carbon nucleus ($^{13}$C), instead of the more commonly used hydrogen nucleus ($^{1}$H) [10]. The MR-sensitive isotope carbon-13 only shows a natural abundance of about 1%, therefore, allowing to track only certain metabolic pathways through $^{13}$C-enriched molecules of interest, with almost no background signal. However, this comes with the problem a of low concentration of the administered $^{13}$C-labels and lower inherent sensitivity of $^{13}$C compared to $^{1}$H, yielding only little signal to evaluate for $^{13}$C MRI. Yet, an application becomes feasible by either using highly concentrated model solutions or by introducing the so-called hyperpolarization (HP) technique [11].

The HP method used in this work is dissolution dynamic nuclear polarization (d-DNP), the theoretical principles of which were first postulated by Overhauser in 1952 [12]. It was experimentally proven one year later by Slater and Slichter [13], but only found its way into the clinical application within the last 20 years. d-DNP provides a signal enhancement of over 10,000 by exploiting the naturally higher sensitivity of electrons and transferring their polarization to the $^{13}$C nucleus [14]. HP allows to track $^{13}$C-labeled metabolites in vivo to assess their in-body distribution and also metabolic turnover in real-time. This enables not only the localization of a tumor but also the possibility to analyze its response to a therapy approach [15].

Technical challenges for the imaging modalities using hyperpolarized $^{13}$C are the non-recoverable hyperpolarized state, which decays within a few minutes through the molecule-specific relaxation processes, namely $T_1$ decay, demanding for a rapid encoding of all desired information, as well as a highly controlled usage of the available signal [16]. Typically employed MR sequences in the context of HP experiments are, for one, spectroscopic sequences, like slice-selective free induction decay (FID) spectroscopy [17] and chemical shift imaging (CSI) [18], which provide high spectral bandwidth (BW) and resolution, but either offer no spatial resolution or are very slow. Other approaches are metabolite-specific (MS) imaging sequences, like echo-planar imaging (EPI) with spectral-spatial radio-frequency (RF) pulses [19] and spectrally-selective balanced steady-state free precession (bSSFP) [20], which offer a good spatial resolution with additional spectral information. However, these MS approaches rely on prior knowledge of the expected resonances, as well as sparse, well-defined spectral peaks. For the acquisition, this means a high sensitivity to the correct adjustment of sequence parameters and inhomogeneities, and ultimately, the need for a more complex reconstruction algorithm.

In contrast, this work proposes a novel magnetic resonance spectroscopic imaging (MRSI) sequence for in vivo hyperpolarized $^{13}$C experiments, namely radial echo-planar spectroscopic imaging (rEPSI) [21], to not only efficiently encode for all three spatial dimensions but also capture the spectral domain with a high BW and resolution. rEPSI is presented as a valuable tool with enormous potential for HP $^{13}$C experiments, allowing to volumetrically evaluate several possible complex spectral settings, like capturing newly appearing resonances (e.g. through unknown metabolic conversions), varying position of peaks (e.g. through pH-induced chemical shift changes) or extremely complex spectral patterns (e.g. with [1,2-$^{13}$C]pyruvate or $^{13}$C lipid signals in the human brain).

The rEPSI sequence was additionally optimized to fit the specific needs of several experimental applications to demonstrate its adaptability as a spectroscopic imaging tool. Through its radial readout, this sequence is robust to undersampling, allowing for faster data acquisition compared to Cartesian spectroscopy sequences, an essential prerequisite in the context of time-sensitive HP measurements. An optimal undersampling threshold was determined to shorten the acquisition time without the use of any special advanced reconstruction algorithms.
Exploiting this compatibility to undersampling, a novel readout pattern, called gapped arrangement of golden angles (GAGA) [22], was designed to not only increase the homogeneity in $k$-space coverage, but also allow for the division of a fully sampled dataset into multiple subsets via the sliding window (SW) technique [23]. These additional frames enable the extraction of dynamic information, like $T_1$ decay or metabolic conversion, from the undersampled subsets, while still providing the fully sampled main dataset.
Additionally, further advanced features were implemented, like variable flip angle (VFA) schemes, which were applied to compensate for the continuous $T_1$ decay [24], in turn providing a steady signal amplitude throughout the acquisition, or to produce a $B_1^+$-sensitive signal evolution [25] for the investigation of the actual transmitted RF pulses.
Another implementation was echo-train-shifting (ETS) [26], which allows for even broader acquisition of the spectral BW without being hindered by hardware restrictions like the gradient strength.
Finally, the radial readout could be easily reordered for the usage of a magnetic resonance fingerprinting (MRF) algorithm [27], which, together with the VFA scheme, was applied to determine the actual transmitted $B_1^+$ field [28].

The spectral data in all applications was evaluated by an optimized pipeline of the individual $^{13}$C resonances via the AMARES fitting algorithm [29].

Furthermore, this thesis showcases applications of the radial echo-planar spectroscopic imaging (rEPSI) sequence to different settings of in vivo HP $^{13}$C experiments, as well as its usage in magnetic resonance fingerprinting (MRF). This demonstrates not only the versatility of the rEPSI method, but also the benefits of a detailed acquisition of spatially resolved high-quality spectral information.

First, in vivo HP measurements were conducted in rats, in which a dynamic series of eight consecutive timepoints was acquired, capturing the metabolic conversion of [1-$^{13}$C]pyruvate into [1-$^{13}$C]lactate and [1-$^{13}$C]alanine.
Subsequent SW reconstruction demonstrated the advantages of the optimally arranged radial readout by dividing each timepoint of the in vivo measurements into 40 smaller subframes.
Next, in vivo MRSI datasets were acquired using hyperpolarized [1,2-$^{13}$C]pyruvate, showing all expected resonances over a large BW of 2 kHz. To this end, ETS was employed to double the BW from native 1 kHz, while using the $T_1$-compensating VFA scheme to combine the respective radial acquisitions without $T_1$-related intensity variations, reducing potentially arising ghost artifacts.
Tracking metabolic conversion, lactate-to-pyruvate-ratio maps were obtained for tumor-bearing rats, before and several weeks after irradiation of the tumor to detect a possible metabolic change.
Lastly, $B_1^+$ mapping was achieved through MRF by applying a reordering of the radial readout together with the $B_1^+$-sensitive VFA scheme. Usage of the whole spectral BW enabled in vivo application, despite the extremely low signal-to-noise ratio (SNR) of brain lipids, while also making this mapping approach more robust. Herewith, a $B_1^+$ correction prior to HP scans is possible, ensuring the necessary optimal usage of the available signal through corrected RF excitations.

In summary, this work presents an advanced rEPSI sequence as an optimized tool for in vivo HP $^{13}$C experiments. The rEPSI provides a highly-accelerated acquisition of 4D datasets, adaptable for the use in several spectroscopically challenging settings.

# 2. Fundamentals

In order to understand all applied methods within this work, we need to dive deeper into the physical foundation that lays beneath the nuclear magnetic resonance (NMR) phenomenon, its application in spectroscopic imaging and so-called 'fingerprinting', as well as the quantum dynamics describing the hyperpolarization (HP) method.

## 2.1. Nuclear Magnetic Resonance

First, an understanding of magnetic resonance (MR) on an atomic level has to be built. In this section the physical properties of nuclear spins are described, as well as their macroscopic effect during NMR experiments. A more detailed description can be found in [13, 30].

### 2.1.1. Nuclear Spin

All matter consists of atoms, which themselves contain electrons and a nucleus. The basic description of NMR starts with an atomic nucleus and its components, namely protons and neutrons, which again consist of quarks and gluons. Depending on this internal arrangement, one can predict the energetically favorable nuclear spin $I$ from three possible cases for the number of protons and neutrons, respectively:

1. even-even: $I = 0$ (zero)
2. odd-odd: $I \in \mathbb{N}$ (full integers)
3. even-odd and odd-even: $I \in (\mathbb{N} - \frac{1}{2})$ (half integers)

$I$ is an intrinsic quantum mechanical property of a nucleus and shows the following eigenvalue equations for the spin eigenstates $|I, m\rangle$:

$$\hat{\vec{I}}^2 |I, m\rangle = \hbar^2 I(I+1) |I, m\rangle \tag{1}$$

$$\hat{I}_z |I, m\rangle = \hbar m |I, m\rangle \tag{2}$$

with the nuclear spin quantum number $m \in \{-I, -I+1, \ldots I-1, I\}$ and the reduced Planck constant $\hbar = \frac{h}{2\pi} \approx 1.05 \cdot 10^{-34}$ Js. The 'hat' notation ($\hat{}$) hereby indicates quantum mechanical operators.

The description of $I$ resembles the angular momentum in classical mechanics, but here only discrete quantum values are possible and no actual rotation is occurring. It also gives rise to the magnetic dipole moment $\mu$, which allows the description of the magnetic behavior of an atomic nucleus:

$$\vec{\mu} = \gamma \vec{I} \tag{3}$$

with $\gamma$ as the nucleus-specific gyromagnetic ratio.
The two investigated atomic nuclei of this thesis are hydrogen-1 ($^1$H) and carbon-13 ($^{13}$C), which are both spin-$\frac{1}{2}$ particles and posses the gyromagnetic ratios $\gamma_{1\mathrm{H}} \approx 42.58\ \frac{\mathrm{MHz}}{\mathrm{T}}$ and $\gamma_{13\mathrm{C}} \approx 10.71\ \frac{\mathrm{MHz}}{\mathrm{T}}$.

### 2.1.2. Zeeman Effect

The interaction of a magnetic dipole moment $\mu$ with a static magnetic field $B_0$ can be described by the Hamilton operator $\hat{H}$:

$$\hat{H} = -\hat{\vec{\mu}} \cdot \vec{B_0} \ . \tag{4}$$

Using $\hat{H}$ and the eigenvalue eq. (1), the energy eigenstates $E_m$ can be calculated for a magnetic field in $z$-direction $\vec{B_0} = (0, 0, B_0)$:

$$E_m = \langle I, m | \hat{H} | I, m \rangle = -m\hbar\gamma B_0 \ . \tag{5}$$

This splitting into $2I + 1$ energy levels, accounting for all possible values of $m$, is called Zeeman effect. For the case of $^1$H or $^{13}$C with a nuclear spin of $I = \frac{1}{2}$ only two eigenstates exist with the following energy difference $\Delta E$:

$$\Delta E = |E_{-\frac{1}{2}} - E_{\frac{1}{2}}| = \gamma\hbar B_0 \ . \tag{6}$$

A key property used in NMR to transition between those states is the Lamor frequency $\omega_0$:

$$\omega_0 = \frac{\Delta E}{\hbar} = \gamma B_0 \ . \tag{7}$$

### 2.1.3. Macroscopic Magnetization

For a large number $N$ of atomic nuclei in a volume $V$, the behavior of all spins can be described via a macroscopic quantity, called magnetization $M$:

$$\vec{M} = \frac{1}{V} \sum_{i=1}^{N} \langle \hat{\vec{\mu}} \rangle_i \, . \tag{8}$$

This formula defines $M$ as the sum over all expected values of magnetic dipole moments per volume. The expectation value can be calculated for a spin-$\frac{1}{2}$ particle via eq. (2) and (3):

$$\langle \hat{\vec{\mu}} \rangle = \left\langle \frac{1}{2}, \pm\frac{1}{2} \right| \gamma \hat{I}_z \left| \frac{1}{2}, \pm\frac{1}{2} \right\rangle = \pm\gamma\frac{\hbar}{2} \, . \tag{9}$$

Since a one-directional $B$ field is applied, only parallel $N_+$ and anti-parallel $N_-$ nuclear spins are possible for spin $\frac{1}{2}$ particles. These occupation numbers $N_\pm$ can then be calculated from the Boltzmann distribution:

$$N_\pm = N \cdot \frac{\exp(E_{\pm\frac{1}{2}}/k_B T)}{\sum_{m=-\frac{1}{2}}^{\frac{1}{2}} \exp(E_m/k_B T)} \tag{10}$$

which determines the probability of each possible state of energy $E_{\pm\frac{1}{2}}$ at a temperature $T$. The Boltzmann constant is $k_B = 1.38 \cdot 10^{-23} \frac{\mathrm{J}}{\mathrm{K}}$.
If eq. (9) and (10) are now inserted into eq. (8) and the summation simplified into the two possible occupation states $N_+$ and $N_-$, the magnetization can be reformulated and approximated to:

$$\vec{M} = \frac{1}{V}\left(N_+\left(+\frac{\gamma\hbar}{2}\right) + N_-\left(-\frac{\gamma\hbar}{2}\right)\right) \tag{11}$$

$$= \frac{1}{V}\frac{\gamma\hbar}{2}(N_+ - N_-) \tag{12}$$

$$= \frac{1}{V}\frac{\gamma\hbar}{2}\left(N \cdot \tanh\left(\frac{\gamma\hbar B_0}{2k_B T}\right)\right) \tag{13}$$

$$\approx \frac{N}{V}\frac{\gamma^2\hbar^2 B_0}{4k_B T} \, . \tag{14}$$

During the last approximation, it is assumed that $k_B T \gg \gamma\hbar B_0$ for the experimental parameters of $T \sim 300$ K and $B_0 = 3$ T. The macroscopic magnetization is therefore increasing proportionally to the concentration $\frac{N}{V}$, the squared gyromagnetic ratio $\gamma^2$ and the static magnetic field $B_0$ and anti-proportionally to the temperature $T$.

### 2.1.4. Magnetic Resonance

The motion of this magnetization vector can be described as a torque, which brings the transversal component in the $x$-$y$ plane to rotate around the external magnetic field $B_0$, and is calculated via their cross-product:

$$\frac{\mathrm{d}\vec{M}}{\mathrm{d}t} = \vec{M} \times \gamma \vec{B}_0 \, . \tag{15}$$

Without any external disturbance, $\vec{M}$ would be parallel to $\vec{B}_0$ and, hence, no motion occurs. However, now a second magnetic field $B_1$ in form of a radio frequency (RF) pulse is applied, which rotates in the transversal plane with the angular velocity $\omega_{\mathrm{RF}}$:

$$\vec{B}_1 = B_1 \begin{pmatrix} \cos(\omega_{\mathrm{RF}} t) \\ \sin(\omega_{\mathrm{RF}} t) \\ 0 \end{pmatrix} \, . \tag{16}$$

By transformation into the rotating reference frame of $\vec{B}_1$ ($\vec{M} \rightarrow \vec{M}'$), the equation of motion from eq. (15) is modulated to the following:

$$\frac{\mathrm{d}\vec{M}'}{\mathrm{d}t} = \vec{M}' \times \gamma \begin{pmatrix} B_1 \\ 0 \\ B_0 - \frac{\omega_{\mathrm{RF}}}{\gamma} \end{pmatrix} = \vec{M}' \times \gamma \vec{B}'_{\mathrm{eff}} \, . \tag{17}$$

$\vec{B}'_{\mathrm{eff}}$ denotes the new effective magnetic field. On-resonant, i.e. under the condition $\omega_{\mathrm{RF}} = \omega_0$, the magnetization only experiences the RF pulse $\vec{B}_1$, which tips the magnetization into the transversal plane. The flip angle (FA) $\alpha$, describing how far the magnetization vector is rotated into the $x$-$y$ plane, can be calculated as:

$$\alpha = \int_0^{t_p} \gamma B_1(t) \mathrm{d}t \tag{18}$$

where $0 \leqslant t \leqslant t_p$ is the time, in which the second magnetic field pulse with shape $B_1(t)$, later also called RF excitation pulse, is applied. Afterwards, the transversal component of $\vec{M}$ is rotating in the $x$-$y$ plane, as described by formula (15).

### 2.1.5. Bloch Equations

The last step to accurately describe an actual experiment are relaxation processes. These are differentiated into an energy exchange with the environment ('spin-lattice') and of the individual spins with one another ('spin-spin'), accompanied by the relaxation times $T_1$ and $T_2$, respectively.
Both processes are encapsulated in the so-called Bloch equations, which are expansions of eq. (15):

$$\frac{\mathrm{d}M_x(t)}{\mathrm{d}t} = (\vec{M} \times \gamma\vec{B})_x - \frac{M_x(t)}{T_2} \tag{19}$$

$$\frac{\mathrm{d}M_y(t)}{\mathrm{d}t} = (\vec{M} \times \gamma\vec{B})_y - \frac{M_y(t)}{T_2} \tag{20}$$

$$\frac{\mathrm{d}M_z(t)}{\mathrm{d}t} = (\vec{M} \times \gamma\vec{B})_z - \frac{M_z(t) - M_0}{T_1} \ . \tag{21}$$

Hereby, $M_0$ represents the ground state magnetization, i.e. the full magnetization $\vec{M}$ aligned along $B_0$.
When these equations are again brought into a rotating frame of reference, they provide the following description:

$$\frac{\mathrm{d}M'_x(t)}{\mathrm{d}t} = -\frac{M'_x(t)}{T_2} + (\omega_0 - \omega)M'_y(t) \tag{22}$$

$$\frac{\mathrm{d}M'_y(t)}{\mathrm{d}t} = -\frac{M'_y(t)}{T_2} - (\omega_0 - \omega)M'_x(t) + \gamma B_1 M'_z(t) \tag{23}$$

$$\frac{\mathrm{d}M'_z(t)}{\mathrm{d}t} = -\frac{M'_z(t) - M_0}{T_1} - \gamma B_1 M'_y(t) \ . \tag{24}$$

Now, the effects of precession, relaxation and excitation can be described in one set of formulas. For the $x'$-component, the amplitude exponentially decays with $T_2$ and increases with the rotation of the $y'$-component within the $x'$-$y'$-plane. Similar for the $y'$-component, where $T_2$ decay and decrease with rotating $x'$-component occur. Additionally, there is an influx via the RF excitation pulse $B_1$, which rotates the $z'$-component into the $y'$-direction. Lastly, the $z'$-component recovers to the ground state with an exponential annealing curve from $-M_0$ to $M_0$, while getting smaller due to the $B_1$-based rotation into the $y'$-component.

## 2.2. Magnetic Resonance Spectroscopic Imaging

In this section, the basic components of MR sequences, like RF excitation pulses, magnetic field gradients as well as the data acquisition, are defined. This work focuses on magnetic resonance spectroscopic imaging (MRSI) sequences, which are used to encode spectral and spatial information simultaneously. For a more in depth explanation of the topic, the reader is referred to [8].

### 2.2.1. Free Induction Decay

The simplest MR sequence just consists of an RF excitation pulse, followed by a readout, i.e. the electronic data acquisition. The resulting signal is described via the solution of the Bloch equations and can be divided into the transversal $M_\perp$ and longitudinal magnetization $M_\parallel$:

$$M_\perp(t) = M_x(t) + iM_y(t) = M_\perp(0)e^{-\frac{t}{T_2^*}} \tag{25}$$

$$M_\parallel(t) = M_z(t) \qquad = M_0 - (M_0 - M_z(0))e^{-\frac{t}{T_1}} \ . \tag{26}$$

The evolution of $M_\perp$ is governed by the $T_2^*$ decay, which extends the $T_2$ relaxation constant by inhomogeneities of the external magnetic field $\Delta B_0$ within the observed volume:

$$\frac{1}{T_2^*} = \frac{1}{T_2} + \gamma \Delta B_0 \ . \tag{27}$$

Therefore, higher inhomogeneities $\Delta B_0$ increase the transversal relaxation. This effect arises from the associated Larmor frequencies (eq. 7), which result in different local precession frequencies and ultimately cause a dephasing of the transversal spins.
It can be noticed that equilibrium state is reached when $M_\parallel$ is recovered to the full initial amplitude of $M_0$, and $M_\perp$ fully decays to zero. During the transversal decay, $M_\perp$ precesses in the $x$-$y$ plane and hereby induces an alternating current in a coil, as stated by Faraday's law. The acquired signal $S$ is equal to this induced voltage $U_{\text{ind}}$ and depends on the density of spins $\rho(\vec{r})$ within the excited volume:

$$U_{\text{ind}}(t) = S(t) = S(0)\, e^{i\omega_0 t} e^{-\frac{t}{T_2^*}} \tag{28}$$

$$S(0) \propto \int \rho(\vec{r}) \mathrm{d}V \tag{29}$$

This time evolution is called free induction decay (FID) and is processed by the electronic data acquisition as complex data, corresponding to $M_\perp = M_x + iM_y$. The covered bandwidth (BW) of the acquisition is defined by the sampling intervals of the $T_2^*$ decay, also called dwell time $t_\mathrm{d}$:

$$\mathrm{BW} = \frac{1}{t_\mathrm{d}} \,. \tag{30}$$

The spectral resolution $R_\mathrm{spec}$ then simply results from the number of points $N_t$ acquired over time.

$$R_\mathrm{spec} = \frac{\mathrm{BW}}{N_t} = \frac{1}{\mathrm{TA}} \,. \tag{31}$$

The total acquisition time (TA) can be calculated by multiplying the dwell time $t_d$ by $N_t$.

The final NMR spectrum can be calculated by applying a Fourier transform (FT) to eq. (28). The resulting spectral peak is located at the corresponding Larmor frequency $\omega_0$ and has a Lorentzian peak shape with a full width half maximum (FWHM) of:

$$\mathrm{FWHM} = \frac{2}{T_2^*} \,. \tag{32}$$

Figure 1 displays the FID shape in time as well as frequency domain. Moreover, the influence of all constituents of the initial signal $S(t)$ are indicated, together with their influence to the final peak shape.

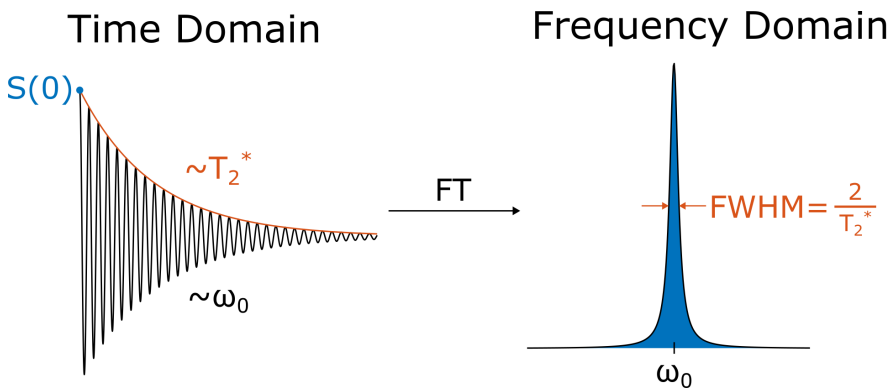


Figure 1: Visualization of the Fourier transformation (FT) of the free induction decay (FID). The acquired time domain signal $S(t)$ is defined by the amplitude $S(0)$, the oscillation frequency $\omega_0$ as well as the decay constant $T_2^*$. After FT into the frequency domain, the signal shows a Lorentzian peak shape. The area under the peak is defined by $S(0)$, the position along the frequency axis by $\omega_0$ and, finally, the peak width by $T_2^*$.

### 2.2.2. Chemical Shift

Using the FID, the molecular structure of a substance can be probed, since the local electronic environment depends on the position of the investigated nuclei within a molecule. With electrons being moving charges, they also generate a magnetic field that changes the local field, affecting the nuclei by a small amount $\delta\vec{B}$, which is described via the magnetic shielding $\sigma$ for a certain nucleus $i$:

$$\delta\vec{B} = -\sigma_i\vec{B_0} \; . \tag{33}$$

This, in turn, results in a small change in the Larmor frequency, which is specific for the chemical environment:

$$\omega_i = \omega_0(1 - \sigma_i) \; . \tag{34}$$

The used unit of comparison is called chemical shift $\delta$ in parts per million (ppm), which defines this new shifted frequency relative to a general reference frequency:

$$\delta_i = (\sigma_{ref} - \sigma_i) \times 10^6 \tag{35}$$

$$= \frac{\omega_i - \omega_{ref}}{\omega_{ref}} \times 10^6 \; . \tag{36}$$

Since $\delta$ is independent of $B_0$, a comparison between set-ups of different magnetic field strength is easier.

### 2.2.3. *J*-Coupling

For the case of two nuclei within one molecule, a scalar coupling of their spins $\hat{I}_1$ and $\hat{I}_2$ can occur. This coupling results from the interaction of the valence electrons of the two neighboring atoms according to the Pauli-principle and can be described via the following Hamilton operator:

$$\hat{H}_J = J_{12}\, \hat{I}_1 \cdot \hat{I}_2 \tag{37}$$

with the scalar coupling constant $J_{12}$, coining the term '$J$-coupling'. The resulting split energy states produce a spectral multiplet, which is measurable by NMR. The number of arising energy levels $j$ can be calculated from the number of neighboring interacting atoms $i$ via:

$$j = i + 1 \; . \tag{38}$$

In this work, this can be observed for ethylene glycol (EG), as well as [1,2-$^{13}$C]pyruvate. For EG, a naturally abundant $^{13}$C atom will interact with the two adjacent $^{1}$H atoms, resulting in a triplet. All further structuring of the energy splitting cannot be observed via the used MR setup. The position of the $^{13}$C atom is not relevant due to the symmetry of the EG molecule.
For [1,2-$^{13}$C]pyruvate, the two chemically-different $^{13}$C-enriched positions will interact, leading to two observable doublets.

### 2.2.4. Spatial Encoding

In order to assign signal to a specific location within the measured volume, magnetic field gradients are employed. Depending on the spatial position, the Larmor frequency is now changed by a new term, which uses the position $\vec{r}$ and the gradient vector $\vec{G}$:

$$\omega(\vec{r}) = \gamma(B_0 + \vec{r} \cdot \vec{G}) \ . \tag{39}$$

Using this new information also extends eq. (28), adding a new gradient induced oscillation to the precession of the magnetization:

$$S(t) = \int_{-\infty}^{+\infty} S(\vec{r}, 0) e^{i\omega_0 t} e^{-\frac{t}{T_2}} e^{i\gamma \vec{r} \cdot \vec{G} t} \mathrm{d}V \ . \tag{40}$$

Eq. (40) is commonly substituted by the $k$ value, which is defined by the integral over a time-dependent gradient $\vec{G}(t)$:

$$\vec{k}(t) = \gamma \int_0^t \vec{G}(\tau) \mathrm{d}\tau \ . \tag{41}$$

After transformation into a frame of reference rotating with $\omega_0$, this results in the signal only being dependent on $\vec{k}(t)$:

$$S(\vec{k}(t)) = e^{-\frac{t}{T_2}} \int_{-\infty}^{+\infty} S(\vec{r}, 0) e^{i\vec{r} \cdot \vec{k}(t)} \mathrm{d}V \ . \tag{42}$$

This description $S(\vec{k}(t))$ defines the so-called $k$-space, which is inverse to the image space. The $k$-space is often used when MR sequences are characterized as it enables a visual presentation of the data acquisition. With this new concept, the signal distribution $S(\vec{r}, 0)$ in the image space can be derived via applying an inverse FT:

$$S(\vec{r}, 0) = \mathcal{F}^{-1}[S(\vec{k}(t))] = \frac{1}{2\pi} \int_{-\infty}^{+\infty} S(\vec{k}(t)) e^{-i\vec{r} \cdot \vec{k}(t)} \mathrm{d}\vec{k}(t) \ . \tag{43}$$

This result is directly proportional to the localized spin density $\rho(\vec{r})$, as described in eq. (29). Hence, this reconstruction process represents a localization of the acquired data and produces 3D intensity maps of the investigated resonances.
The $k$-space representation is useful to directly calculate the field-of-view (FOV), which represents the spatial imaging range:

$$\mathrm{FOV} = \frac{1}{\Delta k} \tag{44}$$

with $\Delta k$ being the step size in which the spatial domain is sampled in $k$-space.
The spatial resolution is then simply the FOV divided by the number of acquired points $N_k$:

$$R_{\mathrm{spat}} = \frac{\mathrm{FOV}}{N_k} \ . \tag{45}$$

### 2.2.5. Point Spread Function (PSF)

However, in reality, the acquired data is finite and hence, the expression of eq. (43) is calculated via a discrete fast Fourier transform (FFT) algorithm. This also changes the actual voxel size given by eq. (45). A calculation is possible by a multiplication with a sampling grid $F_{\mathrm{sample}}(\vec{k}(t))$:

$$S_{\mathrm{sample}}(\vec{k}(t)) = S(\vec{k}(t)) \cdot F_{\mathrm{sample}}(\vec{k}(t)) \ . \tag{46}$$

For the one-dimensional case, $F_{\mathrm{sample}}(\vec{r}) = \mathcal{F}^{-1}[F_{\mathrm{sample}}(\vec{k}(t))]$ is described by a sinc shape and, therefore, produces a smearing out of the resulting voxel. Moreover, the signal intensities spreading outside of the nominal voxel size, i.e. the sinc sidelobes, will contaminate neighboring voxels, an effect called 'voxel bleeding'. $F_{\mathrm{sample}}(\vec{r})$ is also referred to as point spread function (PSF), which is used to quantify the actual voxel size through the width of the central main lobe.

### 2.2.6. RF Excitation

The RF pulse used in this thesis is a whole-volume excitation, meaning no gradients are applied simultaneously. There are four main specifications through which an RF pulse is defined, which are the pulse shape $B_1(t)$, pulse length $t_p$, amplitude $B_{1,\mathrm{max}}$ and center frequency $f_c$.
The center frequency is described in eq. (16) ($f_c = \frac{\omega_{\mathrm{RF}}}{2\pi}$) and sets the center point of the excited frequency range. The pulse length defines how far off-resonant spectral points are excited. Due to the inverse nature of the FT, a longer RF pulse means a sharper

excitation range in the frequency domain. The RF amplitude $B_{1,\max}$, together with $t_p$, defines the FA, as the integration in eq. (18) shows. Finally, the RF pulse shape $B_1(t)$ defines the intensity, in which off-resonant points are effected as a direct result from its FT.

In this work, only block and sinc pulses are applied, which, in turn, produce a sinc and block excitation profile in the frequency domain (see Figure 2). Since, in reality, no infinitely long sinc pulses can be applied, a certain cut-off has to be defined. This is done via the time-bandwidth product (TBW), which is defined as:

$$\mathrm{TBW} = t_p \cdot \mathrm{BW}_{\mathrm{RF}} \tag{47}$$

$$B_1(t) = B_{1,\max} \cdot \mathrm{sinc}(\mathrm{TBW}\frac{t}{t_p}) \tag{48}$$

with $-\frac{t_p}{2} \leqslant t \leqslant \frac{t_p}{2}$.

Here, $\mathrm{BW}_{\mathrm{RF}}$ stands for the excited frequency range at half maximum of the $M_\perp$ profile in the frequency domain. For the pulse shape, the TBW also corresponds to the number of zero-crossings for the sinc function in the time domain before the cut-off.

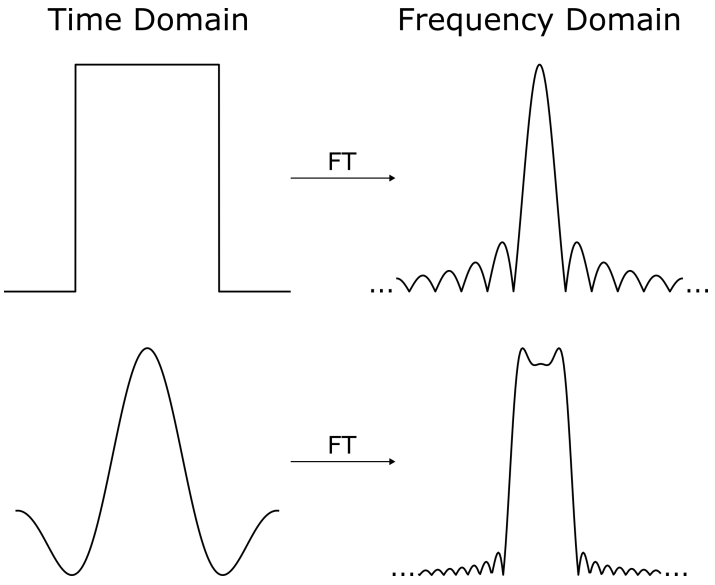


Figure 2: Block and sinc pulse shapes of the applied RF pulses in the time domain. Through Fourier transformation, the excitation profile in the frequency domain can be calculated, which in turn has a sinc or block shape, respectively. Note that for the infinitely long sinc function a certain cut-off has to be defined, which results in truncation artifacts of for block shape in frequency domain.

## 2.3. Hyperpolarization

Conventionally, MRI uses the resonance of the $^1$H nucleus, however also other MR-sensitive nuclei can be used for imaging, as mentioned in Section 2.1.1. In this thesis, the main focus is dedicated to the carbon nucleus, which occurs as the MR-sensitive $^{13}$C isotope with a nuclear spin of $I = \frac{1}{2}$. However, this brings along technical challenges, since the natural abundance (NA) of $^{13}$C is only about 1.1% and the gyromagnetic ratio $\gamma$ almost a quarter of the $^1$H one (see Table 1). Additionally, the administered amount of $^{13}$C labels $N/V$ is about three orders of magnitude below the in vivo $^1$H concentration. The resulting total available magnetization $M$ can then be calculated from eq. 14 to be five orders of magnitude lower.

| Nuclei | NA | $\gamma\,[\frac{\mathrm{MHz}}{\mathrm{T}}]$ | $N/V\,[\frac{1}{\mathrm{m}^3}]$ | $M\,[\frac{\mathrm{A}}{\mathrm{m}}]$ |
|---|---|---|---|---|
| $^1$H | 100% | 42.58 | $10^{19}$ | $10^{-11}$ |
| $^{13}$C | 1.1% | 10.71 | $10^{16}$ | $10^{-16}$ |

Table 1: Comparison of the order of magnitude of the magnetization and its factors for $^1$H and $^{13}$C .

This would render $^{13}$C MRI unusable in clinical settings. However, several measures can be taken to increase this inherently low MR signal via enhancement of the polarization $P$:

$$P = \frac{N_+ - N_-}{N_+ + N_-} = \tanh\left(\frac{\gamma\hbar B_0}{2k_B T}\right) . \tag{49}$$

The most straight-forward approach to increase $P$, also called 'brute force' method, following from eq. 49, is to increase the magnetic field $B_0$ and decrease the temperature $T$. However, both of these quantities are restricted by technical limitations and in vivo conditions. Thus, further hyperpolarization (HP) techniques have been developed, as described in the next section.

### 2.3.1. Dissolution Dynamic Nuclear Polarization

The HP method used in this work is called dissolution dynamic nuclear polarization (d-DNP), which provides a signal enhancement of a factor of more than 10,000 [14]. Electrons possess a gyromagnetic ratio of $\gamma_e \approx 28.02\ \frac{\mathrm{GHz}}{\mathrm{T}}$, three orders of magnitude higher compared to $^{13}$C. Using eq. 49 and inserting $T = 1$ K and $B_0 = 5$ T, this yields a 99.75% polarization for electrons, while $^{13}$C only shows a value of 0.13%.

d-DNP aims to transfer a part of the much higher polarization of electrons to the $^{13}$C nucleus. For this purpose, the $^{13}$C-enriched substrate is frozen to an amorphous solid at $T < 4$ K and doped with a radical, typically trityl radical, which provides the necessary free electrons. At these low temperatures and in a high magnetic field of $B_0 = 5$ T, the coupled spin system of electrons and $^{13}$C nuclei is manipulated using microwave (MW) irradiation near the electron resonance frequency. This triggers multiple mechanisms [31, 32], like the solid effect and the Overhauser effect, which result in a saturation of higher energy states. In subsequent relaxation processes in the solid substrate, favored transitions yield an increase in the total polarization of the $^{13}$C nuclei.
As soon as a sufficiently high $^{13}$C polarization is achieved, the substrate is rapidly dissolved in a heated medium and filtered from remaining radical molecules. The resulting hyperpolarized liquid can then be administered. However, as soon as the dissolution process starts and the substrate leaves the above described conditions, its polarization will revert back to the ground state. This decay is governed by the $T_1$ relaxation and depends on the used substrate. In the case of this thesis, [1-$^{13}$C]pyruvate and [1,2-$^{13}$C]pyruvate are used, for which the $T_1$ times at 3 T are about 40-60 s in aqueous model solutions and 10-20 s in vivo [17, 33].

### 2.3.2. $^{13}$C-Enriched Pyruvate

Most prominently used in HP $^{13}$C experiments is $^{13}$C-enriched pyruvate [34]. Pyruvate serves as a central biochemical molecule in the human energy metabolism [35], as it is part of the glycolysis.
The two relevant metabolic conversions that are investigated in this thesis are the lactate dehydrogenase (LDH) reaction and the alanine transaminase (ALT) reaction.
The LDH enzyme catalyzes the conversion of pyruvate into lactate with a simultaneous oxidation of nicotinamide adenine dinucleotide (reduced form, NADH) to $NAD^+$. This supports energy metabolism in the absence of oxygen, as the regeneration of $NAD^+$ allows glycolysis to continue.

$$\text{Pyruvate} + \text{NADH} + \text{H}^+ \overset{\text{LDH}}{\rightleftharpoons} \text{Lactate} + \text{NAD}^+ \tag{50}$$

The enzyme ALT is mostly found in the liver and muscle tissue and catalyzes the production of alanine and $\alpha$-ketoglutarate by transfer of an amino group from glutamate to pyruvate. Alanine is an important amino acid involved in the biosynthesis of proteins.

$$\text{Pyruvate} + \text{Glutamate} \overset{\text{ALT}}{\rightleftharpoons} \text{Alanine} + \alpha\text{-Ketoglutarate} \tag{51}$$

When injecting $^{13}$C-enriched pyruvate into a living organism, the MR-sensitive $^{13}$C label is transferred to Lactate and Alanine. Since those newly formed molecules then exhibit a changed chemical surrounding, additional resonances appear in the spectral data, which allow the quantification of the metabolic turnover of pyruvate into these substrates. This enables the investigation and characterization of disease-specific metabolic alterations, like the Warburg effect in the case of cancer [36], ultimately aiding in their diagnosis and treatment assessment.

## 2.4. Magnetic Resonance Fingerprinting

Magnetic Resonance Fingerprinting (MRF) can produce multiple parameter maps in a single acquisition, mostly such as $T_1$, $T_2$ and $M_0$ [37]. Moreover, it can be extended and adapted to predict even more properties of interest, like $B_1^+$ or exchange rates [28, 38]. To this end, MRF uses the fact that the signal evolution of an MR measurement is dependent on the specific properties of the measured material or tissue. Through exact simulation of the measurement sequence with varying experimental input parameters, like relaxation times, this signal evolution is, in theory, recreatable [27]. This concept is realized by simulating the conducted experiment for several starting parameters and comparing it to the acquired data. The closest match then represents an estimate of the actual underlying properties.
In this thesis, MRF is used to produce $B_1^+$ maps to predict the actual applied flip angle for $^{13}$C measurements. A $B_1^+$ map is necessary whenever a new RF pulse or coil is applied, since coil geometry and excitation pulse performance is dependent on the nucleus and the coil itself [39, 40], which results in a deviation from the nominal value of eq. (18). Most available FA mapping methods are only applicable for the $^1$H nucleus, high flip angles and rely on fully relaxed $T_1$ [41–43]. However, as a preparation for HP measurements, the $^{13}$C nucleus and especially low FA are of interest.

### 2.4.1. Signal Simulation

The collection of simulations, called a dictionary, is filled by changing the input parameters to the Bloch equations eq. (22−24), which depend on the applied sequence as well as the object under investigation. The sequence parameters are known and set through the acquisition itself, while the properties of the object are of interest and their estimation is the aim of the MRF. Therefore, to find these properties, a set of starting values, later also referred to as 'fingerprinting parameters', is defined. Then, the experiment is simulated with all possible combinations of these fingerprinting parameters. The complete set of all simulated signal evolutions, also called fingerprints, forms a dictionary.

### 2.4.2. Dictionary Matching

In the matching process, the simulated fingerprints $S_{\text{sim}}$ are, first of all, brought to the same $L^2$ norm by dividing them through the following factor:

$$L^2 = \left| \sqrt{\sum_{i=1}^{N} S_{\text{sim}} \cdot \overline{S}_{\text{sim}}} \right| \tag{52}$$

with $N$ being the number of points within one fingerprint and $\overline{S}_{\text{sim}}$ the mean value. Then, the vector dot product is calculated between the acquired data $S$ and all computed fingerprints $S_{\text{sim},q}$. The maximum value determines the optimal match:

$$S_{\text{sim,best}} = \arg\max_{q} \left[ S \cdot \left( \frac{S_{\text{sim},q}}{L_q^2} \right) \right] \tag{53}$$

with $q = 1, ..., Q$ and $Q$ as the total number of simulated fingerprints.
In a final step, the used simulation parameters are extracted from the best matching simulation $S_{\text{sim,best}}$. These values then represent the estimate for the properties of interest, which, in the case of this work, is mainly $B_1^+$ as the actual transmitted FA. Additionally, the spin density $M_0$ can be determined as a result from multiplying the dictionary entry with the corresponding $L_2$ value.

# 3. Materials and Methods

## 3.1. Hardware

### 3.1.1. MR Scanner and RF Coils

All experiments were conducted on a SIEMENS Biograph mMR scanner (Siemens Healthineers, Erlangen, Germany) at the German Cancer Research Center (DKFZ) in Heidelberg, Germany (see Figure 3). This MR scanner has a static magnetic field strength of $B_0 = 3$ T, a maximal gradient strength of $G_{\max} = 45\ \frac{\mathrm{mT}}{\mathrm{m}}$ and a maximal slew rate of $r = 200\ \frac{\mathrm{T}}{\mathrm{m \cdot s}}$. The rEPSI sequence was implemented on SIEMENS IDEA, version VE11P, while the MRF adaptation used PulSeq, version 1.4.1, on MATLAB R2019b.


Figure 3: The 3 T SIEMENS Biograph mMR scanner (Siemens Healthineers, Erlangen, Germany) at the German Cancer Research Center (DKFZ, Heidelberg, Germany) on which all measurements were conducted.

All hyperpolarized MR measurements were performed using a double-resonant $^{13}$C /$^{1}$H volume resonator (RAPID Biomedical, Rimpar, Germany). For the MRF experiments a double-resonant $^{13}$C /$^{1}$H head coil (RAPID Biomedical, Rimpar, Germany) with 16 receiver channels was used. Both coils are shown in Figure 4.

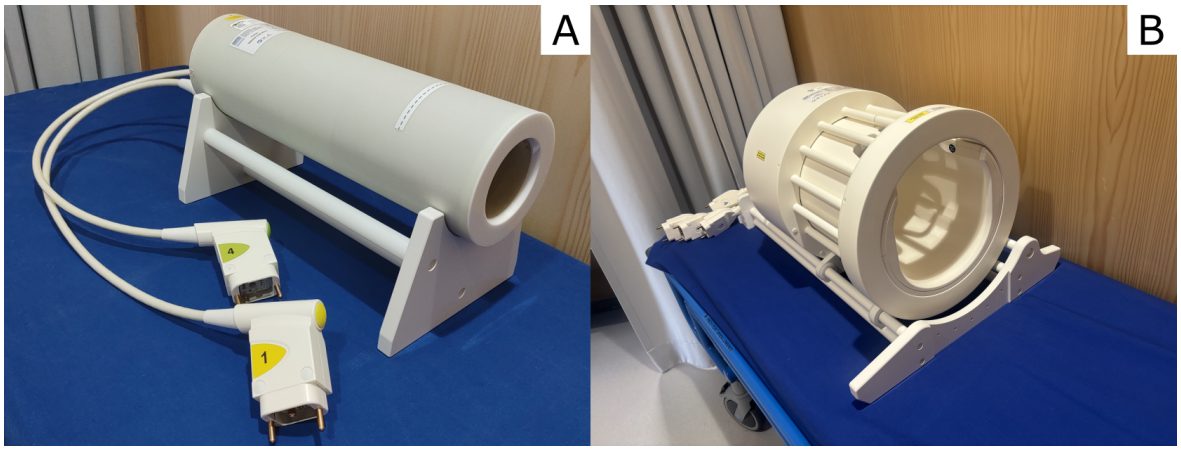


Figure 4: (A) The double-resonant $^{13}$C /$^{1}$H volume resonator (RAPID Biomedical, Rimpar, Germany) used for all hyperpolarized MR measurements. (B) The double-resonant $^{13}$C /$^{1}$H head coil (RAPID Biomedical, Rimpar, Germany) with 16 receiver channels used for all MRF experiments.

### 3.1.2. Dissolution Dynamic Nuclear Polarization (d-DNP) System

The dissolution dynamic nuclear polarization (d-DNP) process was performed using the GE SPINlab$^{TM}$ system (General Electric Healthcare, Chicago, USA) shown in Figure 5 (A). The vials containing the sample formulations are frozen in its cryogenic sample cup at a temperature of $T < 4$ K surrounded by a superconducting magnet with a field strength of $B_0 = 5$ T. The microwave resonator with a frequency range of $f = (138.5 - 140.5)$ GHz is tuned to the specific electron resonance of the used radical to transfer the polarization to the $^{13}$C-labeled compound. The average total polarization time was 2 h.

Via a rapid dissolution, the solid hyperpolarized substance is liquefied and extracted as an injectable solution through a fluid path system, which is shown in Figure 5 (B). The location of the d-DNP system is close to the used MR scanner ($< 10$ m), allowing for a short average transition time of $35.4 \pm 3.0$ s from dissolution until start of the MRSI acquisition, including quality assurance.

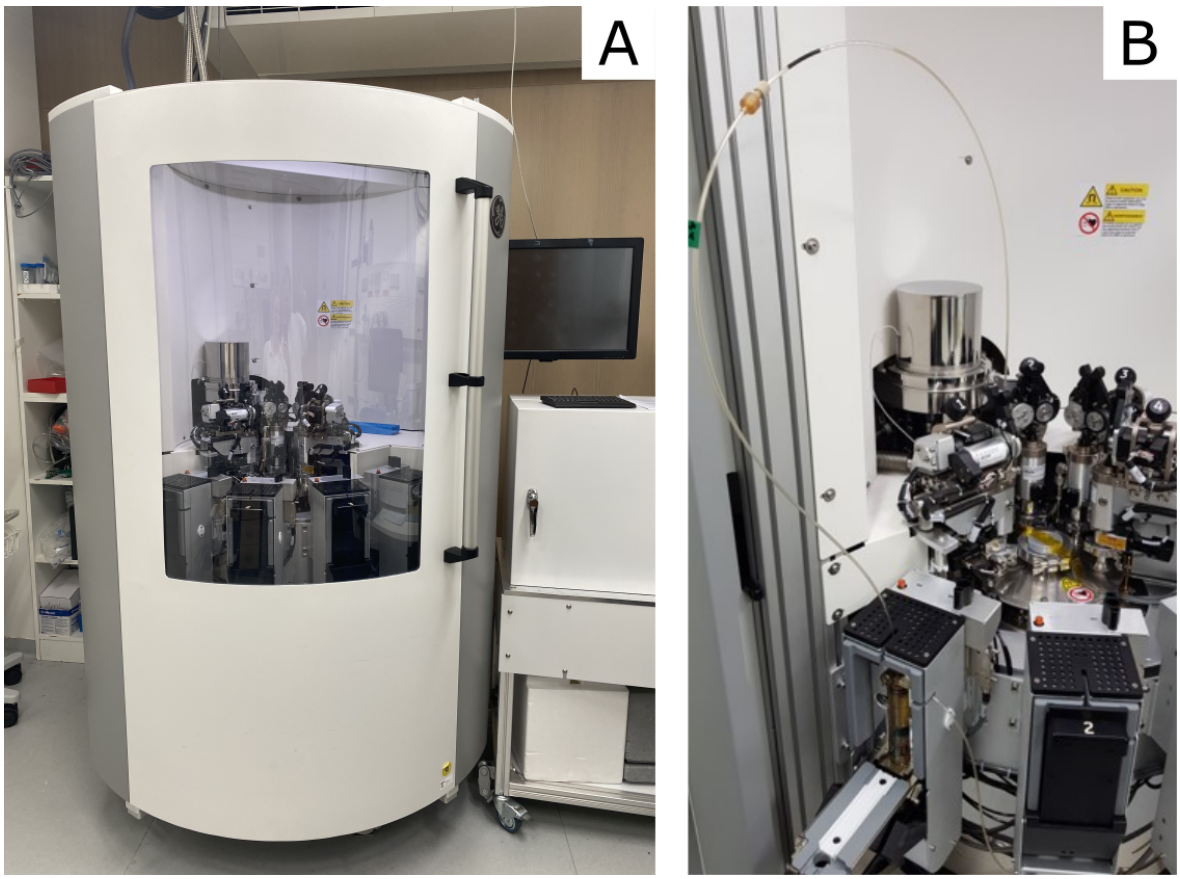


Figure 5: (A) The GE SPINlab$^{TM}$ system (General Electric Healthcare, Boston, USA) used for the d-DNP process. (B) The fluid path system through which the dissolved hyperpolarized sample can be extracted from the d-DNP system.

## 3.2. Phantoms and In Vivo Subjects

### 3.2.1. Ethylene Glycol Phantoms

For $^{13}$C MR experiments at thermal polarization, ethylene glycol (EG, anhydrous, 99.8% from Sigma Aldrich, St. Louis, USA) was used, containing a high concentration of carbon nuclei, resulting in a large number of the $^{13}$C isotope at the natural abundance to produce a sufficient MR signal for measuring. With the volume resonator coil, a 50-mL Falcon® tube (Corning Inc., Corning, USA) filled with EG was used and with the head coil a larger 2-L Nalgene® bottle (Thermo Fisher Scientific Inc., Waltham, USA). The molecular structure of EG can be found in Appendix A.

### 3.2.2. In Vivo Pyruvate Injections

For all in vivo experiments featuring [1-$^{13}$C]pyruvate or [1,2-$^{13}$C]pyruvate, male tumor-bearing Copenhagen rats (syngeneic Dunning prostate adenocarcinoma R3327-HI, right hind leg) were used, which were approved by the local authorities (animal approval: G197/17 for [1-$^{13}$C]pyruvate and G151/22 for [1,2-$^{13}$C]pyruvate) and kept under standard laboratory conditions. The average injection volume was around 1.5 mL, containing 0.9% sodium chloride. The dose was adjusted to the weight of the rat (5 mL/kg), providing a substrate concentration of around 80 mM. Quality assurance provided average values of a pH of $(7.23 \pm 0.28)$ and a temperature of $(37.7 \pm 4.6)$ °C, ensuring safe conditions for the animals.

The metabolism of these animals was investigated before and after treatment of the tumor with heavy-ion radiotherapy using a $^{12}$C beam.

Furthermore, prior comparison measurements showed that metal components of the syringe, such as a stainless steel cannula, can diminish the hyperpolarization [44] (see Appendix B). Hence, all presented in vivo measurements with HP pyruvate injections were conducted using a plastic cannula.

### 3.2.3. In Vivo MRF Measurement

The in vivo $^{13}$C MRF measurements were performed on one healthy volunteer (male, 38 years old).

## 3.3. Basic Data Acquisition and Reconstruction

### 3.3.1. 1D Echo-Planar Spectroscopic Imaging (EPSI)

The echo-planar spectroscopic imaging (EPSI) sequence is used to simultaneously sample $k$-space and spectral domain [45]. The one-dimensional scheme (see Figure 6) consists of a full-volume RF excitation pulse followed by a prephaser gradient, bringing the readout to $+k_{\max}$. From there, an oscillating gradient train $G(t)$ with the amplitude $G_{\text{Amp}}$ samples one $k$-space line $n$ times, from $+k_{\max}$ to $-k_{\max}$, in accordance with the number of gradient lobes:

$$G_{\text{Read}}(t) = -G_{\text{Amp}} \cdot \sin(\frac{\pi t}{t_d}) \tag{54}$$

with $t \in [0, n \cdot t_d]$.
The prephaser gradient causes a spin dephasing additional to the $T_2^*$ effects (see Section 2.2.1). However, this effect is reversed in the center of each following gradient lobe with alternating polarity, producing a so-called gradient echo. The intensity of these echoes decays over time through the $T_2^*$ relaxation. In the following, the total measurement time of one $k$-space line, i.e. the full 1D EPSI scheme, is called repetition time (TR).
The direction of traversing $k$-space is inverted for each lobe, therefore, they are labeled as 'odd' and 'even' for the direction of $+k_{\max}$ to $-k_{\max}$ and $-k_{\max}$ to $+k_{\max}$, respectively. A combination of the odd and even datasets is not straightforward, as shown in Section 3.3.7, hence, they are reconstructed separately.
In the following, the four most essential acquisition parameters and their rEPSI implementation are described for the odd dataset, and analogously for the even one:

- The FOV is defined by the gradient amplitude, which sets the value for $k_{\max}$ and therewith changes the distance $\Delta k$ between the $k$-space points.
- The spatial resolution is defined by the number of points $m$ acquired within one lobe. Simultaneously, the gradient amplitude has to be changed to keep $\Delta k$, i.e. the FOV, constant. This parameters is most restricting for $^{13}$C acquisitions, due to limitation of the gradient hardware, such as slew rate and maximal amplitude.

- The spectral BW is defined by the length of the gradient lobes, which changes the dwell time $t_d$ between the timepoints of the sampled $T_2^*$ decay. For an increased spectral BW, a higher gradient slew rate is necessary.
- The spectral resolution is defined by the number of acquired lobes $n$, corresponding to the number of sampled timepoints and with that, determining how long the $T_2^*$ decay is measured. This parameter increases the acquisition time almost proportionally.

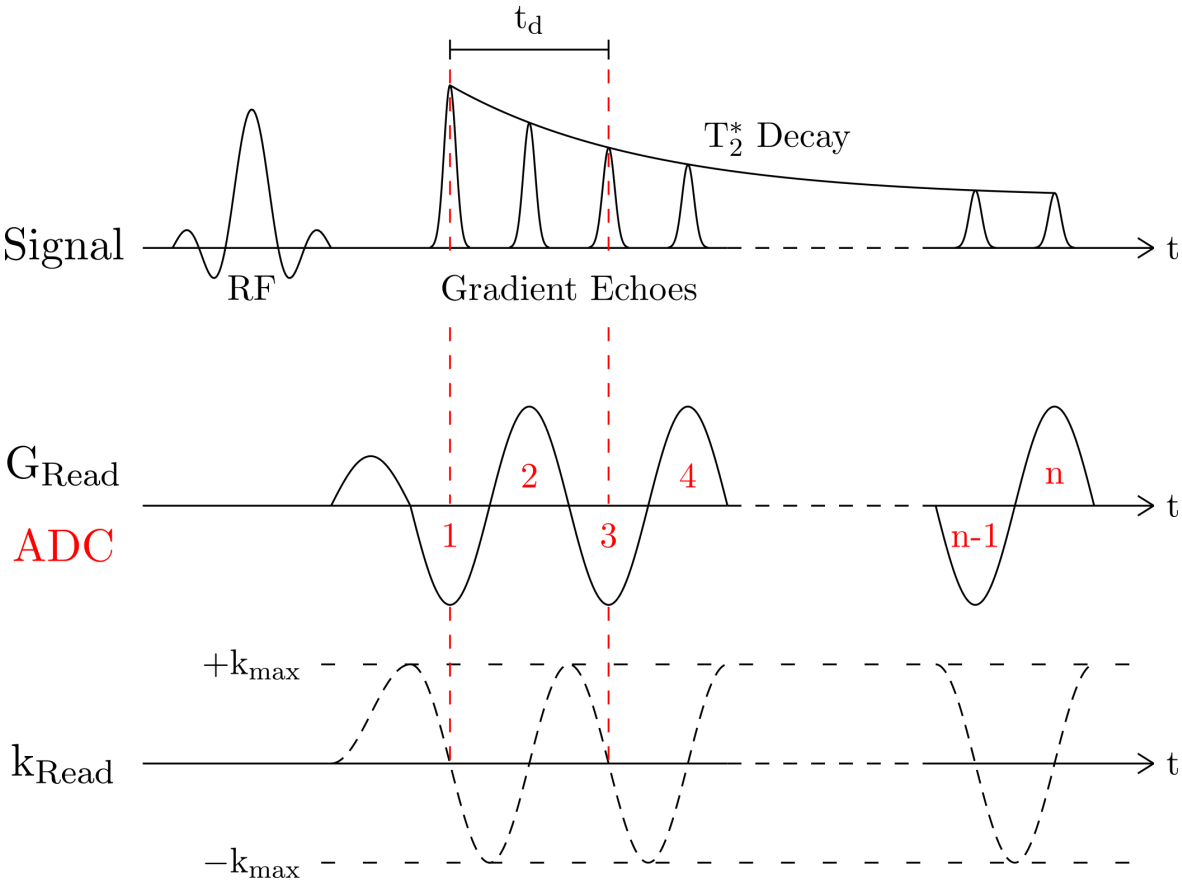


Figure 6: Sequence diagram of the used echo-planar spectroscopic imaging (EPSI) sequence for the one-dimensional case. After a full-volume RF excitation pulse, a prephaser gradient brings the readout to $+k_{\max}$. The following sinusoidal gradient train with $n$ lobes samples one line of $k$-space repeatedly. One full period of this oscillation takes $t_d$. During this acquisition, gradient echoes are produced, which arise from the refocusing spins. The amplitude of these echoes decays over time with $T_2^*$. The resulting data yields 1D spatial information and spectra for each voxel along this dimension.

### 3.3.2. Three-Dimensional Radial EPSI (rEPSI) Sampling

In order to sample all three spatial dimensions, the 1D EPSI scheme of Figure 6 is applied multiple times while rotating the acquired $k$-space line around its center (see Figure 7), producing a volumetric, isotropic spatial resolution. In the following, one single radial acquisition is referred to as a 'spoke'. The spoke rotations are realized by weighting the sinusoidal gradient train (eq. 54) for all three directional gradients as follows:

$$G_x(t) = G_{\text{Read}}(t) \cdot \sin(\theta) \cdot \cos(\phi) \tag{55}$$

$$G_y(t) = G_{\text{Read}}(t) \cdot \sin(\theta) \cdot \sin(\phi) \tag{56}$$

$$G_z(t) = G_{\text{Read}}(t) \cdot \cos(\theta) \tag{57}$$

with $\theta$ and $\phi$ being the polar and azimuthal angle. The calculation of rotation angles is described in detail in Section 3.4.1.

The required number of spokes $M$ depends on the desired number of voxels $m$ along one axis and is based on eq. (44), i.e. the Nyquist criterion [46]. The determination of $M$ is analog to the calculation of the surface of a half-sphere with diameter $m$:

$$M = \text{ceil}\left(2\pi \left(\frac{m}{2}\right)^2\right) \ . \tag{58}$$

This ensures that the minimal distance between points $\Delta k$ on the sphere's surface are not smaller than necessary for the chosen FOV, i.e. FOV $\leqslant \frac{1}{\Delta k}$. Ultimately, $M$ represents the number of starting points of all spokes. The total acquisition time (TA) of a 3D MRSI dataset is calculated via TA = $M\times$ TR.

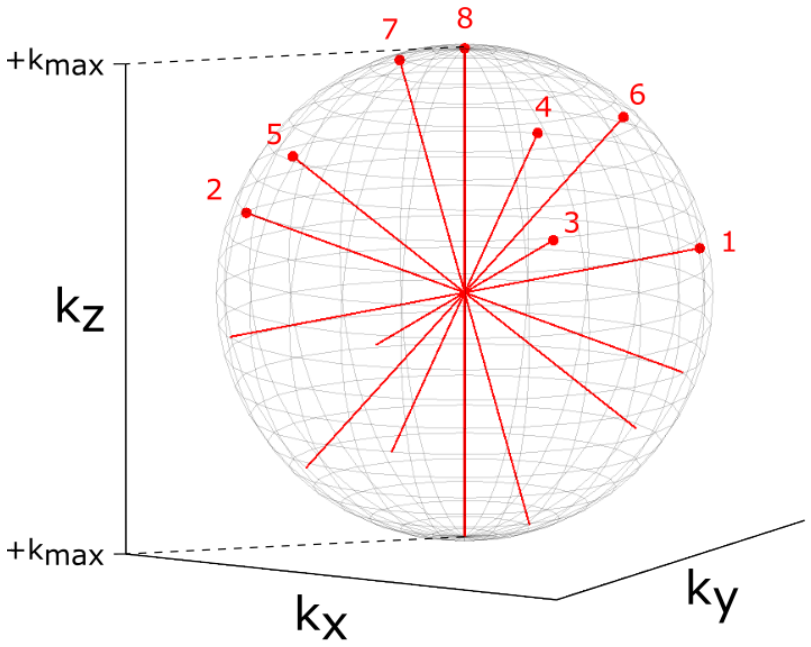


Figure 7: Visualization of the radial spoke distribution in 3D $k$-space for the case of $M = 8$. All spokes (red lines) traverse through the $k$-space center. Their starting points are marked as red dots, numbered for the order in which they are acquired (see Section 3.4.1). The last acquired spoke only runs along the $z$-direction from $+k_{\max}$ to $-k_{\max}$ and back, analogously to what is shown in Figure 6.

### 3.3.3. Gridding Reconstruction

In order to be able to use a fast Fourier transform (FFT), all points have to lie on an equidistant Cartesian grid. Therefore, the radially sampled points have to be redistributed via a so-called data-driven gridding reconstruction [47]. This process is visualized in Figure 8, where around each sampled datapoint $S_i$ a window $W$ is defined, within which the signal of $S_i$ is distributed onto points of a defined grid $C_j$. $W$ is defined via a kernel, i.e. the Kaiser-Bessel function [48], which is used to account for the distance between $S_i$ and all nearby points $C_j$. Its shape reduces voxel-bleeding by minimizing sidelobes, but also enlarges the effective voxels due to a wider main lobe (see Appendix C). The Kaiser-Bessel function is calculated by using a window size of four and a grid oversampling of two [49]. By applying a grid oversampling, i.e. reducing the mesh size, aliasing artifacts are shifted out of the original FOV to reduce their contribution to the image quality.

Additionally, a density compensation is applied to account for the assigned $k$-space volume of each sampled point. This is necessary, since the $k$-space center is strongly overweighted, as it is the crossing point of all spokes (see Figure 7), and also, since the $k$-space is sampled much closer at the periphery along one spoke due to the sinusoidal gradients.

For a more detailed description of the full gridding process, the reader is referred to [21].

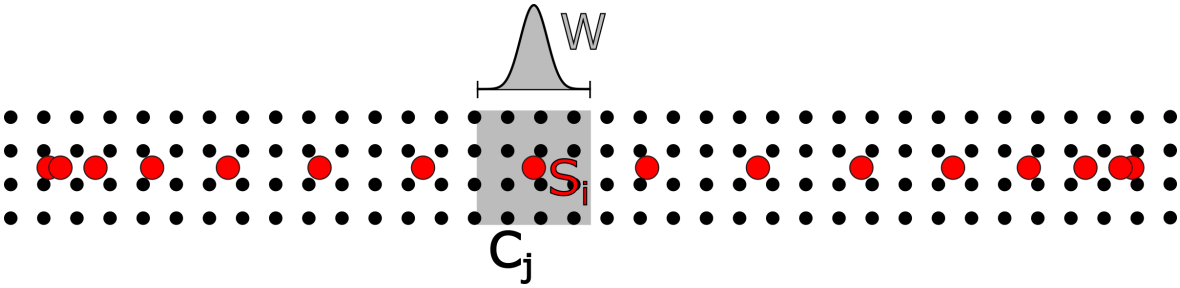


Figure 8: Radially sampled points $S_i$ of one spoke (red) and the points of the Cartesian grid $C_j$ (black) in a two-dimensional $k$-space. During the data-driven gridding algorithm, the signal of $S_i$ is distributed to all $C_j$ within a defined window $W$, using the Kaiser-Bessel function for distance-weighting. The underlying grid uses an oversampling factor of two, reducing the mesh size. In a final step, a density compensation is applied, which accounts for the higher sampling of the periphery of $k$-space along one spoke, as well as the higher sampling density in $k$-space center, where all spokes cross.

### 3.3.4. Zerofilling

The spectral and spatial resolution can be improved visually by zerofilling, i.e. extending the data with zeros after the gridding reconstruction [8]. In the spectral case, this simulates an increased total acquisition time by appending additional timepoints in the time domain. For a zerofilling factor of two, eq. (31) would change the number of acquired points by $N_{t,\text{zerofilled}} = 2N_t$.
In the spatial case, analogously, the outer regions of $k$-space are extended by zeros, changing eq. (45) with $N_{k,\text{zerofilled}} = 2N_k$.
This process does not add information to the shown data, but provides a smoother visualization. However, it has to be made sure beforehand that the peripheral datapoints do not show a significant signal amplitude. Otherwise, truncation artifacts can occur after applying the FT, caused by a sharp step from the non-zero signal to the appended zeros.

### 3.3.5. Apodization

Another method to improve the data quality, next to zerofilling, is the apodization of the temporal and the $k$-space data [8]. All data shown in this thesis is post-processed via this technique.
For temporal data, the FID is multiplied with one of the following filter functions:

$$f_\text{L}(t) = \exp\left(-\frac{t}{T_\text{f}}\right) \tag{59}$$

$$f_\text{G}(t) = \exp\left(-\frac{t^2}{T_\text{f}^2}\right) \tag{60}$$

with $T_\text{f} = 40$ ms. For all phantom data, the Lorentzian weighting $f_\text{L}$ was applied, and for all in vivo data the Gaussian weighting $f_\text{G}$. The resulting FID is additionally suppressed at later timepoints, which primarily contain noise, hence improving the SNR. Moreover, in the case of a very short TR, truncation artifacts are reduced. However, this also broadens the peaks with FWHM $= \frac{2}{T_2^*} + \frac{2}{T_\text{f}}$.
To filter the data in $k$-space, a cosine weighting is multiplied:

$$f_\text{cos}(k) = \frac{1}{2} + \frac{1}{2}\cos^2\left(\frac{\pi k}{m}\right) \tag{61}$$

where $m$ is the number of acquired points along one dimension in $k$-space for $-k_\text{max} \leqslant k \leqslant k_\text{max}$.

This filter suppresses the most-outer $k$-space points with a factor of 0.5, while the $k$-space center is at the original intensity of 1. The result is a reduction of the outer side lobes of the PSF, but also a broadening of the main lobe. In turn, less long-ranging artifacts are present in the final data at the expense of an increased effective voxel size.

### 3.3.6. Denoising

The denoising algorithm used for the in vivo $^{13}$C MRF data is based on a singular value decomposition [50]. Here, the FID dataset $A$ is decomposed into a diagonal matrix $S$ and the unitary matrices $U$ and $V$:

$$A = USV^* \tag{62}$$

where the trace of $S$ consists out of the singular values of $A$ and $V^*$ indicates the conjugate transpose of $V$.
Depending on the applied rank $r$, all values of this trace, except the first $r$ ones, are set to zero, changing $S$ to $S_r$. As the singular values are ordered with decreasing ampltiude, later entries represent noise, while the first entries determine the spectral information. This way noisy spectral components can be removed after $A$ is rebuild using eq. 62 and using the new singular value matrix $S_r$.
The applied denoising is of rank $r = 1$, only preserving the highest singular value (see Appendix D).

### 3.3.7. Odd and Even Data Recombination

Even though the acquired rEPSI data is divided into odd and even datasets, as described in Section 3.3.1, a recombination can be attempted post-reconstruction. This can either be done by (i) adding them voxel by voxel, resulting in an SNR increase by $\sqrt{2}$, or by (ii) an interleaved recombination [51].
The latter approach results in a doubling of the spectral BW, but is prone to aliasing artifacts through a phase shift between odd and even datasets, resulting in 'ghost' resonances, shifted exactly $\frac{\mathrm{BW}}{2}$ relative to the 'real' peak. Hence, the correction of timing differences is crucial to keep this effect to a minimum. Different than for the $k$-space center with a consistent dwell time of $t_d$, all other $k$-space points are sampled with changing time intervals $t_1$ and $t_2$, depending on the gradient polarity, as depicted in Figure 9. Additional gradient imperfections produce further timing inconsistencies, which accumulate during long acquisitions.

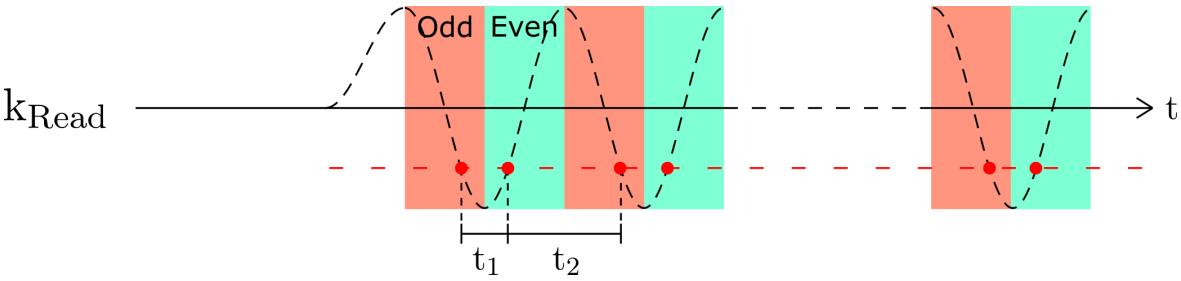


Figure 9: Visualization of the differences in dwell time for the odd (red) and even (green) datasets. Along the red dashed line, all points are acquired at the same point in $k$-space, i.e. belong to one voxel. However, the direction of traversing $k$-space is different through the oscillating gradient. This leads to a changing dwell time between odd-even and even-odd points as $t_1$ and $t_2$, respectively.

As a correction before the interleaved recombination, the even signal $S^{\text{even}}$ is adjusted to the odd phase, as this approach has shown to provide the most stable results [51]. Therefore, the zero phase order $\Phi_0$ is determined via an AMARES fit (see Section 3.3.9). Afterwards, $S^{\text{even}}$ is multiplied with a phase term, which uses the difference between $\Phi_0^{\text{even}}$ of the even and $\Phi_0^{\text{odd}}$ the odd data:

$$S_{\text{corr}}^{\text{even}}(t) = S^{\text{even}}(t) \cdot \exp(-i(\Phi_0^{\text{even}} - \Phi_0^{\text{odd}})) \; . \tag{63}$$

Finally, the timepoints for each voxel, corresponding to the red dashed line in Figure 9, are interleaved and then reconstructed.

### 3.3.8. *k*-Space Centers

The $k$-space center is traversed continuously during the rEPSI acquisition, as seen in Figure 6. Since here, no gradients are applied, these points can be treated as a non-localized FID dataset. However, this is not completely straightforward, since the number of sampled $k$-space points $m$ is always even, hence the $k$-space center is never sampled directly, but only at a slight temporal offset of $\frac{t_d}{2m}$. Nevertheless, close-by points can be used after the following phase correction for the odd dataset, and the even one analogously:

$$S_{\text{corr}}^{\text{odd}}(t) = S^{\text{odd}}(t) \cdot \exp\left(-i\omega\frac{t_d}{2m}\right) \; . \tag{64}$$

### 3.3.9. AMARES Fitting Routine

In order to quantify the spectral data, a customized version of the advanced method for accurate, robust and efficient spectral (AMARES) fitting was used [29]. The fitting process is done in the time domain. As input parameters, the time between excitation and start of data acquisition $T_0$, number of echoes $n$, center frequency $f_c$ and the spectral BW are used. Furthermore, boundaries for each variable of all expected resonances $R$ are defined, i.e. the amplitude $a$, phase $\Phi$, damping $d$ and frequency $\omega$. Additionally, it can be decided whether a Lorentzian ($g = 0$) or Gaussian model ($g = 1$) should be applied, in accordance with the used apodization filter from Section 3.3.5. The resulting fitting function can then be summarized as a summation of all expected resonances as complex exponential functions:

$$y_k = \sum_{r=1}^{R} a_r \cdot \exp((-d_r(1 - g + g\, d_r t_k) + i\omega_r)\; t_k) \cdot \exp(i\, \Phi_r) + e_k \tag{65}$$

with $k = 0, 1, ..., n - 1$ and $e$ as a noise estimate extracted from the analyzed dataset. Via minimization of the root of the squared difference between fit and measured data, an optimal result is found.
A detailed description of the AMARES implementation can be found in [52, 53].

## 3.4. Advanced rEPSI Features

### 3.4.1. Gapped Arrangement of Golden Angles (GAGA)

In the following, a novel arrangement of spherical angles for the rEPSI sequence is described, which provides three-dimensional sampling of $k$-space via changing the spatial orientation of the readout, as introduced in Section 3.3.2.

For the last spoke, only the $z$-gradient is applied, just as depicted in Figure 6. From there, the $k$-space line to be sampled is rotated for every spoke, defined as multiples of the inverse golden ratio $\beta$ for the azimuthal angle $\phi$ and an inverse cosine distribution for the polar angle $\theta$:

$$\beta = \frac{1+\sqrt{5}}{2} \tag{66}$$

$$\phi(i) = 2\pi \bmod \left(\frac{i}{\beta}, 1\right) \tag{67}$$

$$\theta(i) = \arccos\left(\frac{i}{M}\right) \tag{68}$$

with the indices $i \in \{1,\ 2,\ ...\ M\}$ and $M$ as the total number of spokes. The ranges are $\theta \in [0; 2\pi)$ and $\phi \in [0; \frac{\pi}{2}]$, distributing all points along the surface of a half-sphere. An example distribution for $M = 8$ can be seen in Figure 7.

Afterwards, all entries $i$ are reordered, according to the gapped arrangement of golden angles (GAGA) [22], maximizing the distance between successive points to provide sufficient and homogeneous $k$-space coverage for a subsequent division into temporal subframes. For the example in Figure 7, this results in the new spoke order $\{1, 5, 4, 7, 3, 6, 2, 8\}$.

To this end, the number of spokes within one subset $M_{\text{sub}}$ is defined before start of the measurement and the haversine formula applied to calculate the great-circle distance between the starting points of all spokes. The sorting then maximizes an objective defined by the maximum distance of each spoke to all previously acquired spokes in general, but also within the most recent subset. That way, not only the whole set of spokes $M$ is distributed as homogeneously as possible, but also the spokes $M_{\text{sub}}$ in each subset.

### 3.4.2. Sliding-Window (SW) Reconstruction

Using the optimally distributed spoke subframes from the GAGA scheme, a sliding window (SW) reconstruction can be applied [23]. This technique divides one full rEPSI acquisition with $M$ spokes into subsets of the size $M_{\text{sub}}$, resulting in multiple undersampled MRSI datasets that share the same spatial resolution as the original measurement. These subsets can be used to produce 3D metabolite maps with a temporal resolution corresponding to TR, i.e. the measurement time of one spoke, thus enabling the analysis of metabolic dynamics [22]. The resulting number of subsets $N_{\text{sub}}$, and consequently also of the timesteps, can be calculated via

$$N_{\text{sub}} = M - M_{\text{sub}} + 1 \, . \tag{69}$$

An example representation of the arrangement of temporal subsets for a simple 2D example is illustrated in Figure 10, where $M = 8$ and $M_{\text{sub}} = 4$, resulting in five subframes.

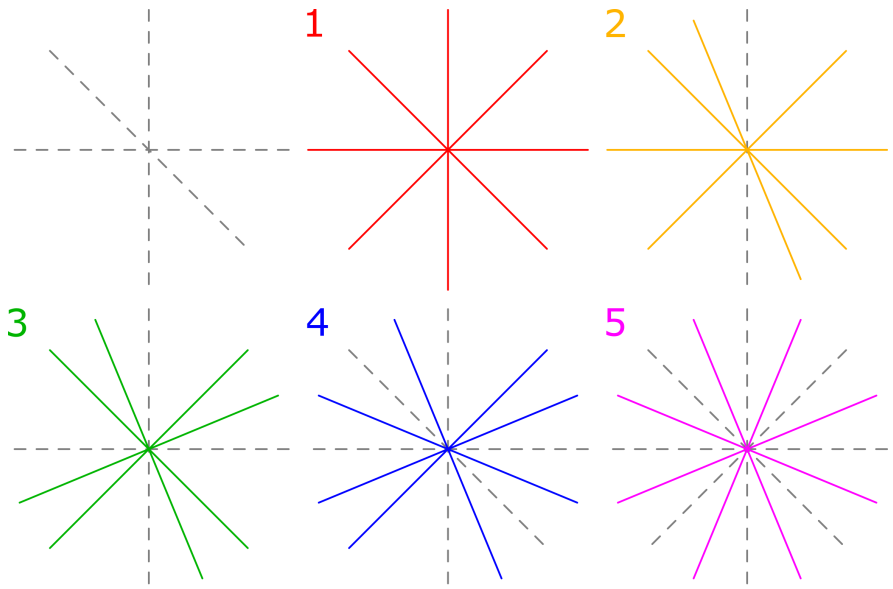


Figure 10: 2D example representing the implemented sliding window (SW) reconstruction. Before the start of the measurement, the number of spokes of the full acquisition ($M = 8$) is defined, as well as the subset size ($M_{\text{sub}} = 4$). With the acquisition of four spokes of the rEPSI readout, the first undersampled subset (red) can be reconstructed. With every new spoke acquired, a new subset of four is formed (yellow, green, blue and violet), keeping the $k$-space coverage as homogeneous as possible. Eventually, a fully sampled dataset can be reconstructed using all eight acquired spokes.

### 3.4.3. $T_1$-Compensating Variable Flip Angle Scheme

Some advanced reconstruction techniques, require a constant MR signal over all acquired spokes (see Section 3.4.4), which is not a given for HP experiments. Therefore, a variable flip angle (VFA) scheme was applied to compensate the intensity loss through $T_1$ decay. To this end, the FA is gradually increased following an inverse tangent with the last FA defined as the 90° point to achieve the full usage of the available signal until the end of the acquisition[1]:

$$\mathrm{FA}(M) = \pi \tag{70}$$

$$\mathrm{FA}(j) = \arctan\left(\exp\left(-\frac{\mathrm{TR}}{T_1}\right)\sin\left(\mathrm{FA}(j+1)\right)\right) \tag{71}$$

with the index $j \in \{M-1, ..., 2, 1\}$ and TR as the acquisition time of one spoke. In the case of the rEPSI sequence, $M$ different flip angles are applied, one for each spoke. The $T_1$ relaxation time was estimated before the start of the experiment with a value of 12.73 s for the in vivo MR experiments. This value represents the average $T_1$ time of all previously conducted HP [1-$^{13}$C]pyruvate MR experiments in rats and was extracted from the data of the $k$-space centers, as described in Section 3.3.8.

### 3.4.4. Echo-Train-Shifting

An alternative to the interleaved recombination of Section 3.3.7 is two consecutive acquisitions of the same spoke while using echo-train-shifting (ETS) [26], which is demonstrated in Figure 11. This technique inserts a small time delay of $\frac{t_d}{2}$ between the prephaser gradient and the oscillating gradient train. The first acquisition ETS #1 is consistent to the initially presented rEPSI scheme, but in the second run ETS #2 all points are sampled with an offset of $\frac{t_d}{2}$. When the two datasets ETS #1 and ETS #2 are now interleaved and then reconstructed, the effective dwelltime $t_d$ is halved, resulting in a doubled spectral bandwidth. Since this entails a second acquisition for every spoke, the total measurement time also increases by a factor of approximately two.

[1] The code used for this implementation was adapted from the source: `https://de.mathworks.com/matlabcentral/fileexchange/49836-hyperpolarized-mri-toolbox`.

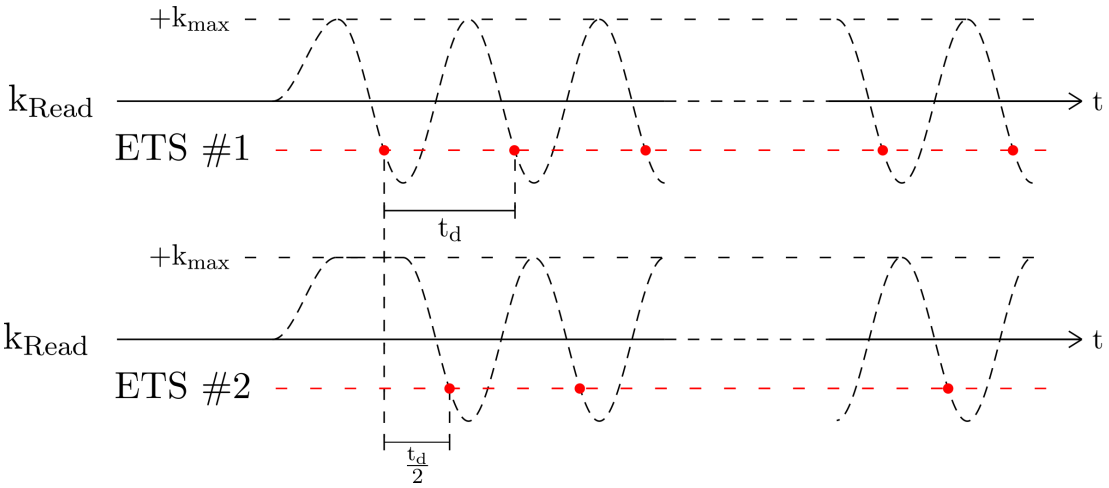


Figure 11: Visualization of the $k$-space acquisition using echo-train-shifting (ETS). The radial readout for each spoke is executed two times. For the first run (ETS #1), the prephaser gradient brings the readout to $+k_{\max}$ and, subsequently, the data acquisition starts, just as described in Section 3.3.1. In the second run (ETS #2), however, the readout is delayed by half the dwelltime $\frac{t_d}{2}$. This leads to a shifted sampling of the $T_2^*$ decay. After interleaving the points of both acquisitions (red dots), the new effective dwelltime has been halved, leading to a doubled bandwidth of the resulting spectral data. In turn, also the total measurement time is approximately doubled, since each spoke has to be sampled twice.

## 3.5. Magnetic Resonance Fingerprinting Using rEPSI

In the following, the implemented $B_1^+$ mapping algorithm is described, which consists of a magnetic resonance fingerprinting (MRF) adaptation of the rEPSI sequence, as well as a subsequent estimation of the actual transmitted FA.

### 3.5.1. MRF Acquisition

For application of the rEPSI sequence to MRF, a reordering of the acquisition scheme is necessary, which was adapted from [28] and is visualized in Figure 12. First, each spoke is acquired multiple times, changing the FA with a $B_1^+$-sensitive pattern [25]:

$$\mathrm{FA}(j) = \mathrm{FA}_{\mathrm{max}} \cdot \sin(\frac{\pi j}{N_{\mathrm{sin}}}) \tag{72}$$

with the index j $\in \{1,2,...,N_{\mathrm{sin}}\}$ and $N_{\mathrm{sin}}$ being the number of FA within one sinusoidal curve. This pattern is repeated three times, using $N_{\mathrm{sin}} = 35$ and appending those sinusoidal curves with $\mathrm{FA}_{\mathrm{max}}$ scaled to 50%, 61.43% and, finally, 100%. Then, the first 100 points of this FA distribution are used, restricting the minimum FA to be 1°.
Afterwards, all spokes with the same FA are grouped and reconstructed, resulting in a 3D MRSI dataset for each FA.

In other words, each voxel of the obtained MRSI data contains the full FA pattern, allowing to match it to the simulated dictionary and with that, estimate the local $B_1^+$ value, as depicted in Figure 13.

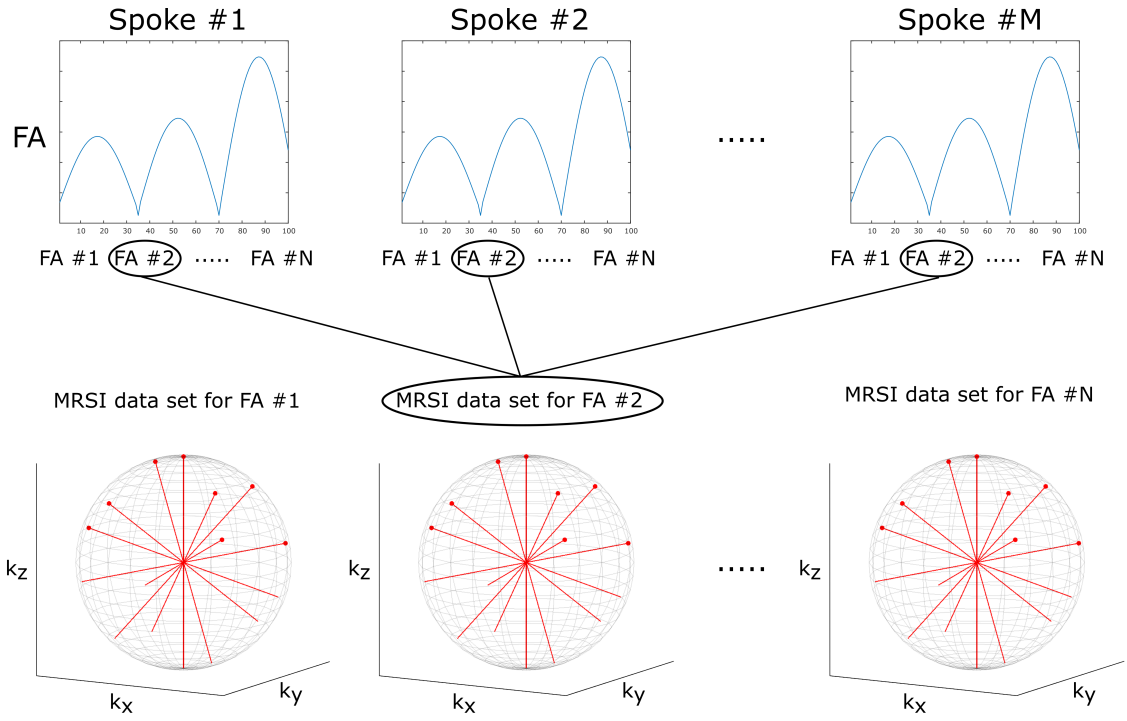


Figure 12: Visualization of the MRF acquisition scheme using the rEPSI sequence. Each spoke is acquired $N$-times throughout the whole variable flip angle (VFA) pattern. After all $M$ spokes are sampled, they are grouped for the same FA and reconstructed to $N$ MRSI datasets.

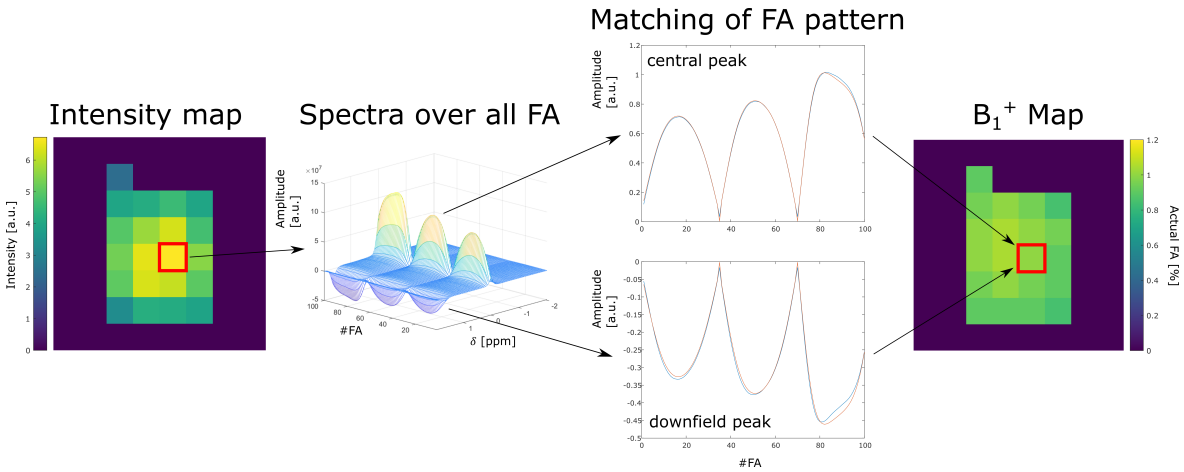


Figure 13: Visualization of the MRF workflow. The resulting dataset from the MRF acquisition scheme (see Figure 12) yields the full spectral information in each voxel over the complete VFA pattern. For this signal evolution, an optimal match from a set of simulations is found. This process is repeated voxel-wise. Using the deviations between the simulated and the applied nominal FA values, a $B_1^+$ map can be calculated as the actual FA in percentage.

### 3.5.2. Dictionary Calculation

The MRF dictionary is built using Bloch simulations with changing starting values. The necessary parameters can be divided into simulation parameters, which are fixed and depend on the rEPSI acquisition, and fingerprinting parameters, over which the algorithm iterates to find an optimal match with the acquired data.
The simulation parameters are: repetition time TR, time between RF pulse and acquisition $T_0$, number of spokes $M$, RF pulse length $t_p$, RF pulse shape, spectral BW, number of FA, maximal flip angle $\mathrm{FA}_{\mathrm{max}}$ and number of isochromats. The latter defines the simulated number of spectral offsets contributing to one signal due to off-center resonances within one voxel caused by inhomogeneities of the external magnetic field $\Delta B_0$.
The fingerprinting parameters, which are estimated by the MRF algorithm, are the relaxation times $T_1$ and $T_2$, the off-resonance frequency $f_{\mathrm{off}}$ and the actual FA. The latter can used to calculate the $B_1^+$ maps via eq. (18). However in later evaluation, the direct result from the MRF estimation is shown, which is the actual FA, given in percentage of the nominal one.
Using all these parameters, the signal evolution is simulated. As a starting point, the ground state with no transversal magnetization is inserted into an RF pulse simulation algorithm[2]. The result sets the starting points for further Bloch simulations accounting for precession and relaxation during the readout. This sequence of RF simulation and following signal evolution is repeated for each FA, always using the prior result as the new starting point.
Afterwards, a weighting along the spectral domain is introduced via multiplication with the expected spectral pattern. This pattern is calculated from the number, chemical shift and relative amplitudes of the expected resonances.
Relative peak amplitudes were set to 1 for the highest peak at 0 ppm and the remaining ones were scaled according to the observations. In the case of EG, for the $^{13}$C MRSI data, the two off-center peaks at $\pm 4.48$ ppm were set to 0.5 and, for the $^{1}$H data, the downfield peak at $+1.63$ ppm to 0.5. For the $^{13}$C in vivo data, the spectral pattern was taken from a prior FID measurement, which is displayed in Figure 34 at the beginning of Section 4.3. The extracted values were one peak at $+4.23$ ppm with a relative amplitude of 0.73 and one at $-3.84$ ppm with 0.42.
A Gaussian lineshape was chosen with the width defined by the estimated in-voxel $\Delta B_0$, which was set to 10 Hz for the phantom and 20 Hz for the in vivo data. The overall shift of this distribution is given by the fingerprinting parameter $f_{\mathrm{off}}$.

[2] The code used for this implementation was provided by BA Hargreaves.

In a final step, the data is summed over all isochromats. The whole simulation results in one entry and is repeated for a new set of experimental parameters, filling the dictionary.
However, two different approaches for handling the spectral information were implemented, which change the dictionary calculation and subsequent matching slightly. In following sections, the differences between AMARES-based MRF and full-spectral MRF are described.

### 3.5.3. AMARES-based MRF

The AMARES-based MRF method compares the simulated dictionary with the peak amplitudes from the AMARES fit, similar to [38]. Hence, the simulation only calculates the first point of the signal evolution during the data acquisition. The subsequent weighting is done separately for every expected (and fitted) resonance. After summation of the isochromats, each final dictionary entry then consists of a fingerprint for each peak, which can be compared separately.
To find an optimal match, the dot products between acquired data and the simulations are calculated for all peaks. In the final step, these dot products are summed, using the maximal result to determine the best match.

### 3.5.4. Full-Spectral MRF

The full-spectral MRF approach compares the complete acquired spectral data with the simulations. Hence, the Bloch simulations are done in multiple steps analogue to the number of echoes $n$ of the acquisition. The weighting for the expected spectral pattern includes all resonances combined. After the summation of the isochromats, the dictionary yields fingerprints, which include the FIDs of all peaks over the full acquisition time.
In the full-spectral MRF matching process, the dot product is calculated for all $n$ acquired spectral points. Afterwards, all $n$ dot products are summed, analogue to the AMARES-based method. The maximal value then not only represents the best match to the FA pattern, but also to each spectrum.

### 3.5.5. Masking of the MRF Results

In order to exclude all matched voxels outside of the volume of interest, a masking threshold is defined. In this process, all voxels with an $L^2$ value smaller than 33% of the highest $L^2$ value were set to zero. This threshold showed the best distinction between phantom volume and void regions and was also applied to the in vivo data.

### 3.5.6. $B_1^+$-Determination via Double-Angle Mapping

In order to verify the novel MRF $B_1^+$ mapping techniques, double-angle (DA) mapping was employed as a reference. DA mapping uses two acquisition with the FAs $\alpha$ and $2\alpha$ to estimate the $B_1^+$ field. The repetition time TR is chosen long to ensure full relaxation of the system for each excitation. Then, the measured transversal magnetization $M_\alpha$ can be calculated from the ground state magnetization $M_0$ rotated with the FA $\alpha$, yielding following relations:

$$M_\alpha = M_0 \sin(\alpha) \tag{73}$$

$$\frac{M_\alpha}{\sin(\alpha)} = \frac{M_{2\alpha}}{\sin(2\alpha)} \tag{74}$$

Using the identity $\sin(2\alpha) = 2\sin(\alpha)\cos(\alpha)$, eq. (74) can be reordered to recalculate the actually transmitted FA from the acquired signal:

$$\alpha_{\text{actual}} = \arccos(\frac{M_{2\alpha}}{2M_\alpha}) \tag{75}$$

By using $\alpha_{\text{actual}}$ and eq. (18), the $B_1^+$ in each voxel can be calculated. However, in all following evaluation, $\frac{\alpha_{\text{actual}}}{\alpha}$ is used to calculate the relative actual flip angle in percentage.

The DA mapping applied in this thesis used TR = 2.5 s with $\alpha = 45°$ for the phantom and with $\alpha = 60°$ for the in vivo measurements. The total measurement time for both FA, $\alpha$ and $2\alpha$, was 10.9 min.

## 3.6. Measurement Protocols

In the following, the sequence parameters for all conducted measurements are listed.

### 3.6.1. EG Measurements

For all measurements in Section 4.1 using the 50-mL EG phantom, the following sequence parameters have been used:

| Sequence Parameters | |
|---|---|
| FOV | 200 mm |
| $\Delta$x | $(12.5\ \text{mm})^3$ |
| BW | 500 Hz |
| $n$ | 128 |
| TR | 260 ms |
| TA | 105 s |
| $M$ | 404 or 403 (403 needed) |
| FA | 60° |
| $t_p$ | 0.2 ms |
| RF shape | block |

Table 2: Sequence parameters for the measurements using the 50-mL ethylene glycol phantom. The number of spokes was $M = 404$ without use of the GAGA scheme and $M = 403$ spokes with it. The Nyquist criterion of $M = 403$ spokes was fulfilled in both cases. In the results regarding the ETS application, the native BW of 500 Hz was doubled to 1000 Hz.

The number of spokes was $M = 404$ for the state-of-the-art measurement in the beginning of Section 4.1 and for Section 4.1.2, without the use of the GAGA reordering. For Sections 4.1.2 and 4.1.5, with the use of GAGA, only $M = 403$ spokes have been acquired. This was due to implementation of the GAGA scheme, which was only applied for specific numbers of spokes. Also, in the case of Section 4.1.5, the BW was increased to 1000 Hz by using a ETS-factor of two. Additionally, a zerofilling factor of two was applied in spectral and spatial domain, doubling the respective resolution.

### 3.6.2. In Vivo [1-$^{13}$C]Pyruvate Measurements

For all in vivo measurements using [1-$^{13}$C]pyruvate, i.e. Sections 4.2.1, 4.2.2 and 4.2.3, the following parameters have been used:

| Sequence Parameters | |
|---|---|
| FOV | 180 mm |
| $\Delta$x | $(15\ \text{mm})^3$ |
| BW | 1000 Hz |
| $n$ | 64 |
| TR | 105 ms |
| TA | 6.3 s |
| $M$ | 60 (227 needed) |
| FA | 3° |
| $t_p$ | 0.2 ms |
| RF shape | block |

Table 3: Sequence parameters for the in vivo [1-$^{13}$C]pyruvate measurements. To fulfill the Nyquist criterion, $M = 227$ spokes were needed, leading to an undersampling factor of $\sim 4$.

A zerofilling factor of two was applied in spectral and spatial domain to double the respective resolution.

### 3.6.3. In Vivo [1,2-$^{13}$C]Pyruvate Measurements

For the $T_1$-compensated measurements in Sections 4.1.4 and 4.2.4, the following parameters have been used:

| Sequence Parameters | |
|---|---|
| FOV | 180 mm |
| $\Delta$x | $(15\ \text{mm})^3$ |
| BW | 2000 Hz using ETS = 2 |
| $n$ | 128 |
| TR | 140 ms |
| TA | 17 s |
| $M$ | 60 (227 needed) |
| FA | VFA with $T_1 = 12.73$ s |
| $t_p$ | 0.2 ms |
| RF shape | block |

Table 4: Sequence parameters for the in vivo [1,2-$^{13}$C]pyruvate measurements with $T_1$-compensation. To fulfill the Nyquist criterion, $M = 227$ spokes were needed, leading to an undersampling factor of $\sim 4$.

For the reference measurement in section 4.1.4, without $T_1$-compensation:

| Sequence Parameters | |
|---|---|
| FOV | 180 mm |
| $\Delta$x | $(15\ \text{mm})^3$ |
| BW | 1000 Hz |
| $n$ | 128 |
| TR | 140 ms |
| TA | 8.4 s |
| $M$ | 60 (227 needed) |
| FA | 12° |
| $t_p$ | 0.2 ms |
| RF shape | block |

Table 5: Sequence parameters for the in vivo [1,2-$^{13}$C]pyruvate measurements without $T_1$-compensation. To fulfill the Nyquist criterion, $M = 227$ spokes were needed, leading to an undersampling factor of $\sim 4$.

In both cases, a zerofilling factor of two was applied in spectral and spatial domain to double the respective resolution.

### 3.6.4. MRF using the EG phantom

The sequence parameters of the $^1$H and $^{13}$C MRF acquisitions using EG, featured in Section 4.3, were:

| Sequence Parameters | |
|---|---|
| FOV | 200 mm |
| $\Delta$x | $(25\ \text{mm})^3$ |
| BW | 500 Hz |
| $n$ | 64 |
| TR | 200 ms |
| TA | 402 s |
| $M$ | 20 (403 needed) |
| FA | VFA with max. 45° |
| $t_p$ | 2 ms |
| RF shape | sinc with TBW= 5 |

Table 6: Sequence parameters for the MRF acquisitions. To fulfill the Nyquist criterion, $M = 403$ spokes were needed, leading to an undersampling factor of $\sim 20$.

For the dictionary calculation, the following simulation and fingerprinting parameters were used:

| Simulation Parameters | |
|---|---|
| TR | 200 ms |
| $T_0$ | 1.25 ms |
| $t_p$ | 2 ms |
| BW | 500 Hz |
| $FA_{max}$ | 45° |
| $N$ | 100 |
| $n$ | 64 |
| isochromats | 101 |
| RF shape | sinc with TBW= 5 |

Table 7: Simulation parameters used to produce the MRF dictionary for the $^{1}$H and $^{13}$C EG data.

| Fingerprinting Parameters | |
|---|---|
| $T_1$ | [500:100:900] ms |
| $T_2$ | [20:20:100] ms |
| actual FA | [70:5:130]% |
| $f_{off}$ | [-4:2:4] Hz |

Table 8: Fingerprinting parameters, which are varied to find an optimal match to the acquired $^{1}$H and $^{13}$C MRF data of EG.

The time necessary to produce the above described dictionaries with 1750 entries for the AMARES approach was $\sim$ 0.8 h. The used processor was an Intel® Core™ Ultra 9 285K, 24 cores, 64 GB RAM. The data reconstruction required $\sim$ 9 min and the subsequent MRF matching time was $\sim$ 6 s.
For the full spectral approach, the dictionary production required $\sim$ 1.2 h, data reconstruction $\sim$ 1 min and the matching $\sim$ 6 min.

### 3.6.5. In Vivo MRF

The sequence parameters of the $^{13}$C in vivo MRF acquisitions, featured in Section 4.3, were:

| Sequence Parameters | |
|---|---|
| FOV | 200 mm |
| $\Delta$x | $(25\ \text{mm})^3$ |
| BW | 800 Hz |
| $n$ | 128 |
| TR | 200 ms |
| TA | 17:23 min |
| $M$ | 52 (101 needed) |
| FA | VFA with max. 60° |
| $t_p$ | 2 ms |
| RF shape | sinc with TBW= 5 |

Table 9: Sequence parameters for the MRF acquisitions. To fulfill the Nyquist criterion, $M = 101$ spokes were needed, leading to an undersampling factor of $\sim 2$.

For the dictionary calculation, the following simulation and fingerprinting parameters were used:

| Simulation Parameters | |
|---|---|
| TR | 200 ms |
| $T_0$ | 1.25 ms |
| $t_p$ | 2 ms |
| BW | 800 Hz |
| $\text{FA}_{\text{max}}$ | 60° |
| $N$ | 100 |
| $n$ | 128 |
| isochromats | 101 |
| RF shape | sinc with TBW= 5 |

Table 10: Simulation parameters used to produce the MRF dictionary for the in $^{13}$C vivo data.

| Fingerprinting Parameters | |
|---|---|
| $T_1$ | [300:100:900] ms |
| $T_2$ | [4:2:16] ms |
| actual FA | [50:5:110]% |
| $f_{\text{off}}$ | [-10:5:10] Hz |

Table 11: Fingerprinting parameters, which are varied to find an optimal match to the acquired $^{13}$C in vivo MRF data.

The time necessary to produce the above described dictionary with 3430 entries for the AMARES approach was $\sim$ 1.6 h. The used processor was an Intel® Core™ Ultra 9 285K, 24 cores, 64 GB RAM. The data reconstruction required $\sim$ 9 min and the subsequent MRF matching time was $\sim$ 16 s.
For the full spectral approach, the dictionary production required $\sim$ 3.2 h, data reconstruction $\sim$ 1 min and the matching $\sim$ 16 min.

# 4. Results

## 4.1. Advancing Radial Echo-Planar Spectroscopic Imaging Towards a Versatile Imaging Tool

In previous work, the radial echo-planar spectroscopic imaging (rEPSI) was successfully implemented to measure hyperpolarized 4D $^{13}$C MRSI datasets [51]. As shown in Figure 14, volumetric intensity maps with highly resolved $^{13}$C spectra could be acquired for the thermally polarized ethylene glycol (EG) phantom. Additional processing pipelines allowed for either an added or interleaved recombination of odd and even datasets, as well as an extraction of non-localized, highly time-resolved $T_1$ curves of HP substrates.

However, further advancements were required to unlock the full potential of data sampling via the rEPSI sequence. In the following, several techniques and features are presented, which allow highly improved data acquisition using the rEPSI, tailored to hyperpolarized $^{13}$C experiments:

(i) $k$-space undersampling, (ii) optimized spoke ordering, (iii) sliding window (SW) reconstruction, (iv) variable flip angle (VFA) excitation, and (v) expansion of acquired spectral bandwidth by echo-train-shifting (ETS).

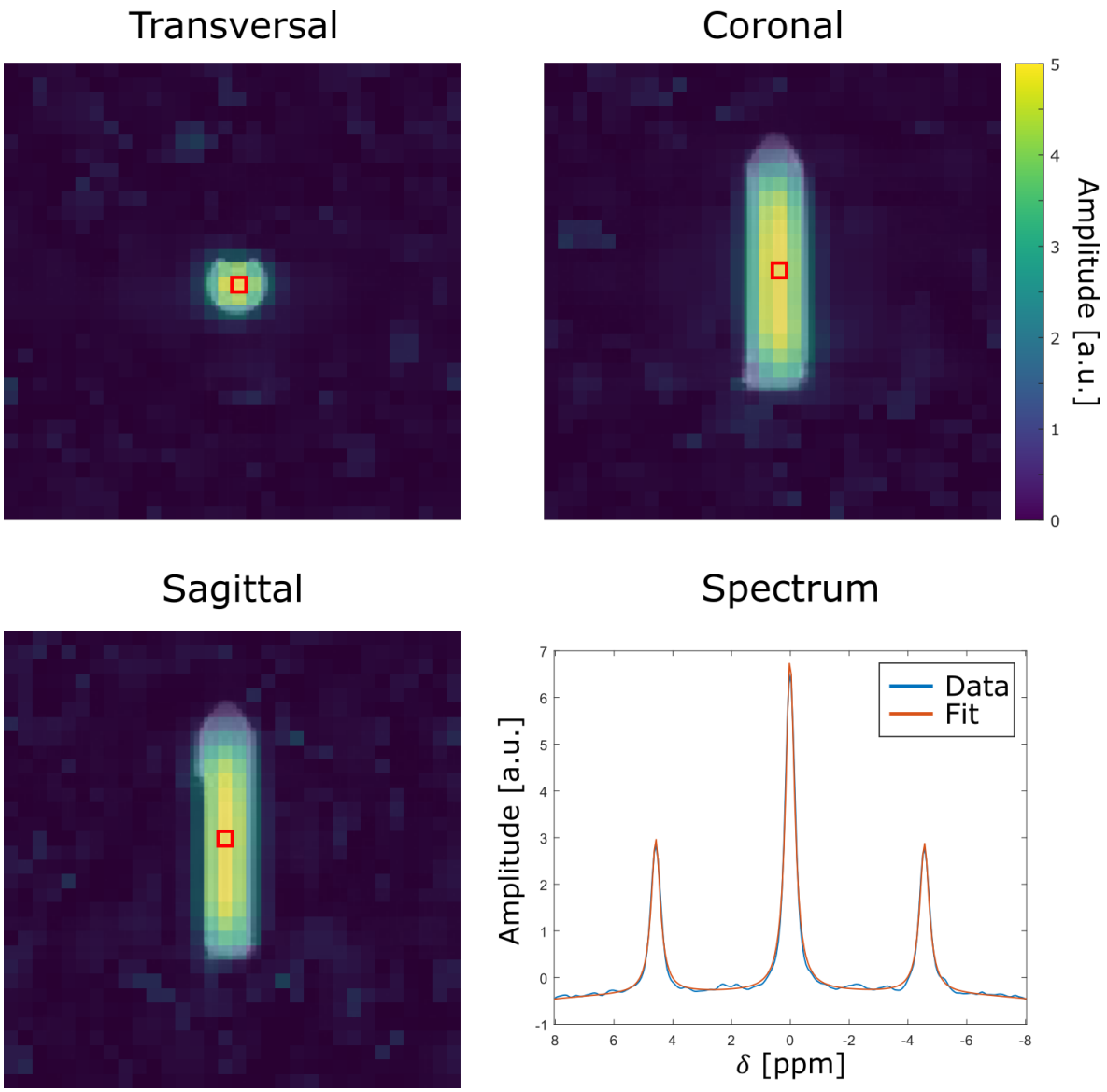


Figure 14: Previously implemented state-of-the-art rEPSI sequence. Shown are $^{13}C$ intensity maps of the central peak for one slice in transversal (top left), coronal (top right) and sagittal (bottom left) view, overlaid with an anatomical image. Additionally, a representative fitted spectrum (bottom right) of a voxel within the phantom (red square) is presented.

### 4.1.1. Undersampling

The rapidly decaying hyperpolarized signal requires the measurement time to be as short as possible ($< 1$ min) while large image data matrices are targeted. Hence, the robustness of the rEPSI acquisition regarding undersampling, i.e. the acquisition of less spokes, was investigated, comparing a fully sampled to a highly undersampled $^{1}$H intensity map of EG in Figure 15. Especially at higher undersampling, more pronounced noise-like patterns can be observed in void regions, originating from undersampling artifacts of the center resonance of EG. Analogous results for the $^{13}$C data can be observed in Figure 16. These artifacts arise when the number of acquired spokes does not fulfill the Nyquist criterion, as stated in eq. (58).
Naturally, with a lower number of acquired spokes, the total measurement time also decreased. The fully sampled dataset ($M = 403$) required 105 s, but with an undersampling factor of five ($M = 81$) this reduced to 21 s and finally, with a factor of 20 ($M = 20$), the total measurement time was only 5 s.

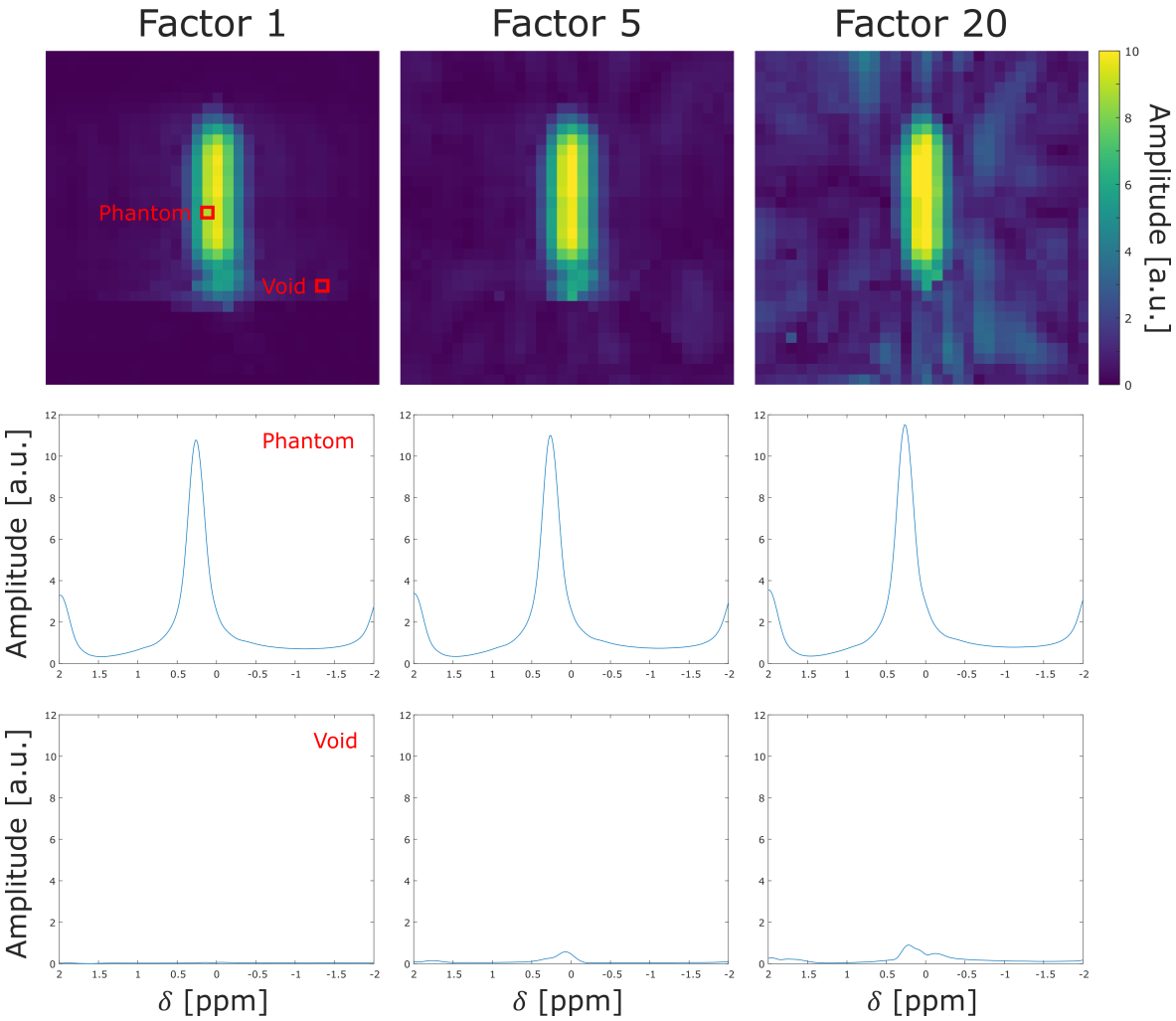


Figure 15: Coronal slice of the $^{1}$H intensity map for the EG phantom (top row). From left to right the undersampling factor increases from 1 to 5 and 20. Representative spectra are shown for a voxel within the phantom (middle row) and the void region (bottom row).

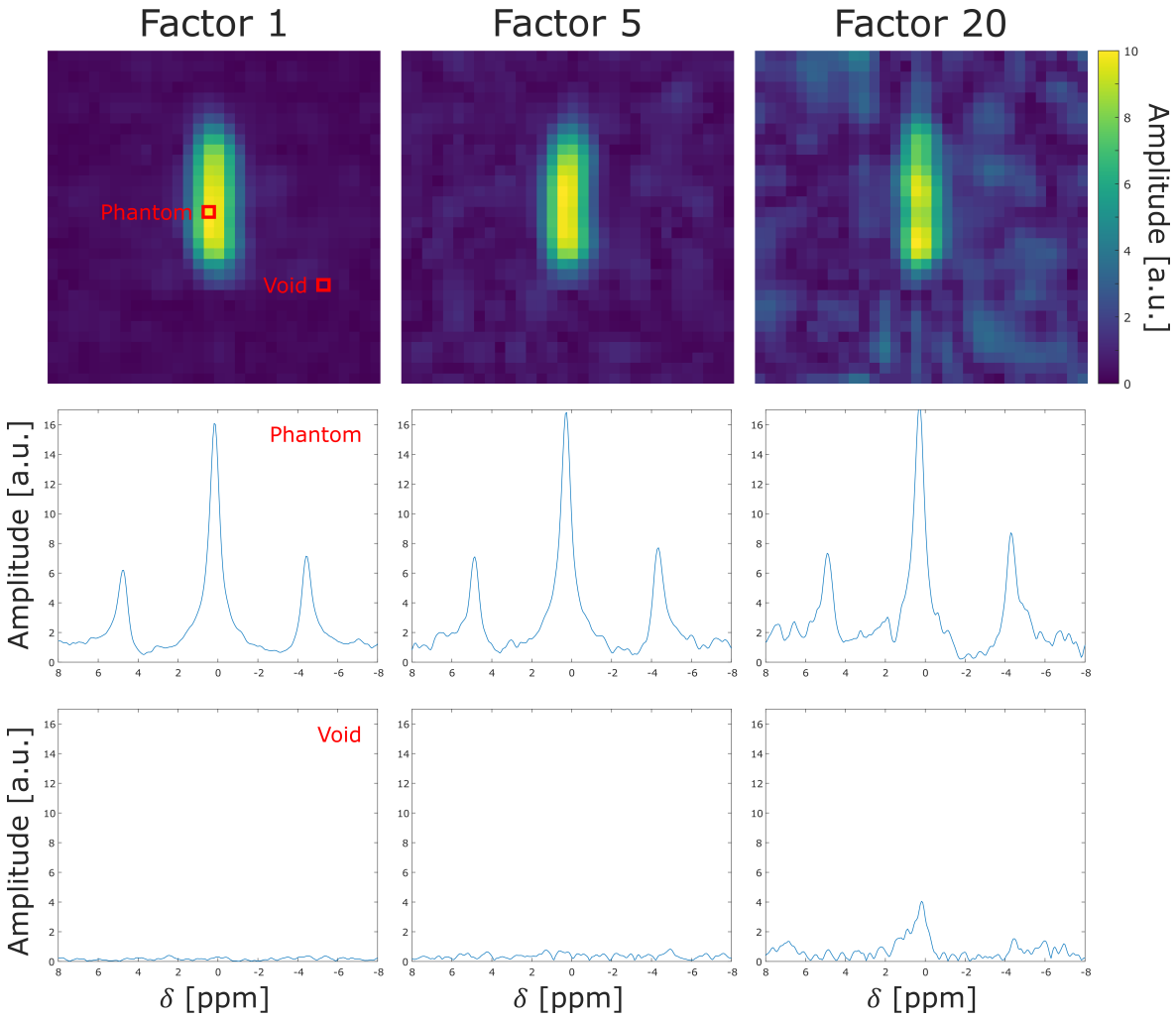


Figure 16: Coronal slice of the $^{13}C$ intensity map for the EG phantom (top row). From left to right the undersampling factor increases from 1 to 5 and 20. Representative spectra are shown for a voxel within the phantom (middle row) and the void region (bottom row).

Figure 17 evaluates the increase in artifact amplitude with a higher undersampling factor for $^{1}$H and $^{13}$C , respectively. The average relative artifact amplitude exceeded the $3\sigma$ range of the fully sampled dataset at an undersampling factor of five. At this point, much more pronounced patterns in the void region were also observed by qualitatively comparing the artifacts in all maps. Hence, this undersampling factor was chosen as a cut-off to which a reconstruction without advanced algorithms is possible and was applied for later in vivo measurement.

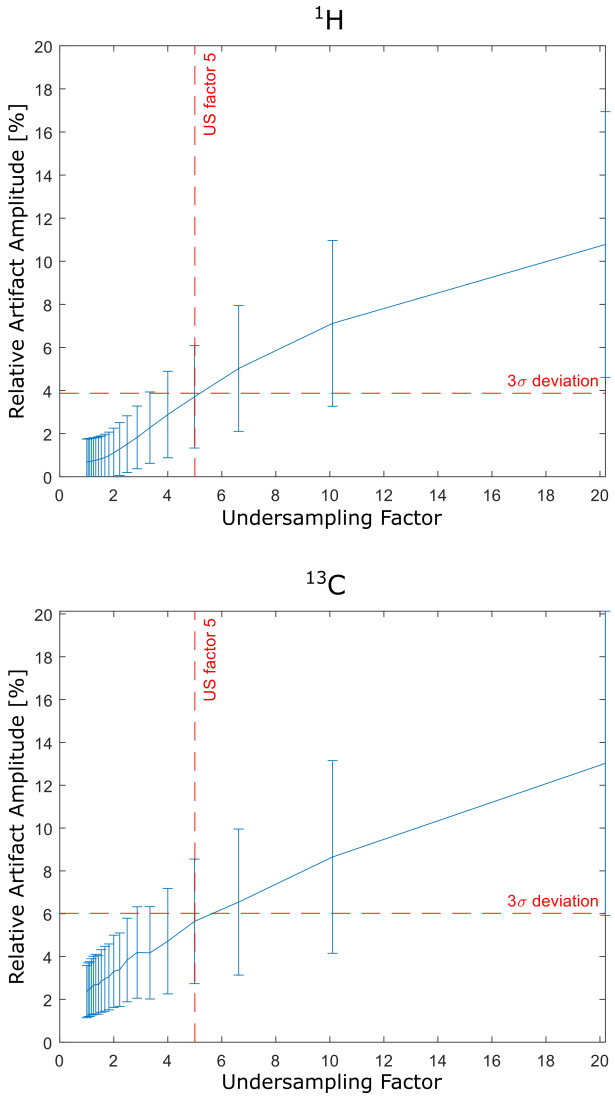


Figure 17: Increase of artifact amplitude relative to the $^{1}$H (top) and the $^{13}$C (bottom) signal amplitude in percentage in dependency on the undersampling (US) factor. The $3\sigma$ line of the fully sampled dataset was chosen as a cut-off for the maximally feasible undersampling factor.

### 4.1.2. Gapped Arrangement of Golden Angles

To increase the homogeneity of the $k$-space coverage as much as possible, a gapped arrangement of golden angles (GAGA) was implemented [22], which changes the order in which the spokes are acquired. This is especially important for HP experiments, where the signal intensity decreases with the $T_1$ relaxation time, what results in a time-dependent weighting of the acquired datapoints and, with that, in possible image blurring.

Figure 18 presents two acquired $^{13}$C datasets of EG, one with the upwards spiraling golden angle acquisition and one with the reordering through the GAGA scheme. For both datasets, a $T_1$ decay filter of 13 s was applied in post-reconstruction to simulate an in vivo HP experiment with an exponentially decreasing spoke intensity. The comparison shows a significant blurring for the normal golden angles in coronal direction with smaller oscillating artifacts in the sagittal slice. In contrast, the GAGA acquisition agrees with the phantom geometry and has defined borders to the void areas with no blurring in either spatial orientation.

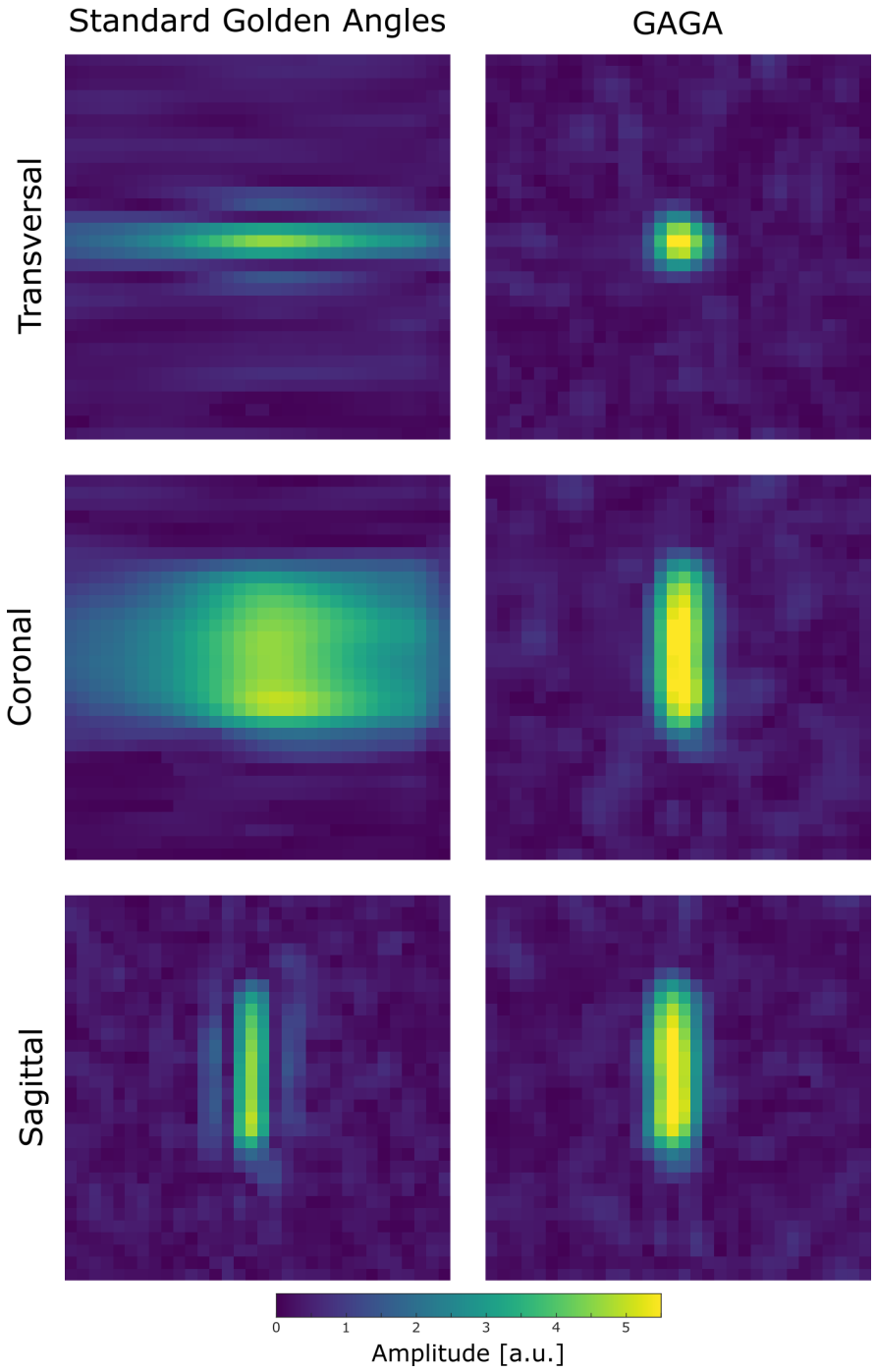


Figure 18: Comparison of golden angle acquisition schemes for the EG phantom. In post-reconstruction, a $T_1$ decay of 13 s was applied to the spoke intensities to simulate an in vivo HP experiment. Shown are intensity maps for the standard golden angle upwards spiral (left column) and the reordering through the golden angle gapped arrangement (GAGA) scheme (right column) for one transversal (top), coronal (middle) and sagittal (bottom) slice.

### 4.1.3. Sliding Window Reconstruction

Another advantage of the homogeneous radial $k$-space sampling via the GAGA scheme, is the usage of a sliding window (SW) reconstruction. Here, a fully sampled rEPSI dataset with an image matrix size of $16 \times 16 \times 16$ and $M = 403$ spokes was used. Just like in the previous section, a $T_1$ decay of 13 s was applied in post-reconstruction. Then, this fully sampled dataset was divided into $N_{\text{sub}} = 384$ subsets with $M_{\text{sub}} = 20$ spokes each. The resulting strongly-undersampled subframes allow for the dynamic investigation with a fine temporal spacing $\Delta t = \text{TR} = 260$ ms, as shown in Figure 19. Through the SW reconstruction, the subsets yield a high undersampling factor of $\sim 20$. The fitted $T_1$ decay of the amplitude of the central peak yields a value of $(12.80 \pm 0.27)$ s. The true value of 13 s is therefore within the $1\sigma$ range.

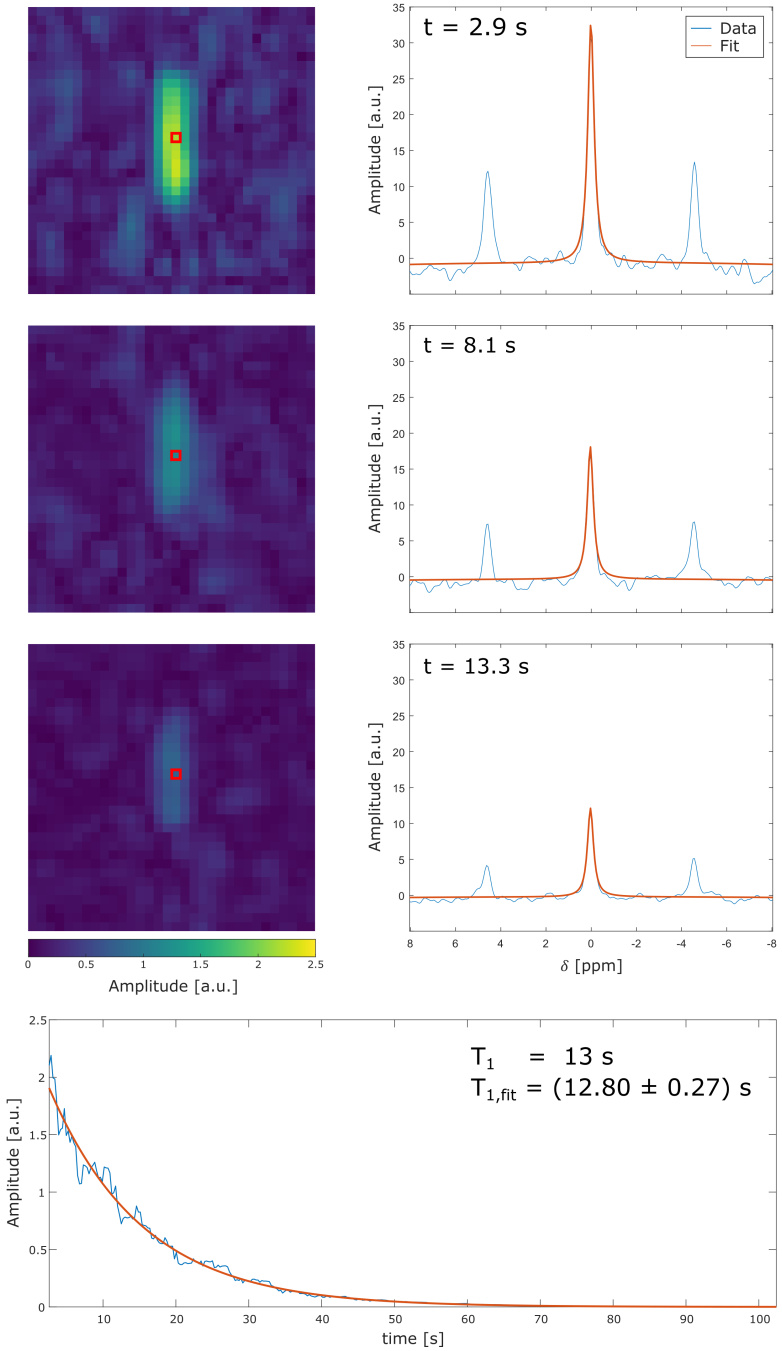


Figure 19: Presentation of the sliding window reconstruction of the EG phantom. In post-reconstruction, a $T_1$ decay of 13 s was applied to the spoke intensities to simulate an in vivo HP experiment. The fully sampled dataset with $M = 403$ spokes is divided into $N_{\text{sub}} = 384$ subsets with the temporal spacing $\Delta t = \text{TR} = 260$ ms. An example coronal slice of the fitted central peak (left column) is shown for three timepoints (2.60 s, 8.06 s, 13.26 s) with a representative fitted spectrum (right column) of a voxel within the phantom (red square). Finally, all fitted amplitudes are plotted over time (from 2.60 s until 102.44 s) with a fitted $T_1$ decay of $(12.80 \pm 0.27)$ s.

Furthermore, the steps $\Delta t$ in which the subset window progresses along the time axis can be changed. Figure 19 used the smallest possible step size of one spoke with $\Delta t = \mathrm{TR} = 260$ ms. The maximal possible step size is $M_{\mathrm{sub}} = 20$ spokes, which results in $\Delta t = 20 \times \mathrm{TR} = 5.2$ s. In Figure 20 the resulting fitted $T_1$ curves are presented for the step sizes of 1, 10 and 20 spokes.

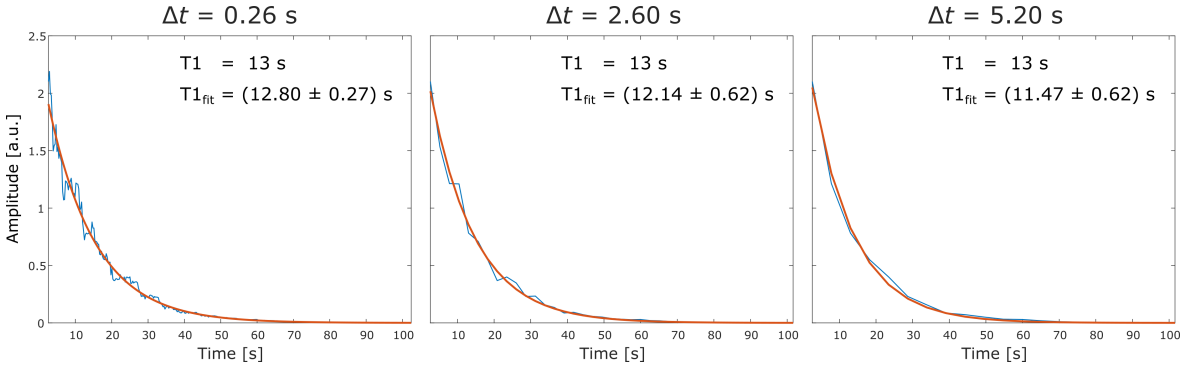


Figure 20: SW reconstruction of the EG phantom with a changing step size of the window. In post-reconstruction, a $T_1$ decay of 13 s was applied to the spoke intensities to simulate an in vivo HP experiment. The window size remains constant with $M_{\mathrm{sub}} = 20$, however, the number of subsets $N_{\mathrm{sub}}$ and with that, the temporal spacing $\Delta t$ differs. From left to right, these parameters are $N_{\mathrm{sub}} = [384, 40, 20]$ and $\Delta t = [0.26, 2.60, 5.20]$ s. The fitted amplitude of one voxel is plotted over time, yielding value for the $T_1$ decay of $(12.80 \pm 0.27)$ s, $(12.14 \pm 0.62)$ s and $(11.47 \pm 0.62)$ s, respectively.

A significant oscillation in signal intensity can be observed over the time course, deviating from the underlying $T_1$ decay. This fluctuation becomes more prominent with a decreasing window step size and $\Delta t$. Nevertheless, the fitted $T_1$ value with the smallest $\Delta t$ is not only closest to the true one but also shows the smallest error margin. Naturally, it is also the dataset with the most datapoints.

A correction for the intrinsic signal oscillation was attempted by applying the SW reconstruction to the same data but without the $T_1$ decay. The signal variations within the steady signal amplitude are assumed to only exhibit the individual spoke contributions in each subset due to the specific signal distribution in $k$-space. The resulting data was used to rebalance the dynamic plot from Figure 19, resulting in a signal curve with much less oscillations, as displayed in Figure 21. Afterwards, the decay was fitted again, now yielding a constant of $T_1 = (12.82 \pm 0.10)$ s. This value agrees very much with the data before the correction, however, the error range is strongly reduced.

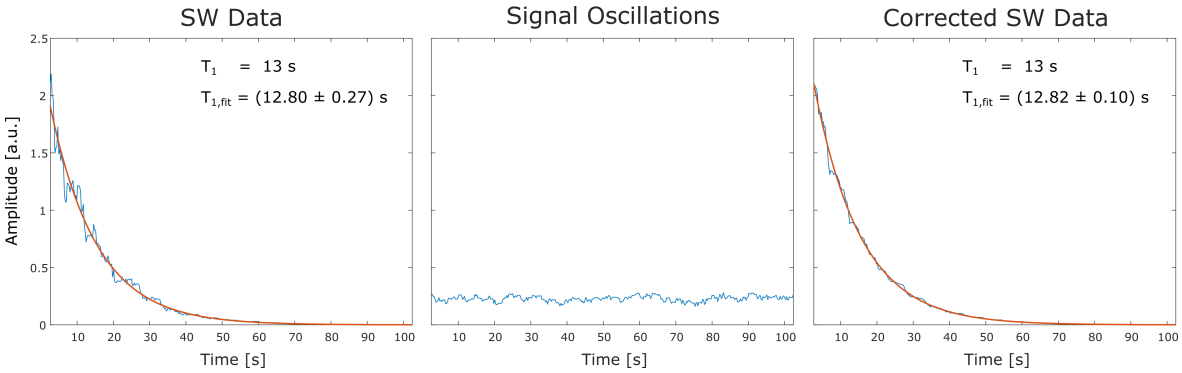


Figure 21: Fitted $T_1$ decay of a representative voxel from the $^{13}$C EG data after the SW reconstruction (left). The same data was reconstructed without simulated $T_1$ decay, only showing the $k$-space specific signal oscillations (middle). Finally, the SW data was corrected for these oscillations to produce a smoother decay curve (right).

Finally, both SW datasets, the corrected as well as the original one, were quantified in every voxel, resulting in $T_1$ maps over the full FOV, as shown in Figure 22. As suggested by the decreased fitting error, the $T_1$ maps are much smoother after the applied correction.

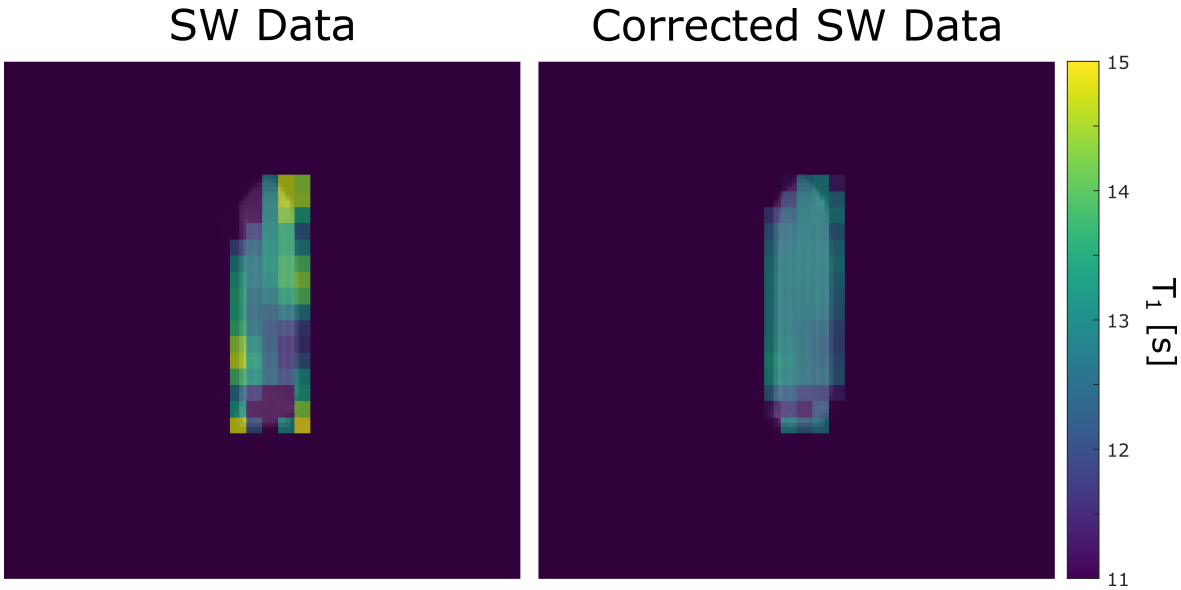


Figure 22: $T_1$ maps extracted through the SW reconstruction before (left) and after correction (right) for the $k$-space dependent signal oscillations, overlaid with an anatomical image.

### 4.1.4. $T_1$-Compensating Variable Flip Angle Scheme

To ensure a steady signal intensity throughout the acquisition of all spokes, which is a requirement for the later used ETS, a $T_1$-compensation through exponentially increasing flip angles was applied. Figure 23 shows the data extracted from the $k$-space centers of two in vivo measurement after injection of HP [1,2-$^{13}$C]pyruvate, once acquired with a constant FA and once with the use of the $T_1$-compensation, assuming a $T_1$ of 12.73 s.

In both cases, the non-localized spectrum was fitted and the amplitude for the upfield [1-$^{13}$C]pyruvate peak plotted over time. While the constant FA shows a $T_1$ relaxation curve, the compensated dataset does not show variations in signal intensity. Only for the last 10% of acquisitions a slight overcompensation can be seen, increasing this spoke intensity compared to the remaining ones.

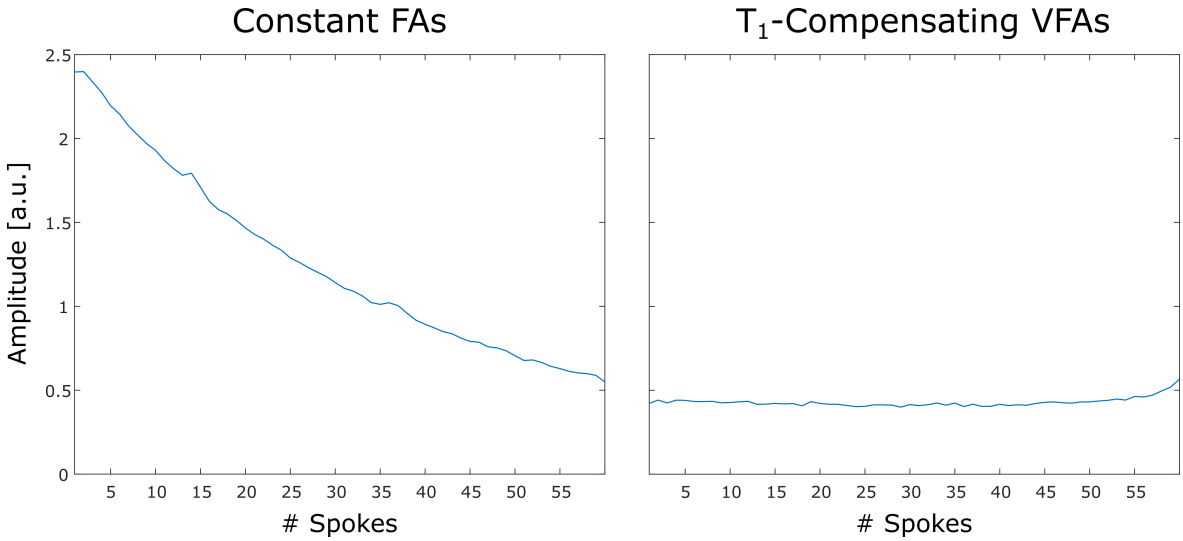


Figure 23: Comparison of two in vivo measurements with injection of hyperpolarized [1,2-$^{13}$C]pyruvate. Shown are the spoke intensities extracted from the $k$-space center points for a standard acquisition using a constant FA (left) vs. the $T_1$-compensated VFA scheme (right).

### 4.1.5. Echo-Train-Shifting

A particular challenge in EPSI is the acquisition of high spectral bandwidths, as an increased gradient rise time is necessary, which is restricted through the scanner's hardware (see Section 3.3.1). Two possible alternatives to increase the spectral bandwidth are the recombination of the acquired odd and even datasets during reconstruction or the use of echo-train-shifting (ETS), which are explained in Sections 3.3.7 and 3.4.4, respectively.

To evaluate those techniques, the ETS is compared to the recombination approach using the same data of a EG measurement. As shown in Figure 24, the bandwidth was doubled from approximately 32 ppm to 64 ppm in both cases, using an ETS factor of two. The spectra from a voxel within the phantom both show the peak triplet from EG, however, for the recombination case significant ghosting artifacts can be observed. Also, more phase inhomogeneities can be seen in the recombined dataset, complicating the fit. In contrast, the ETS approach enables accurate quantification without phasing artifacts.

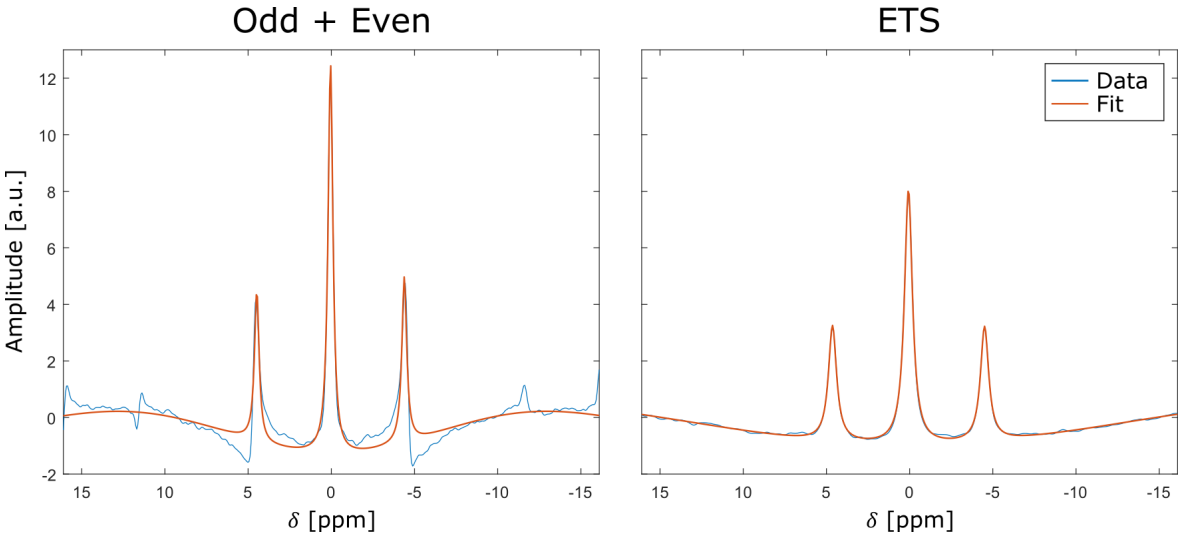


Figure 24: Comparison of the interleaved recombination of odd and even (left) vs. the odd dataset after use of ETS (right). In both cases a central voxel within EG phantom was chosen.

Next, the ETS was tested against stability to a $T_1$ decay ($T_1$ = 13 s) in the spoke intensities and two different acquisition orders (see Figure 25). The left plot again shows the ETS spectrum from before, but rescaled to serve as a reference without present $T_1$ decay.
For the first acquisition order, the two ETS acquisitions of one spoke have once been acquired right after one another. The resulting spectrum is shown in the middle, where all three peaks can clearly be evaluated, as the artifacts arising from the $T_1$ decay are minimal.
In the second case, first all spokes have been acquired once and the second ETS run started afterwards. The spectrum, displayed to the right, shows large ghosting artifacts due to the different spoke ordering, since the two combined ETS acquisitions have vastly different signal intensities through progressed $T_1$ effects.

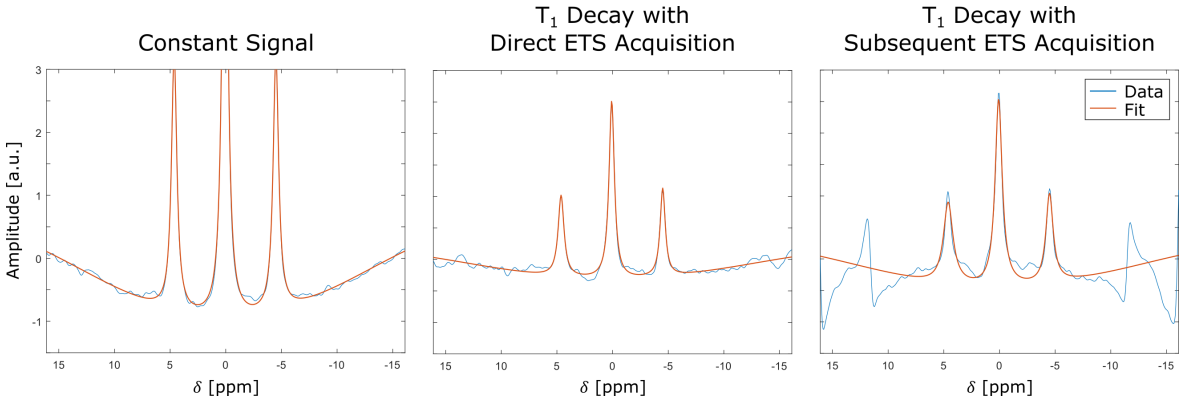


Figure 25: A representative spectrum is shown after the use of ETS with steady signal intensity (left) and an exponentially decreasing intensity (middle and right). For the spectrum in the middle, first each spoke was acquired twice for both ETS, while for the spectrum on the right, all spokes were acquired and the ETS applied subsequently. In all three cases a central voxel within EG phantom was chosen.

In conclusion, for the [1,2-$^{13}$C]pyruvate in vivo acquisition, presented in Section 4.2.4, a direct ETS acquisition was used, as this approach does not only produce the least phasing and ghost artifacts, but also is most stable in combination with a present $T_1$ decay.

## 4.2. Application of Radial EPSI to Metabolic Imaging of Hyperpolarized $^{13}$C-Pyruvate In Vivo

In order to demonstrate the feasibility of the implemented advanced rEPSI for use in metabolic imaging with high spatio-spectral and temporal resolution, an in vivo proof-of-principle study with hyperpolarized $^{13}$C-pyruvate was conducted.
First, a validation using single-labeled [1-$^{13}$C]pyruvate was performed with focus on the temporal resolution, i.e. capturing metabolic images at multiple timepoints after injection [54].
As a second step, the implemented advancements were applied to double-labeled [1,2-$^{13}$C]pyruvate to demonstrate the benefits of rEPSI in scenarios with a high spectral complexity [55].

### 4.2.1. Metabolic Imaging with [1-$^{13}$C]Pyruvate

For the first time, the volumetric rEPSI sequence was applied in vivo after injection of hyperpolarized [1-$^{13}$C]pyruvate. Through robust undersampling with a factor of approximately four, large isotropic data matrices of 16 with a high spectral bandwidth of 1 kHz were acquired in just about 6 s. The spectral data within each voxel was quantified with AMARES fitting, resulting in three-dimensional maps for each detectable $^{13}$C-labeled metabolite. Representative slices through a central point are presented in Figure 26, with the intensity distribution for [1-$^{13}$C]pyruvate, [1-$^{13}$C]lactate and [1-$^{13}$C]alanine. For all metabolites, the signal is highest near the heart, with pyruvate reaching into the lower intestines and lactate being more present in the leg muscles.

Figure 27 shows the fitted spectral data for one central abdominal voxel, as well as one peripheral voxel in the right leg (red squares in Figure 26).
In the abdomen all peaks are well-defined with a high SNR, allowing for an optimal fit. The peripheral voxel exhibits a split central peak for pyruvate, as well as a lower SNR, complicating a good fitting process.
Through the short acquisition time of 6.3 s, eight 4D dataset could be obtained. This allowed of an evaluation of the peak amplitudes over time, showing the temporal evolution of the $T_1$ decay for all metabolites as well as the initial build-up for downstream metabolites lactate and alanine. Due to the worse fit in the peripheral voxel, less smooth signal evolutions are present, but nevertheless, all expected dynamics can be observed.

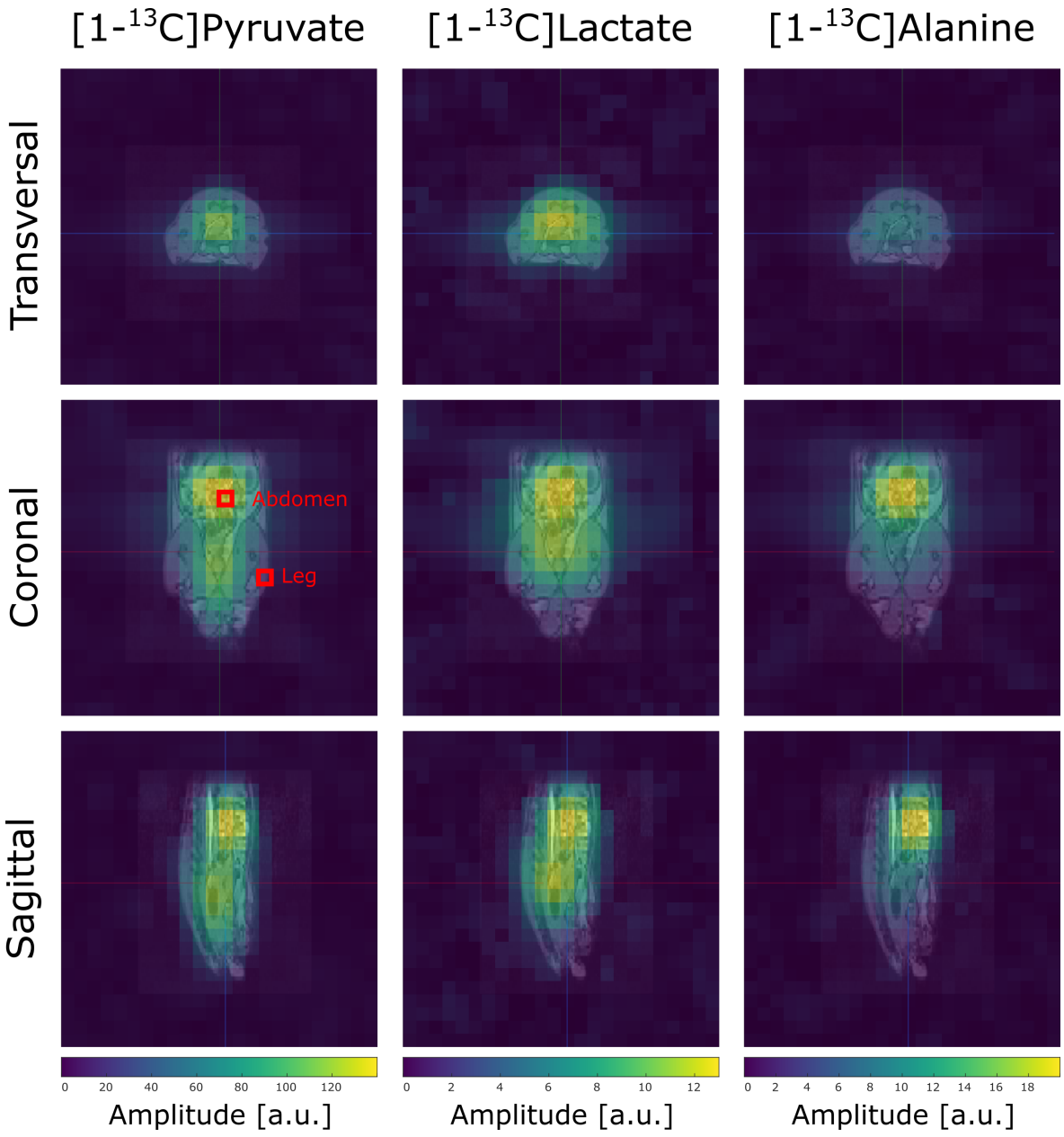


Figure 26: Intensity maps for a hyperpolarized $^{13}$C measurement of a rat, showing the distribution of [1-$^{13}$C]pyruvate, [1-$^{13}$C]lactate and [1-$^{13}$C]alanine (from left to right) for a slice in transversal, coronal and sagittal (from top to bottom) view. The two red squares indicate the voxel positions within abdomen and the right leg muscle of the shown spectra in Figure 27.

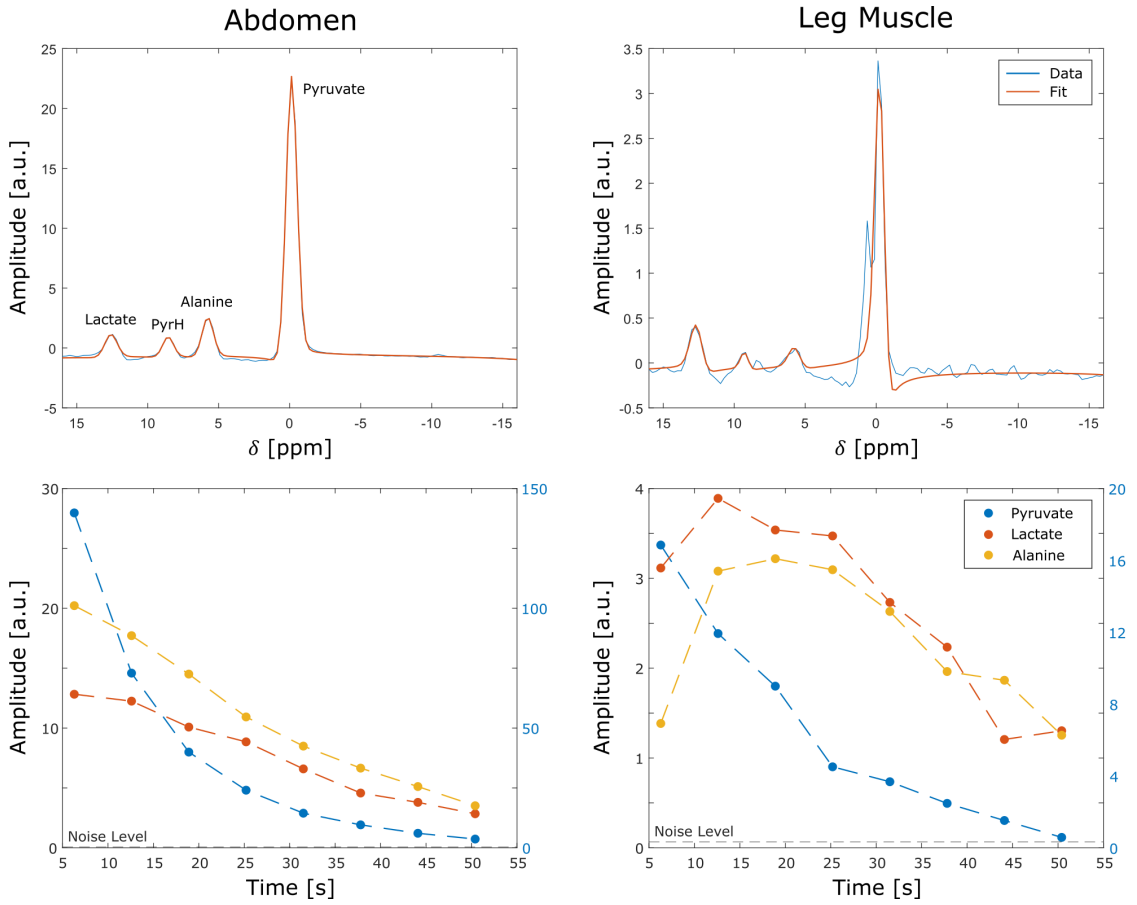


Figure 27: A representative spectrum from the abdomen of the rat (top left) and from a peripheral voxel within the right leg muscle (top right). In the bottom row, the fitted amplitudes of [1-$^{13}$C]pyruvate, [1-$^{13}$C]lactate and [1-$^{13}$C]alanine are plotted over all eight acquired timepoints with a temporal spacing of 6.3 s. Note, that for a better visualization, the amplitude of [1-$^{13}$C]pyruvate was divided by five, as it is indicated by the blue axis on the right.

### 4.2.2. SW Reconstruction of In Vivo [1-$^{13}$C]Pyruvate Data

In order to explore the benefits of radial sampling even further, a sliding window (SW) reconstruction was now applied to the representative in vivo measurement of Section 4.2.1. The result is shown in Figure 28, where $N_{\text{sub}} = 41$ subsets were extracted from each acquired undersampled dataset of $M = 60$ spokes. For all eight repetitions, this results in a total of $8 \times 41 = 328$ timepoints with a spacing of TR = 105 ms. However, between all eight repetitions, e.g. timepoints 41 and 42, the temporal spacing is $20 \times 105$ ms = 2.1 s, since a new GAGA scheme is started and a new subset can only be reconstructed after acquisition of all $M_{\text{sub}} = 20$ spokes. As a consequence of the SW reconstruction, the undersampling factor was increased from a initial value of $\sim 4$ to $\sim 11$, while offering a much higher temporal resolution. For [1-$^{13}$C]lactate, this increased temporal detail even revealed the initial metabolic build-up, which could not be detected before.

Especially for the high-SNR metabolite [1-$^{13}$C]pyruvate, it can be seen that the flickering in intensity follows the same pattern, repeating at every of the eight acquisitions, i.e. repetition of the same GAGA scheme.

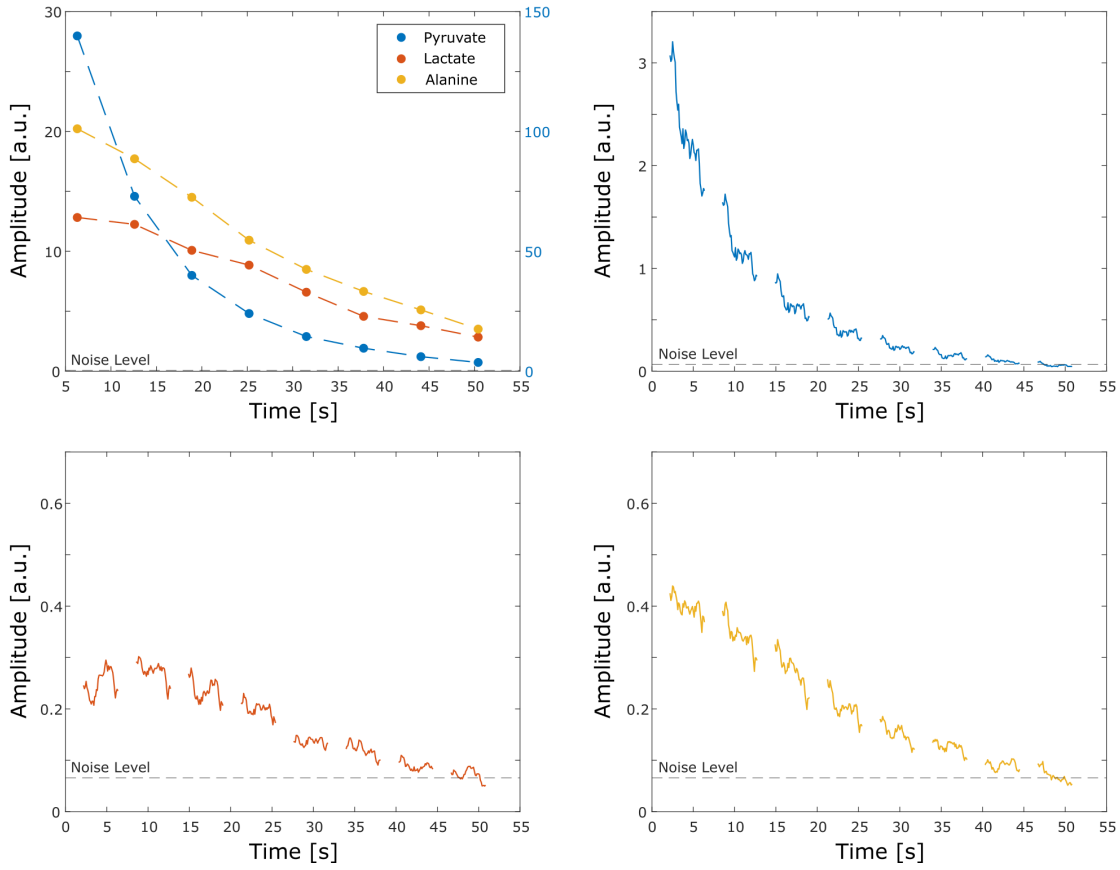


Figure 28: Dynamic data obtained by the SW reconstruction of the representative rat measurement using [1-$^{13}$C]pyruvate. On the top left, all observed metabolites are plotted over all eight acquired timepoints, each consisting of $M = 60$ spokes. Here, the pyruvate amplitude was divided by five for visualization purposes, as indicated by the blue axis on the right. Through a SW reconstruction, each timepoint is divided into 41 further subframes, shortening the temporal spacing from 6.3 s to 105 ms. Note the larger time gap of 2.1 s between each of the eight acquisitions, needed to acquire the minimally required subset size of $M_{\text{sub}} = 20$.

In a final analysis of the in vivo HP [1-$^{13}$C]pyruvate data, the quantification of the $T_1$ time of pyruvate via the three methods was compared, using the $k$-space centers, the eight repeated measurements and the SW reconstruction. In Figure 29, the non-localized FID from the first method is shown, as well as the resulting $T_1$ maps from the other two methods, repsectively.

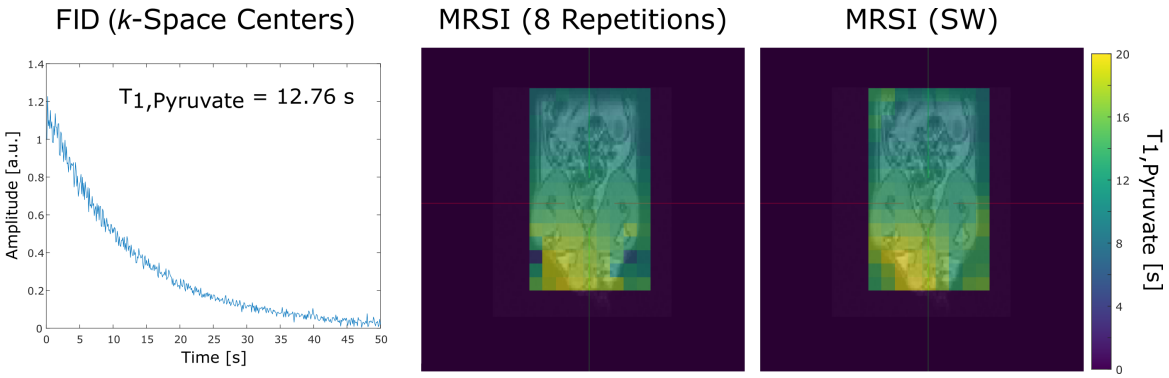


Figure 29: Determined $T_1$ values for the three different data reconstruction methods: 1) only using the $k$-space centers (left), 2) standard reconstruction of the eight timepoints (middle) and 3) expansion of the eight points by application of the sliding window (SW) reconstruction (right). The $k$-space centers only provide non-localized spectra, hence only the overall [1-$^{13}$C]pyruvate decay over time is shown with a value of $T_1 = 12.76$ s. For the other two spatially resolved reconstruction methods, the $T_1$ maps of a representative coronal slice are presented.

| FID ($k$-Space Centers) | MRSI (8 Repetitions) | MRSI (SW) |
|---|---|---|
| $12.76 \pm 0.15$ s | $12.51 \pm 3.10$ s | $13.11 \pm 2.99$ s |

Table 12: Comparison of the determined $T_1$ times from three different data reconstruction methods: 1) using the $k$-space centers only, 2) conventional reconstruction of the eight repetitions and 3) expansion of the eight points by application of the sliding window (SW) reconstruction.

The determined $T_1$ times of the shown coronal slice are displayed in Table 12. All values agree within the given standard deviation. The $k$-space center reconstruction yields the smallest error, most likely due to the highest SNR.
Additionally to the standard deviation arising from evaluating all voxels in the shown coronal slice, also the average fitting uncertainty was extracted, similar to Figure 21. This error is 1.27 s for the standard eight point reconstruction and 0.72 s for the SW reconstruction, demonstrating a more accurate evaluation via AMARES through the additional timesteps.

In conclusion, the applied SW reconstruction allowed for a more detailed investigation of the metabolic dynamics. Even with present signal oscillations, the finer temporal resolution revealed dynamic processes, like parts of the [1-$^{13}$C]lactate build-up, and enabled a more accurate $T_1$ quantification.

### 4.2.3. Pilot Study to Assess the Response to Radiation Therapy using [1-$^{13}$C]Pyruvate

After demonstrating the feasibility of the rEPSI sequence for in vivo measurements of hyperpolarized [1-$^{13}$C]pyruvate, a pilot study with tumor-bearing rats was conducted. In this study, not only possible metabolic changes after a irradiation of the tumor with heavy ions were investigated, but also the reproducibility of this MRSI technique, when applied on multiple days and to different subjects.

Taking advantage of the compatibility to a high undersampling, as demonstrated in Section 4.1.1, it was possible to shorten the acquisition time to consecutively acquire multiple MRSI datasets. In turn, the dynamic behavior for [1-$^{13}$C]pyruvate, [1-$^{13}$C]lactate and [1-$^{13}$C]alanine within the healthy leg, as well as the tumor volume, was captured, similar to Section 4.2.1. Using the area under the curve (AUC) values from [1-$^{13}$C]lactate and [1-$^{13}$C]pyruvate, the corresponding metabolite ratios could be determined in each voxel and displayed as lactate-to-pyruvate ratio maps (see Figure 30).

On the day after the measurement, the rat was treated with radiotherapy. Then, this experiment was repeated after one, two and three weeks, enabling the assessment of the localized change in the lactate-to-pyruvate ratio over time in response to the radiation treatment (see Figure 31).

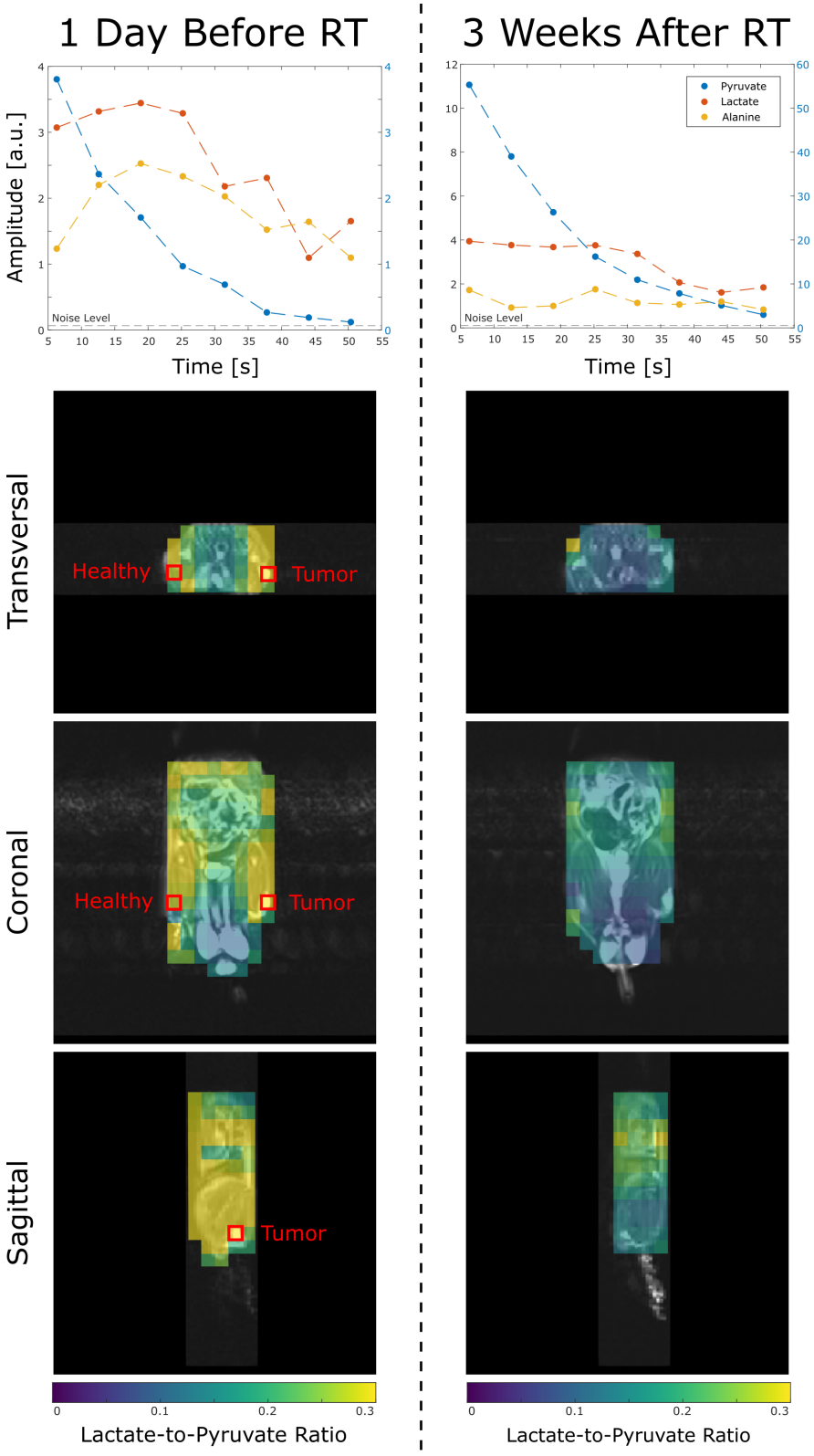


Figure 30: Comparison of the dynamic MRSI data obtained one day before the radiotherapy (RT) vs. three weeks after. The top row shows the eight time-points from a voxel within the tumor volume. Here, the pyruvate amplitude was divided by five for visualization purposes, as indicated by the blue axis on the right. Below that, lactate-to-pyruvate AUC ratio maps are shown in a transversal, coronal and sagittal slice through the tumor. For better visibility, the maps were masked, only showing the ratio values within the rat volume.

This study was conducted on eight rats in total, two of which were excluded, since only a single lactate-to-pyruvate ratio datapoint could be acquired. All recorded ratios are plotted in Figure 31. Note, that not all ratios could be acquired for every rat due to occasional failure of the d-DNP system.
In general, all acquired data showed consistency in the relative metabolite signal intensities, their distribution within the rat, as well as the dynamic behavior regarding metabolic conversion and $T_1$ decay.
Nevertheless, quantification of metabolic conversions proved especially difficult for the tumor location. This is due to the low spectral quality in the peripheral regions, i.e. the right hind leg, and ultimately leads to fluctuations in the lactate-to-pyruvate ratios, which is seen as the large ranges of the boxplots in Figure 31. Hence, no significant differences in metabolism could be observed after application of the radiotherapy when comparing the healthy and tumor-bearing leg. However, a general decrease in lactate-to-pyruvate ratio was noted when comparing the data before irradiation with the one after three weeks, which might hint towards a systematic effect of the radiation.

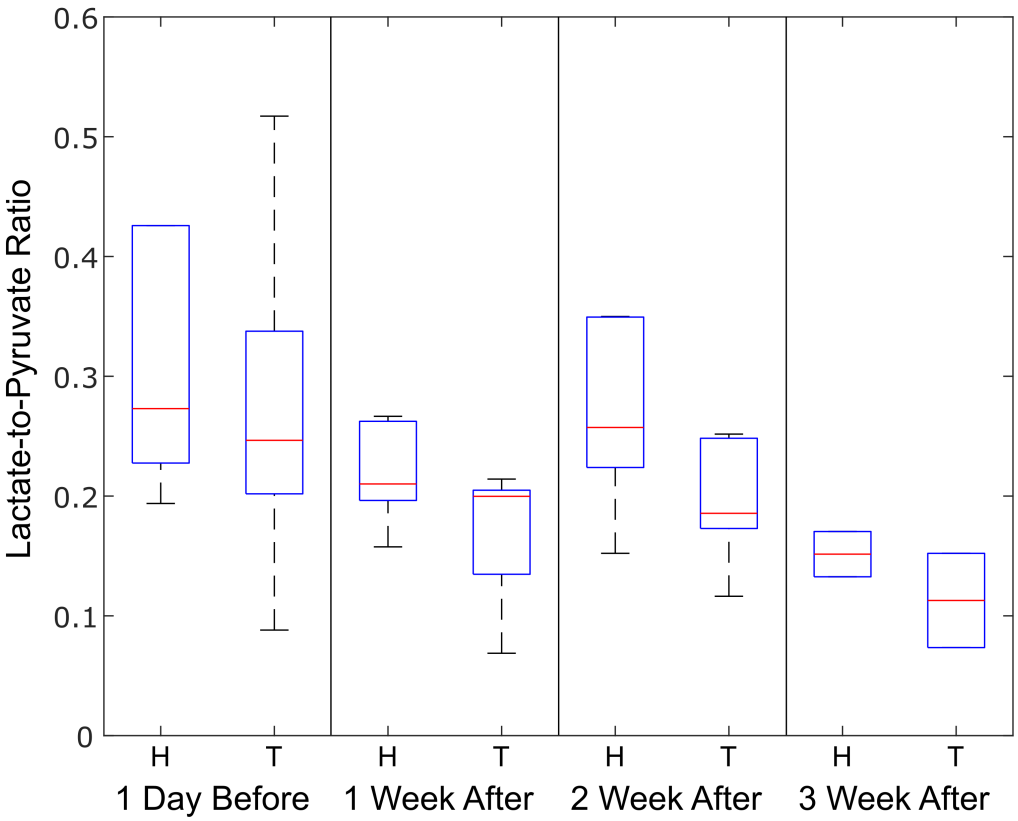


Figure 31: Comparison of the lactate-to-pyruvate ratio changes for six measured rats in response to radiation therapy. The data was acquired one day before the irradiation and, in succession, over the time course of three weeks. Displayed are one voxel in the healthy leg (H) and one within the tumor volume (T). One outlier for the healthy voxel one day before irradiation at $\sim 0.75$ is not displayed.

### 4.2.4. Metabolic Imaging with [1,2-$^{13}$C]Pyruvate

For the first time, volumetric MRSI data of the spectrally-complex [1,2-$^{13}$C]pyruvate was acquired with a spatial resolution in 3D. To this end, the rEPSI acquisition took advantage of the high spatio-spectral resolution, advanced through $T_1$-compensating VFAs as well as ETS [55]. Due to the increased measurement time, only one timepoint could be acquired.

Intensity maps from the up-field peaks of [1-$^{13}$C]pyruvate, [2-$^{13}$C]pyruvate, [1-$^{13}$C]lactate and [1-$^{13}$C]alanine for a transversal, coronal and sagittal slice are shown in Figure 32. In all observed metabolites, the shape of the rat is resembled. While the signal of pyruvate and lactate is spread out over the rat volume, the alanine shows an increased intensity near the heart. Furthermore, it can be noted that the [2-$^{13}$C]pyruvate maps in the coronal slice are shifted to the right in reference to the [1-$^{13}$C]pyruvate maps. This mismapping is also called chemical shift artifact and is discussed in Section 5.2.2.

The spectra of a voxel within the abdomen as well as the right hind leg are shown in Figure 33, where doublets of both [1,2-$^{13}$C]pyruvate peaks can be seen, as well as the doublets for [1-$^{13}$C]lactate, [1-$^{13}$C]pyruvate hydrate and [1-$^{13}$C]alanine. The high spectral quality allows for a clear distinction and quantification of most resonances, only showing an overlap for the upfield resonance of [1-$^{13}$C]pyruvate hydrate and the downfield one of [1-$^{13}$C]lactate.

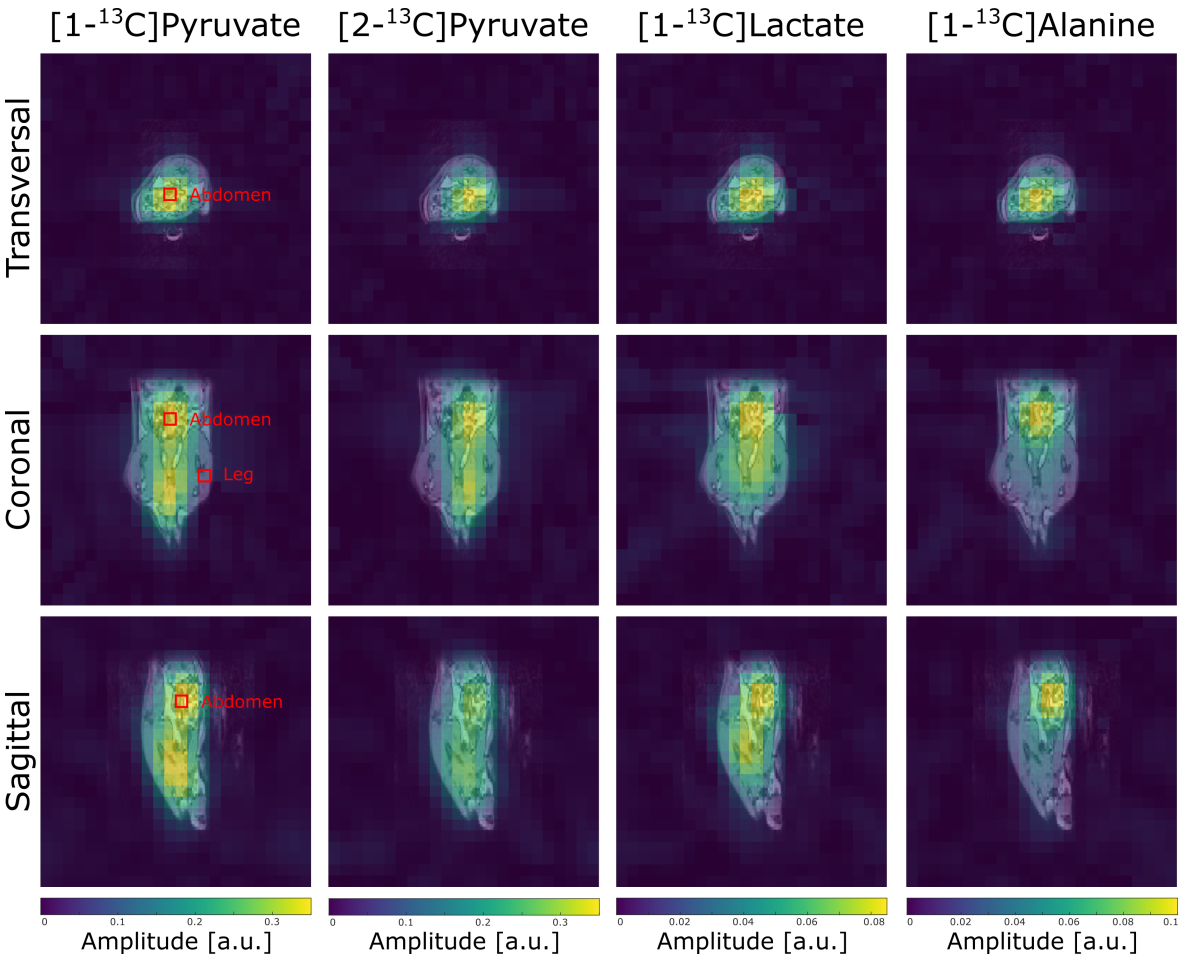


Figure 32: Intensity maps for a hyperpolarized $^{13}$C measurement of a rat using [1,2-$^{13}$C]pyruvate, showing [1-$^{13}$C]pyruvate, [2-$^{13}$C]pyruvate, [1-$^{13}$C]lactate and [1-$^{13}$C]alanine (from left to right) for a slice in transversal, coronal and sagittal (from top to bottom) view. The two red squares indicate the voxel positions within abdomen and the right leg muscle of the spectra shown in Figure 33.

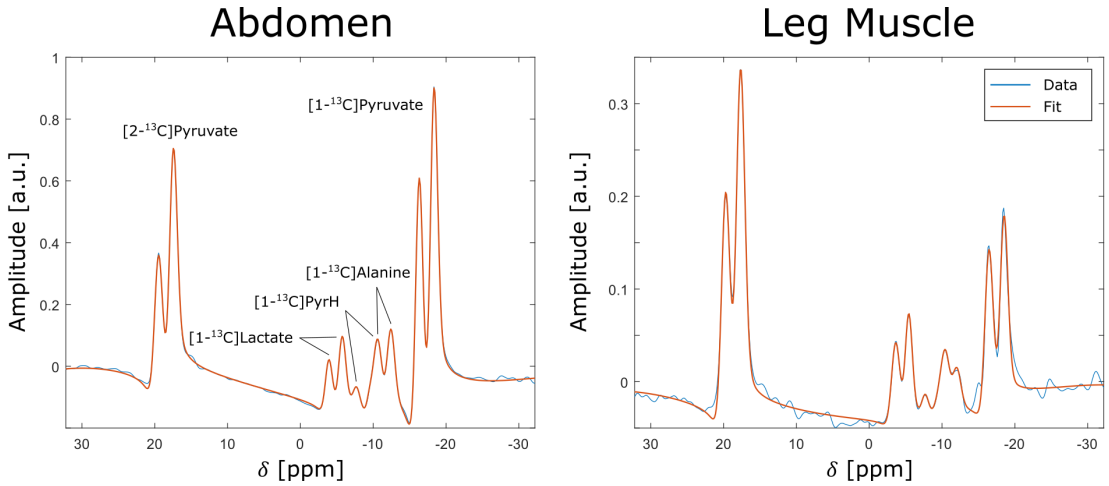


Figure 33: A representative [1,2-$^{13}$C]pyruvate spectrum from the abdominal area of the rat (left) and from a peripheral voxel within the right leg muscle (right).

## 4.3. Application to In Vivo $^{13}$C $B_1^+$ Mapping Using Magnetic Resonance Fingerprinting

As shown in previous sections, hyperpolarized $^{13}$C experiments use dedicated excitation scheme to preserve the non-recoverable hyperpolarized signal or, in the case of the $T_1$-compensation, require an accurate knowledge of the applied FA in general. Hence, $B_1^+$ mapping prior to the HP measurement is highly advantageous to ensure an optimal usage of the available signal.

However, $B_1^+$ mapping for $^{13}$C in vivo is challenging because of an extremely low $^{13}$C SNR, with the highest intensity arising from lipids, mostly from muscle tissue in the neck region. Figure 34 compares the spectrum of an FID measurement with a full volume excitation and 256 averages versus a (50 mm)$^3$ voxel from an rEPSI acquisition with 52 spokes. The spectral resolution was 0.8 Hz for the FID and 6.3 Hz for the rEPSI. In both cases, an FA of 60° was applied.

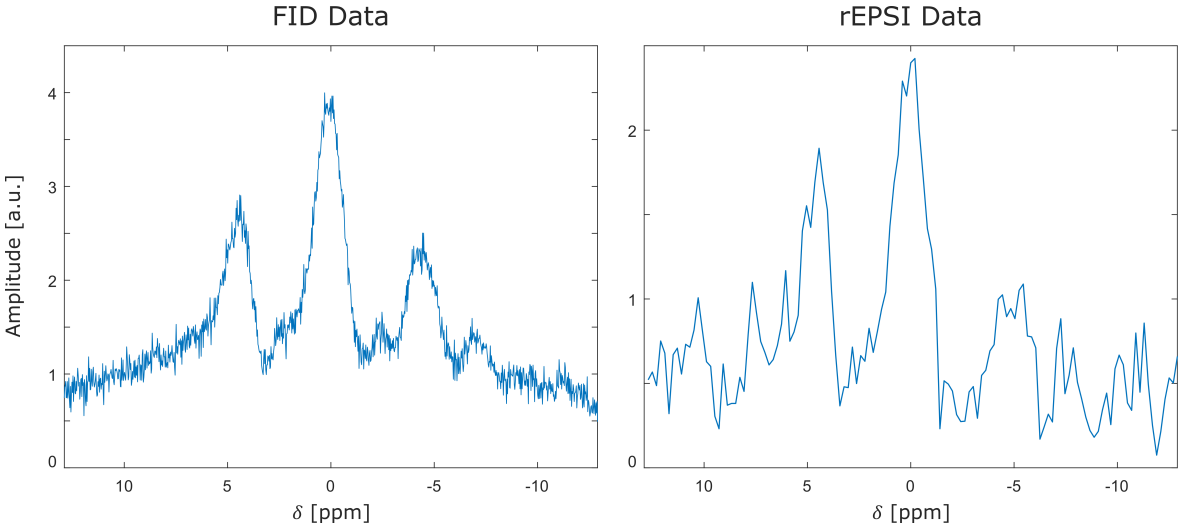


Figure 34: Comparison of the $^{13}$C lipid signal from the human head, once measured with an FID sequence, 256 averages and a full-volume excitation (left) and once with the rEPSI sequence, 52 spokes and a voxel size of (50 mm)$^3$ (right).

The lipid resonances exhibit a very complicated spectral pattern with around twelve resonances within the investigated spectral range of 25.6 ppm [8]. Additionally, and a strong baseline is present, which comes from signals further off-resonant that fold into the acquired spectral BW.

In this work, a novel $B_1^+$ mapping method via a spectral MRF approach was implemented. $B_1^+$ mapping via MRF has proven to be stable against low SNR and undersampling and, moreover, more accurate in low FA regimes than commonly used methods [28]. Ultimately, using the abundant spectral information to facilitate the MRF matching process, this technique could provide a highly robust $B_1^+$ quantification.

### 4.3.1. Proof-of-Concept on $^1$H Data

For a proof-of-concept, the novel $B_1^+$ mapping approach was firstly applied to the $^1$H EG spectra because of the high available SNR. Two different evaluation strategies were compared, one using AMARES fitting results for the matching process, and another that uses the localized spectra directly.

Starting with the AMARES approach, the spectral quality of the acquired data and the corresponding fit can be seen for the lowest applied FA (1°) and the highest one (45°) in the upper part of Figure 35. The high SNR of the $^1$H data allows for a stable fit, even for low FA.

Representatively, the lower part of Figure 35 shows the fitted amplitude of both peaks over the whole VFA pattern, together with the best possible match from the dictionary. Both data and match display a very similar signal evolution over the full VFA scheme, only having a small deviation for the downfield resonance in the high FA regimes.

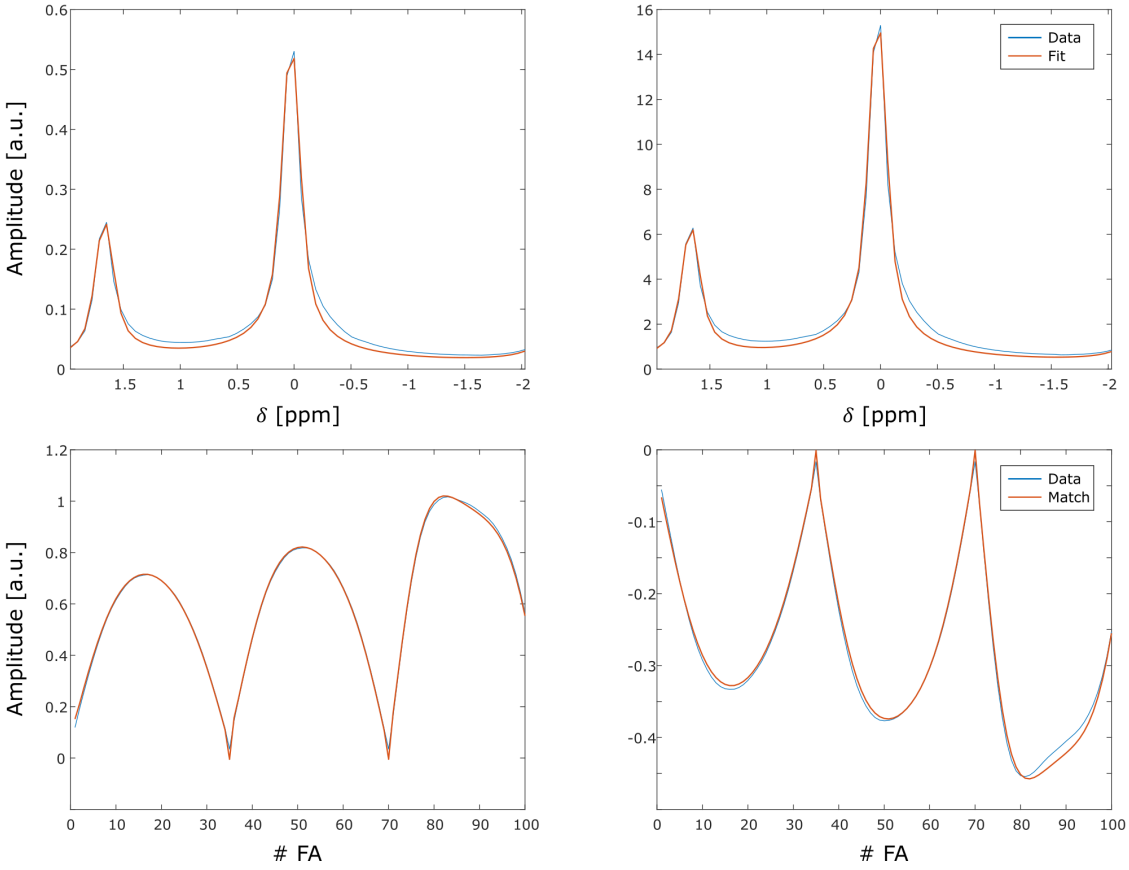


Figure 35: Spectral quality and fit of the $^1$H EG data for the lowest FA of 1° (top left) and the highest FA of 45° (top right). Moreover, the resulting signal of the applied FA pattern for the central peak (bottom left) and the downfield peak (bottom right) is shown with the best match from the AMARES-based MRF.

The resulting estimated $B_1^+$ maps of those fingerprints are shown in Figure 36, where a comparison between the MRF approach conducted on different days, as well as the double-angle (DA) mapping technique as the reference method. The applied mask set all values with a matching accuracy below 33% to zero. All maps show comparable patterns for the estimated actual FAs, especially the two maps from the MRF approach, confirming its reproducibility. However, the DA mapping seems to tend to higher estimated $B_1^+$ values for the center of the coronal slice, as well as lower regions in coronal and sagittal slices, compared to the MRF results.

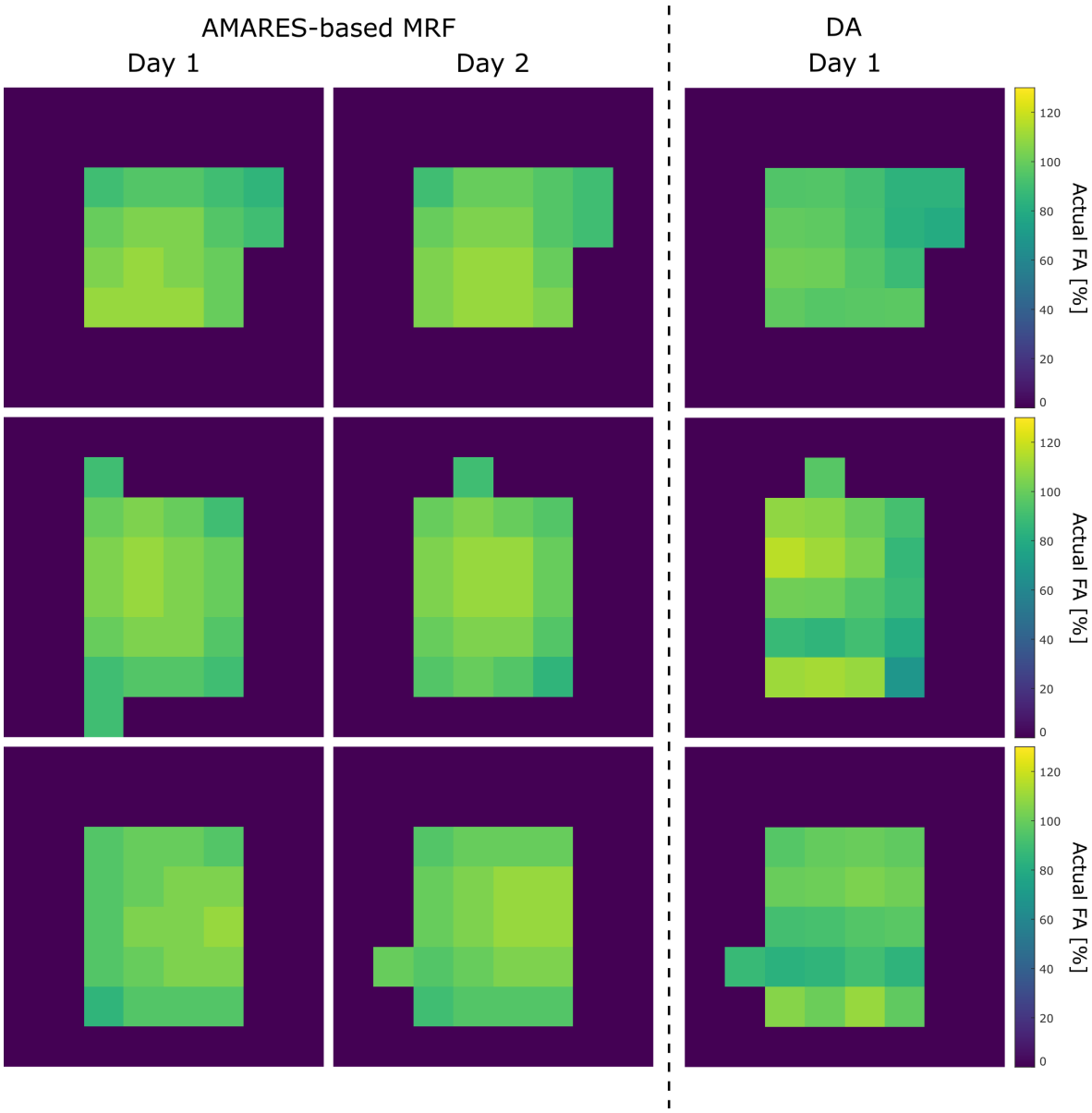


Figure 36: $B_1^+$ maps from the AMARES-based MRF for the $^1$H EG data performed on two different days (left and middle). As a reference, the DA maps are presented (right). For all data, a representative slice is shown in transversal (top), coronal (center) and sagittal (bottom) orientation.

The other parameters of the matching process yielded reasonable estimations as well. The $M_0$ distribution displays a high concentration in the middle of the phantom with a clear cut-off at the boundaries. All other matched values, i.e. $T_1$, $T_2$ and $\Delta B_0$, are shown for the coronal slice of the first MRF dataset. Here, homogeneous maps were produced with the estimated relaxation times being $T_1 = 0.5$ s and $T_2 = 0.08$ s, while off-center shifts due to $B_0$ inhomogeneities reached the boundary of $-4$ Hz in all voxels.

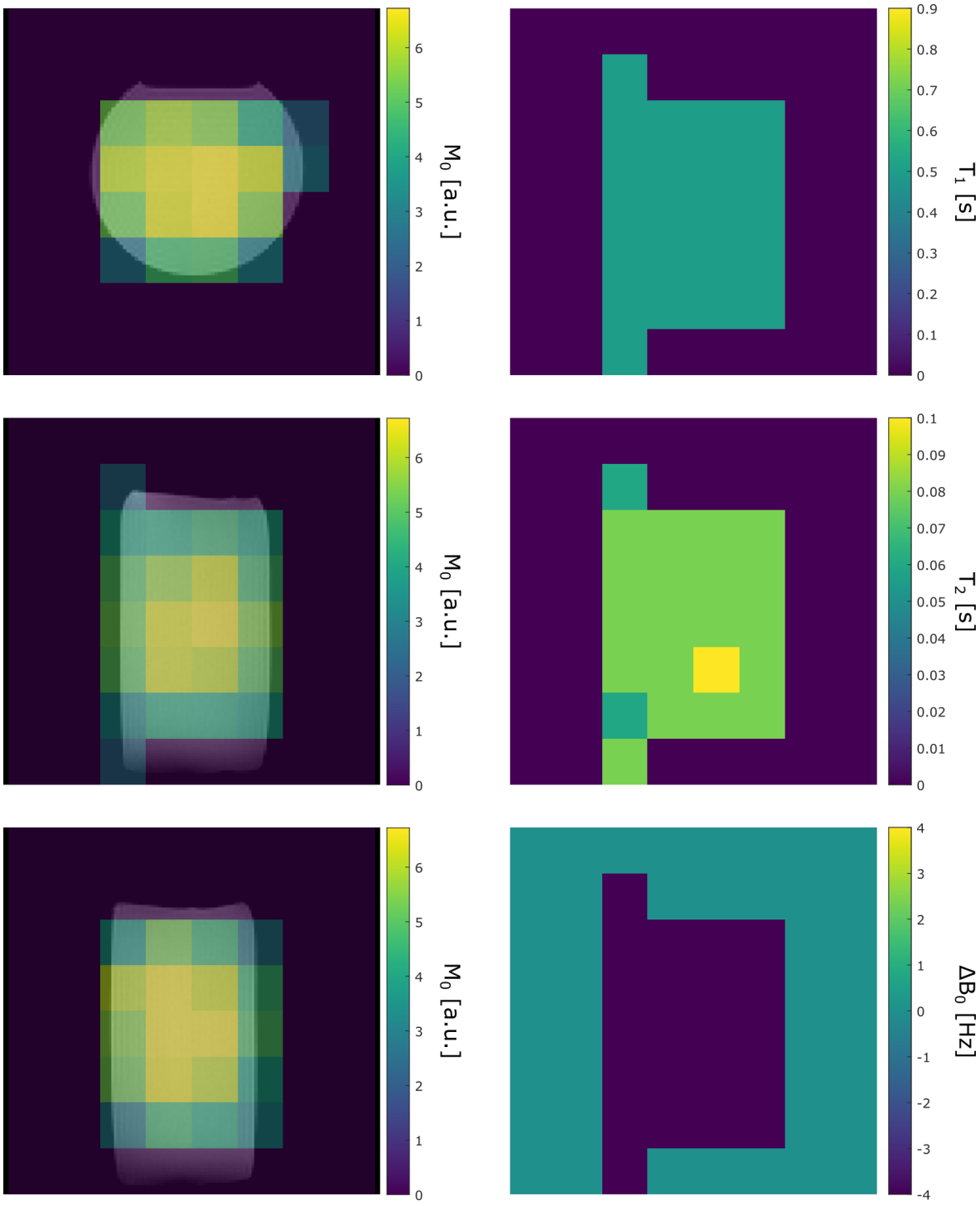


Figure 37: $M_0$ distributions from the AMARES-based MRF for the $^1$H EG data, overlaid with an anatomical image for reference. Shown are a representative transversal (top left), coronal (center left) and sagittal (bottom left) slice. Additionally, $T_1$ (top right), $T_2$ (center right) and $\Delta B_0$ (bottom right) are presented for the coronal slice.

Next, the same $^1$H data of EG was matched with the full-spectral approach. Figure 38, therefore, shows not only two fingerprints, like in Figure 35, but 64, one for each acquired spectral point. For visualization, acquired data and the best-matching fingerprint are shown separately.

An overlay of the match can be displayed for the spectral data at the highest FA, as well as the center of the spectrum at 0 ppm. The matched spectral data shows a good overlap, with only a small deviation around the downfield resonance, seen in Figure 38, bottom left. These mismatched regions in the spectral domain produced amplitude differences in the estimated FA pattern. Even though the FA pattern is resembled well in its shape, some spectral points deviate fairly in amplitude.

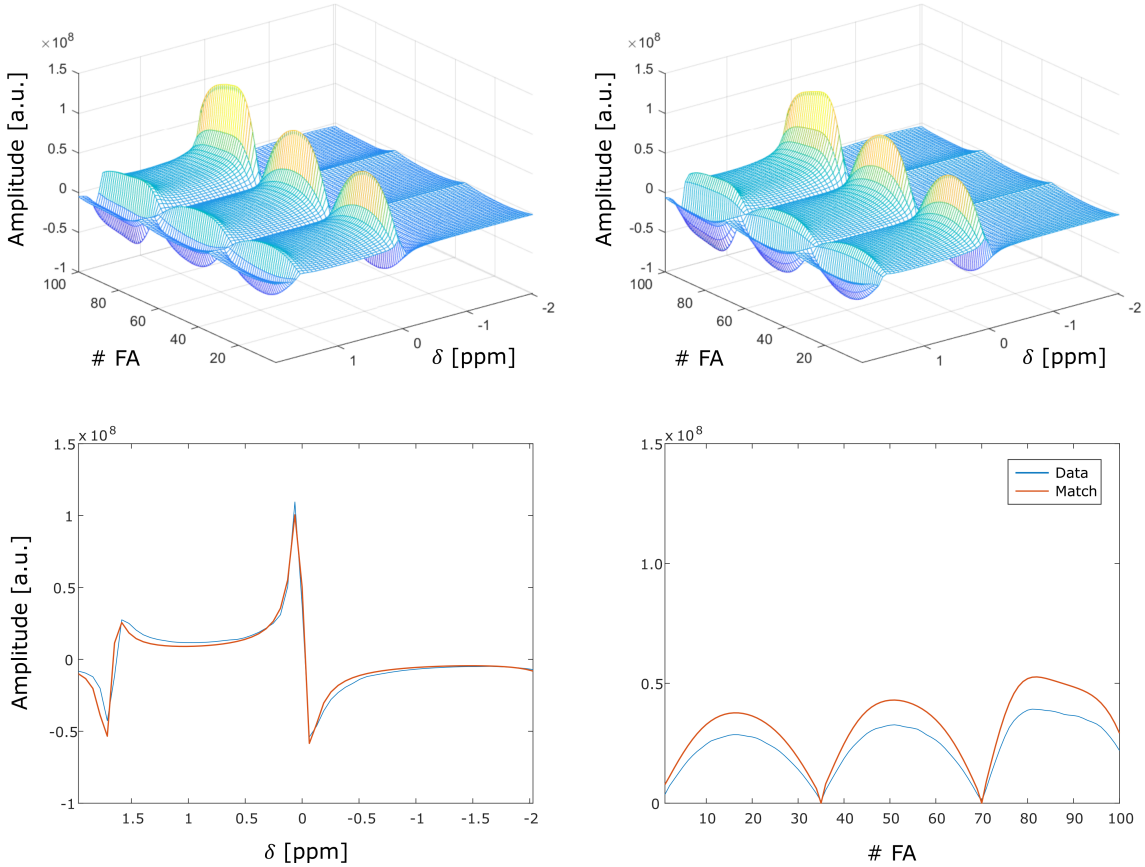


Figure 38: $^1$H EG spectra over the whole FA pattern (top left) in comparison to the best match from the full-spectral MRF (top left). Moreover, the matched spectrum for the highest FA of 45° (bottom left) and the matched FA pattern at 0 ppm (bottom right) are shown.

The resulting $^1$H $B_1^+$ maps in Figure 39 show very similar results for the repeated measurements in comparison to the DA mapping, and also agree with the AMARES-based approach in Figure 35.

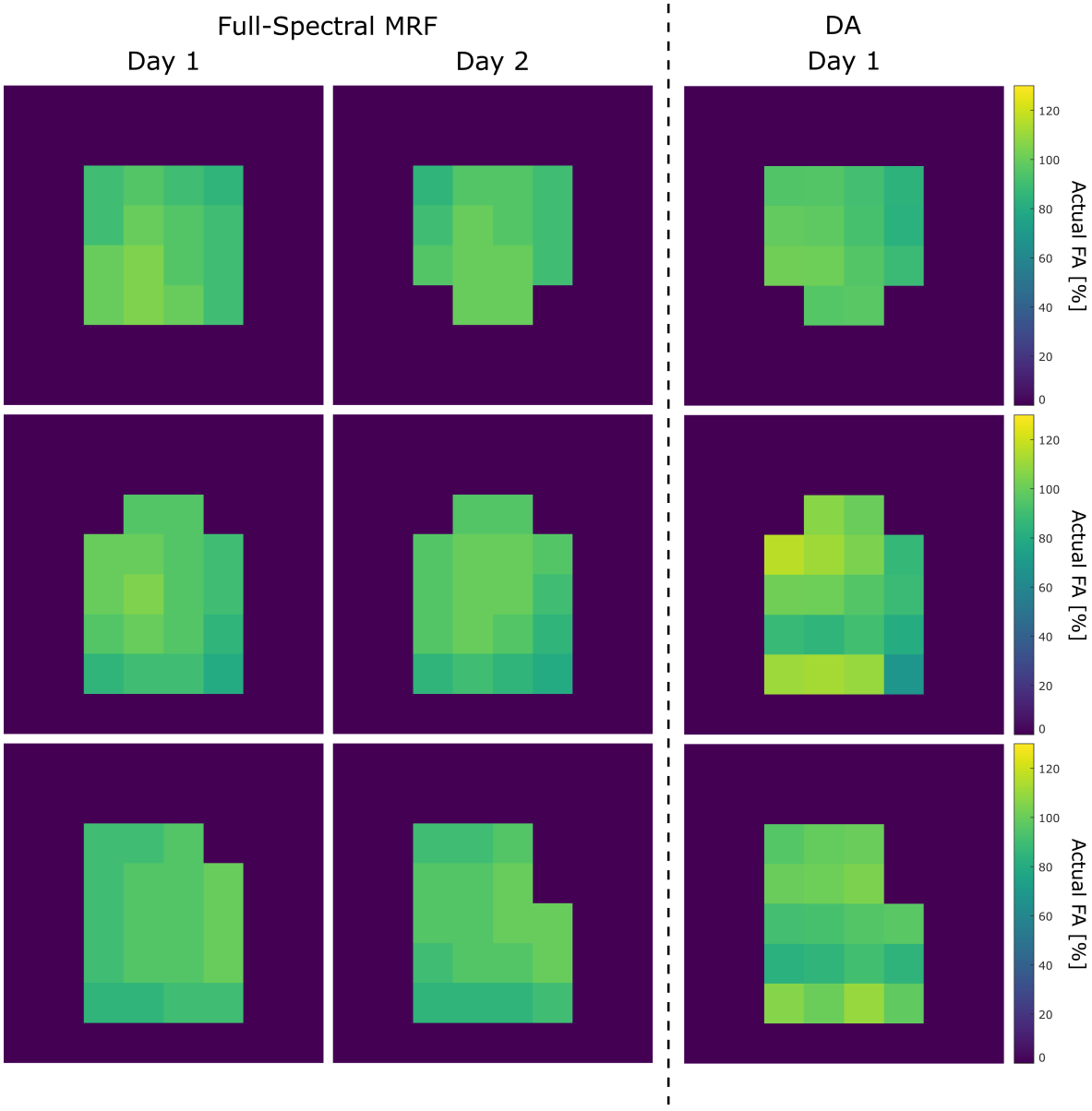


Figure 39: $B_1^+$ maps from the full-spectral MRF for the $^1$H EG data performed on two different days (left and middle). As a reference the DA maps are presented (right). For all data, a representative slice is shown in transversal (top), coronal (center) and sagittal (bottom) orientation.

The $M_0$ distribution agrees very well with the phantom's shape, as shown in Figure 40. The estimated $T_1$ also agrees with the AMARES-based approach, estimating a value of 0.5 s. For $T_2$, a lower value of $\sim 0.06$ s was estimated in the center of the phantom. Also, the spectral shift due to $\Delta B_0$ is changing from $+4$ Hz to $-4$ Hz, going from left to right in the coronal slice.

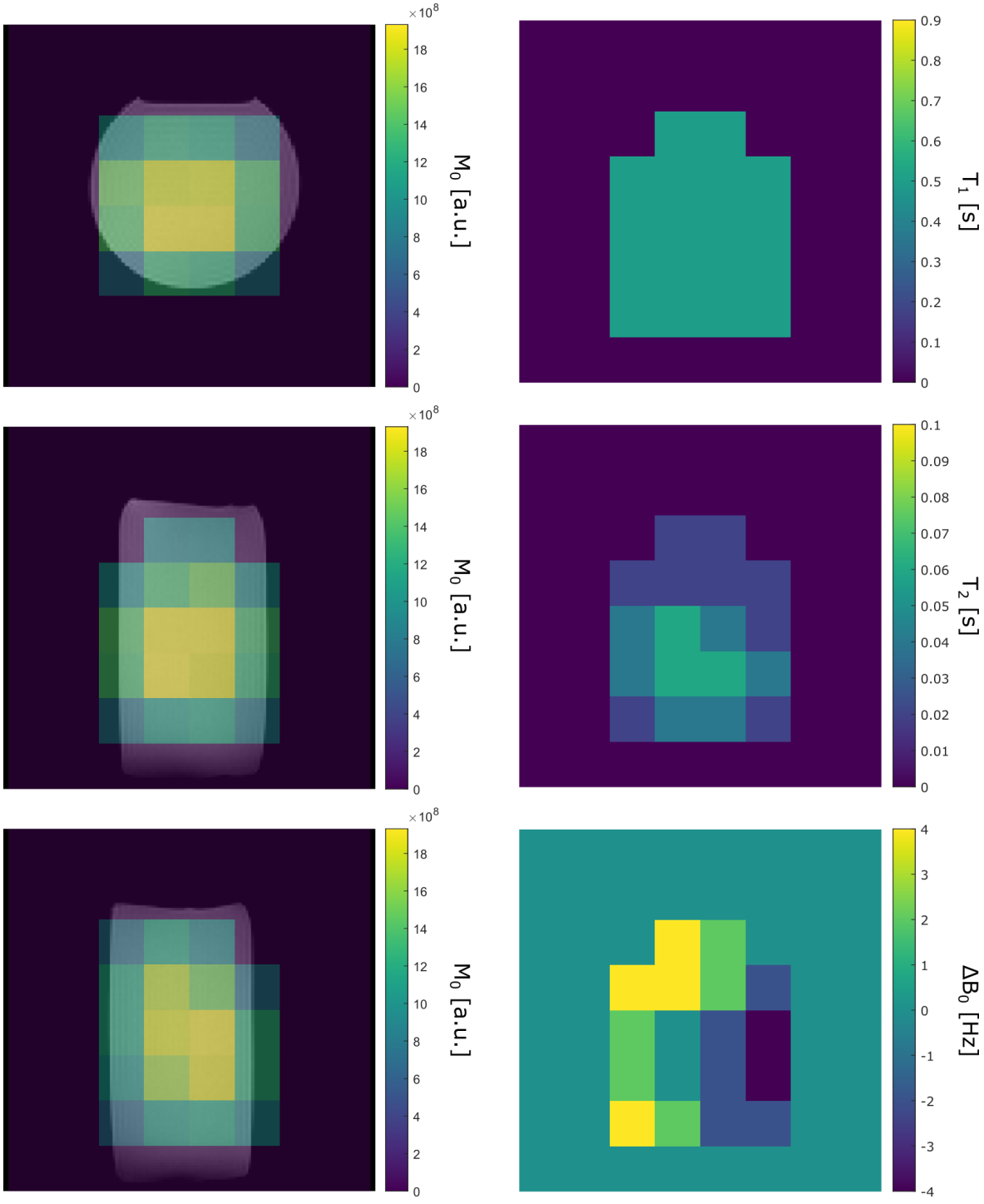


Figure 40: $M_0$ distributions from the full-spectral MRF for the $^1$H EG data, overlaid with an anatomical image for reference. Shown are a representative transversal (top left), coronal (center left) and sagittal (bottom left) slice. Additionally, $T_1$ (top right), $T_2$ (center right) and $\Delta B_0$ (bottom right) are presented for the coronal slice.

Altogether, these results on high-SNR $^{1}$H data demonstrate the general feasibility of the spectral MRF approach to estimate $B_1^+$ fields. While the AMARES-based and the full-spectral matching approach yield similar estimated $B_1^+$ values compared to a conventional DA estimation, the MRF evaluation enables the estimation of additional parameters, which differ slightly between both approaches.

### 4.3.2. $^{13}$C $B_1^+$ MRF In Vitro

With the feasibility of the approach now demonstrated, the spectral $B_1^+$ MRF is applied to $^{13}$C data of lower SNR. First, the AMARES-based approach is applied to the $^{13}$C phantom data. In Figure 41, the lower SNR compared to the $^{1}$H is visible, especially, when applying a small FA of 1°. Nevertheless, the fingerprints resemble the FA pattern very well, allowing for a stable matching of the data for all three resonances.

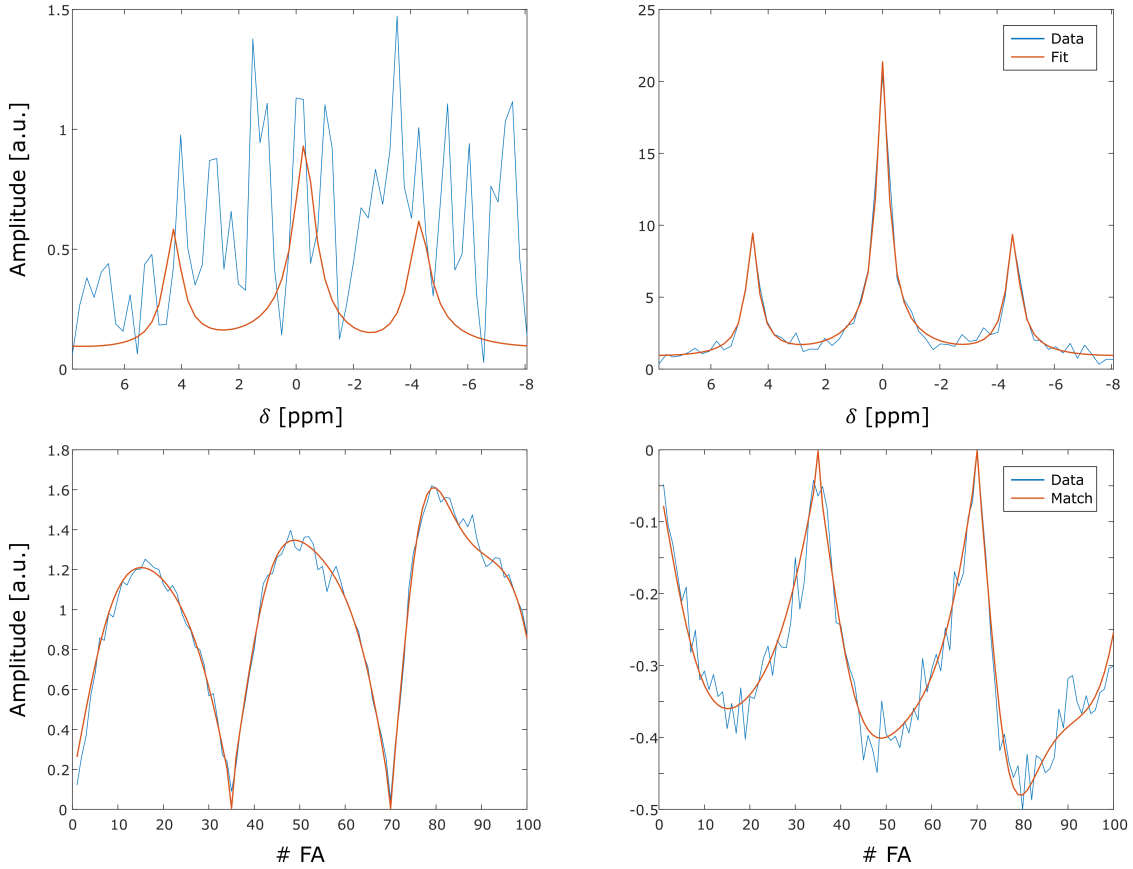


Figure 41: Spectral quality and fit of the $^{13}$C EG data for the lowest FA of 1° (top left) and the highest FA of 45° (top right). Moreover, the resulting signal of the applied FA pattern for the central peak (bottom left) and the downfield peak (bottom right) is shown with the best match from the AMARES-based MRF.

The AMARES-based $B_1^+$ maps from Figure 42 show an overall agreement of the actual FA distributions between different days, as well as the DA mapping. However, the MRF maps show larger fluctuation than the DA maps.

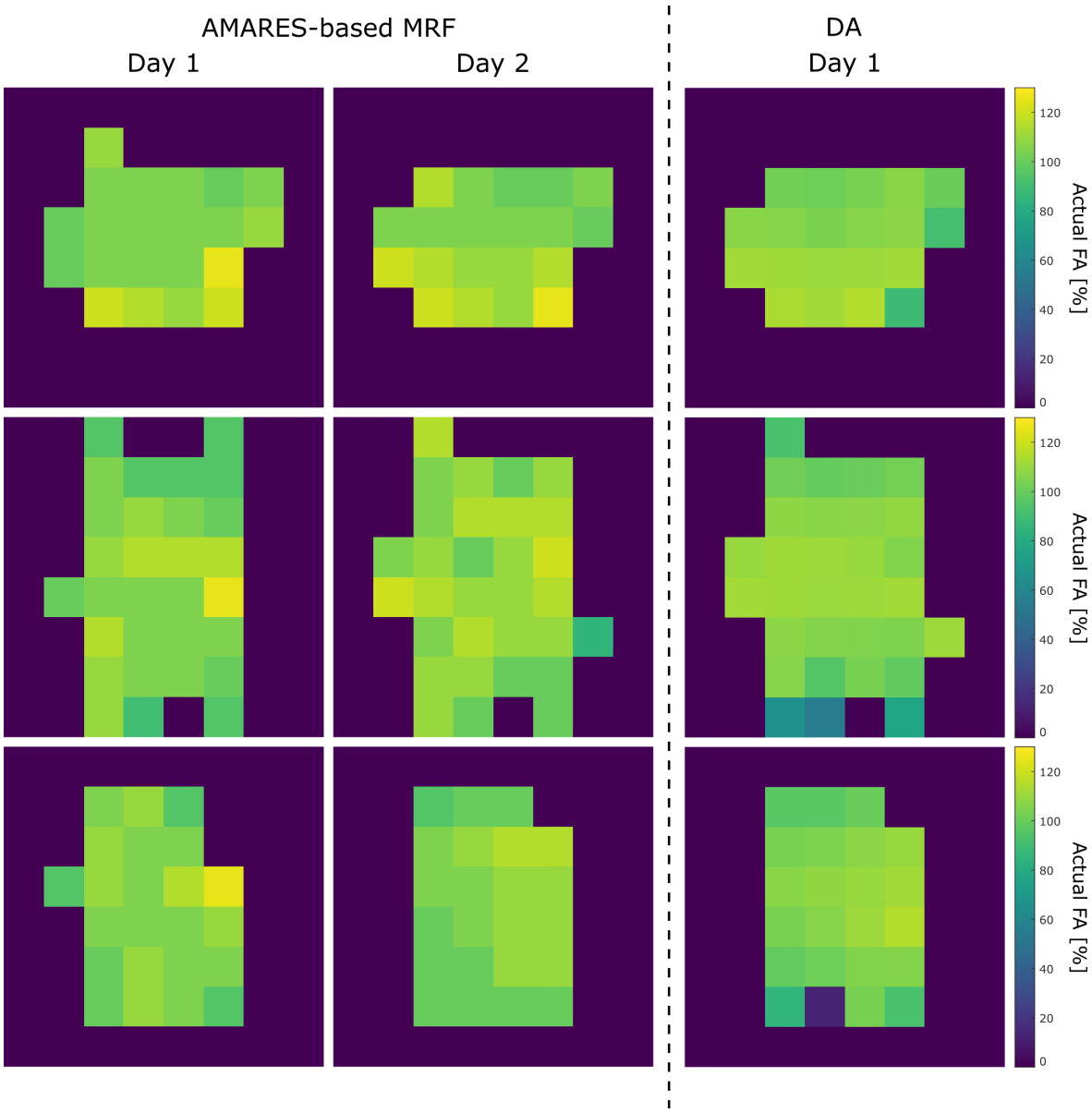


Figure 42: $B_1^+$ maps from the AMARES-based MRF for the $^{13}$C EG data performed on two different days (left and middle). As a reference the DA maps are presented (right). For all data, a representative slice is shown in transversal (top), coronal (middle) and sagittal (bottom) orientation.

Also all other estimated parameters are consistent within repeated measurements. For the $M_0$ distribution, the phantom shape is resembled well, however the shown maps are much more inhomogeneous compared to the $^1$H data, showing intensity drops within the phantom's volume. For the $T_1$ time, the maps roughly converge on 0.8 s and for the $T_2$ time on approximately 0.06 s. The $\Delta B_0$ values again reached the simulation boundary of $-4$ Hz.

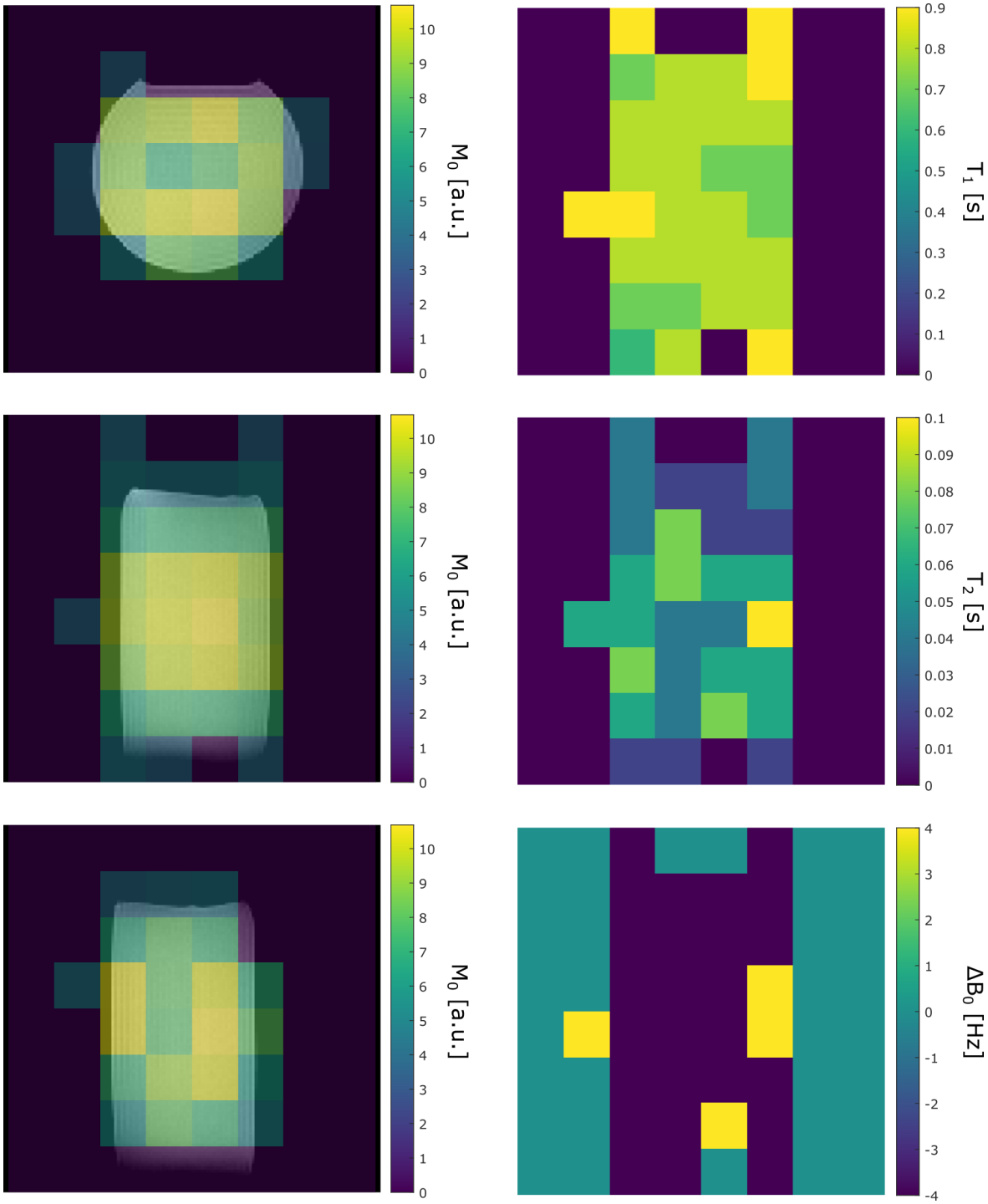


Figure 43: $M_0$ distributions from the AMARES-based MRF for the $^{13}$C EG data, overlaid with an anatomical image for reference. Shown are a representative transversal (top left), coronal (center left) and sagittal (bottom left) slice. Additionally, $T_1$ (top right), $T_2$ (center right) and $\Delta B_0$ (bottom right) are presented for the coronal slice.

Also for the full spectral approach, the matching was successful for the lower SNR $^{13}$C EG data, as shown in Figure 44. The three resonances are matched accurately with correct phases, resulting in only minor amplitude differences in the matching of the FA pattern.

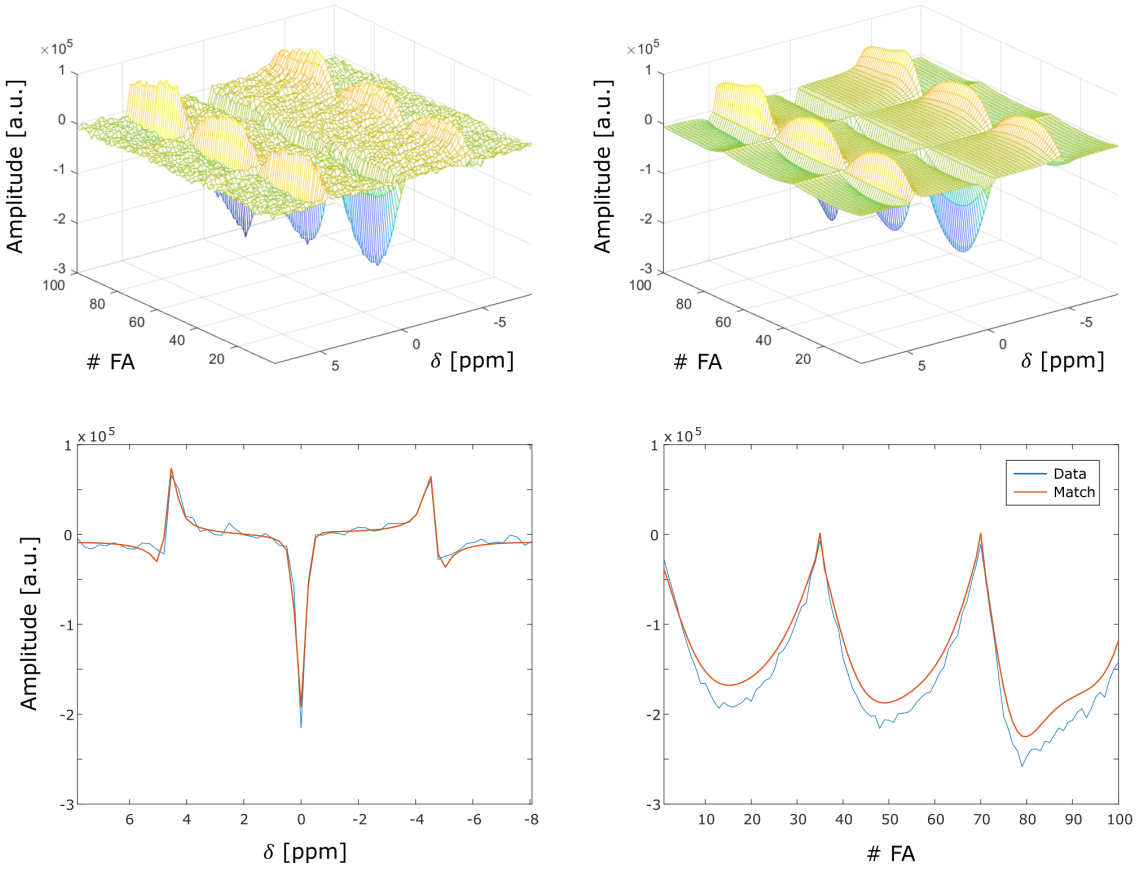


Figure 44: $^{13}$C EG spectra over the whole FA pattern (top left) in comparison to the best match from the full-spectral MRF (top right). Moreover, the matched spectrum for the highest FA of 45° (bottom left) and the matched FA pattern at 0 ppm (bottom right) are shown.

Just like for the AMARES-based approach, the $B_1^+$ maps are consistent for different days and agree with the DA mapping, as seen in Figure 45. Again, the MRF method provides less smooth maps, but appear to fluctuate less than the AMARES-based estimates.

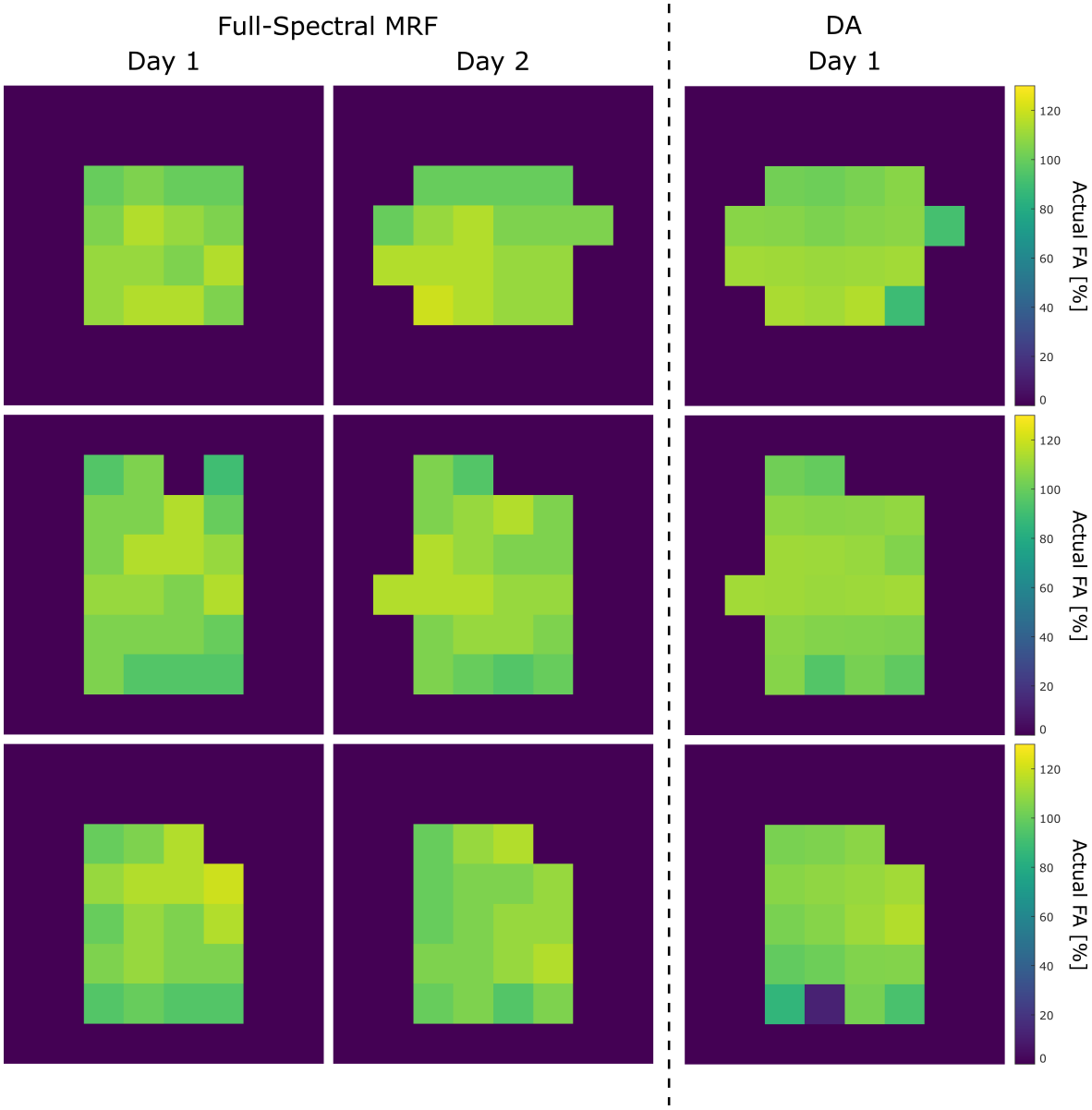


Figure 45: $B_1^+$ maps from the full-spectral MRF for the $^{13}$C EG data performed on two different days (left and middle). As a reference the DA maps are presented (right). For all data, a representative slice is shown in transversal (top), coronal (center) and sagittal (bottom) orientation.

The $M_0$ distribution of Figure 46 are slightly more accurate than for the AMARES-based approach. The estimated $T_1$ time is 0.8 s and the $T_2$ time in the center is 0.06 s. The $B_0$ inhomogeneities shown for the coronal slice range from +2 Hz in the bottom to 0 Hz in the middle of the phantom, and finally again up to +4 Hz in the top.

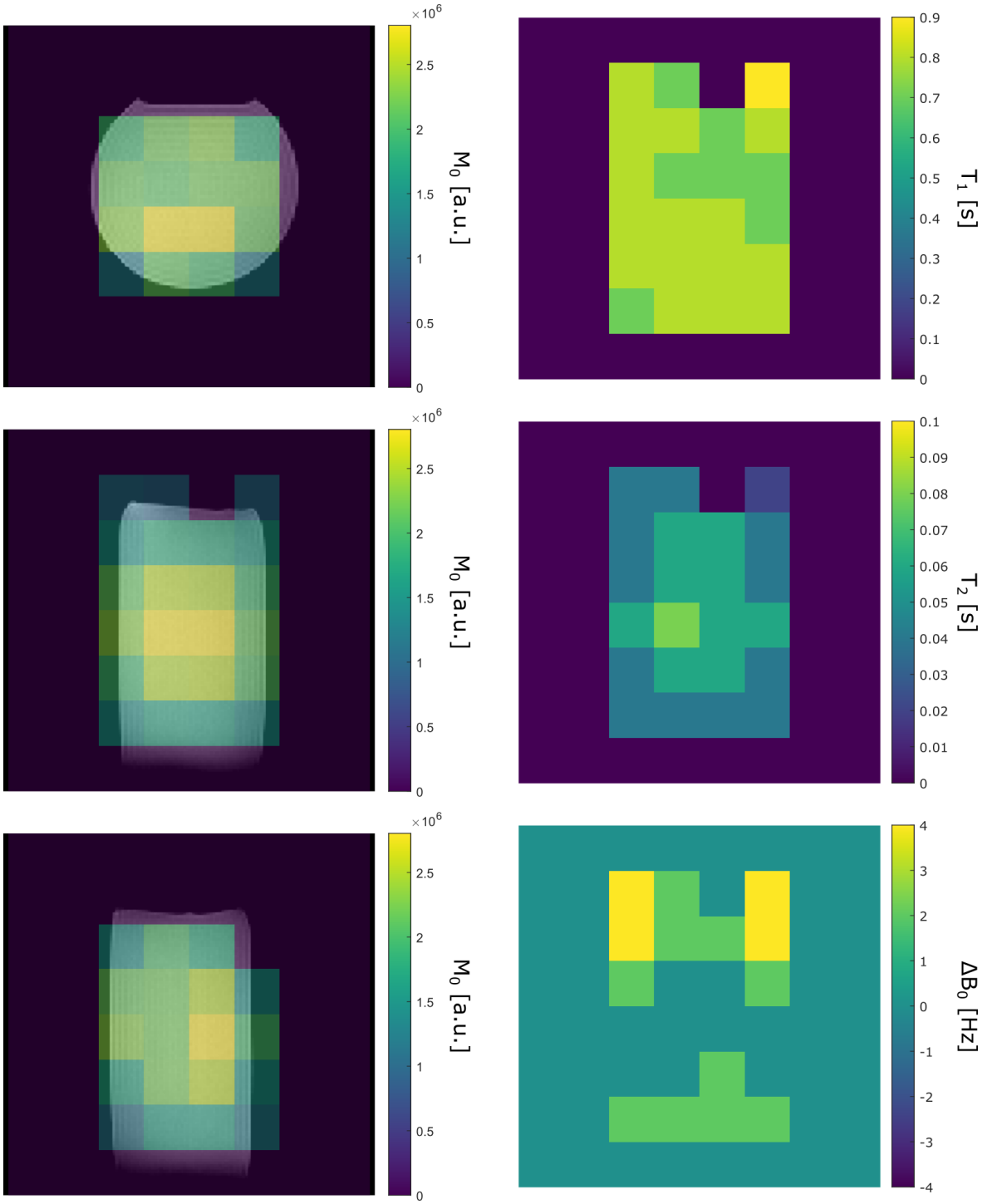


Figure 46: $M_0$ distributions from the full-spectral MRF for the $^{13}$C EG data, overlaid with an anatomical image for reference. Shown are a representative transversal (top left), coronal (center left) and sagittal (bottom left) slice. Additionally, $T_1$ (top right), $T_2$ (center right) and $\Delta B_0$ (bottom right) are presented for the coronal slice.

### 4.3.3. Comparison of the Presented MRF $B_1^+$ Mapping Approaches

In order to identify a suitable approach for the very low SNR expected in vivo, all $B_1^+$ maps are compared with each other. The estimated actual FAs of the eight most center voxels were taken to calculate the mean deviation to the applied nominal FA value. The results are listed in Table 13, where the DA mapping is compared to the two individual measurements of both MRF quantification approaches for $^1$H as well as $^{13}$C.

| Nucleus | DA [%] | AMARES [%] | | Full-Spectral [%] | |
|---|---|---|---|---|---|
| $^1$H | $(+1.5 \pm 6.4)$ | $(+7.5 \pm 2.7)$ | $(+5.6 \pm 3.2)$ | $(-1.3 \pm 2.3)$ | $(-1.9 \pm 3.7)$ |
| $^{13}$C | $(+8.8 \pm 2.4)$ | $(+6.3 \pm 3.5)$ | $(+8.1 \pm 4.6)$ | $(+9.4 \pm 4.2)$ | $(+12.5 \pm 3.8)$ |

Table 13: Comparison of the estimated actual FA as deviation of the nominal value in percentage. Presented are the $^1$H and $^{13}$C data for all three applied $B_1^+$ mapping methods, i.e. DA, AMARES-based MRF and full-spectral MRF. For the two MRF evaluations, two datasets are presented, in order to analyze their consistency. The eight most center voxels have been used for evaluation.

Taking the DA results as a reference, none of the results of the two MRF methods deviate significantly. Looking at the $^1$H data, the AMARES-based approach underestimates the actual FA by about 3%, while the full-spectral method overestimates by approximately 5%. For the $^{13}$C data vice versa, the AMARES-based MRF overestimates and the full-spectral MRF underestimates the reference values by about 2% each. The error margins for all values are revealing no particular advantage of either used technique. Moreover, both approaches yield very similar results when repeated on different days, confirming their reproducibility.

Next, the robustness of both presented MRF quantification approaches against a decreasing SNR is investigated by reconstructing the $^1$H data with multiple gradually increasing noise levels. For each new evaluation, the difference between the results of the noisy data and the ground truth, i.e. the initially acquired high-SNR $^1$H data, was calculated. Figure 47 shows this deviation in dependency on the SNR level in percentage.

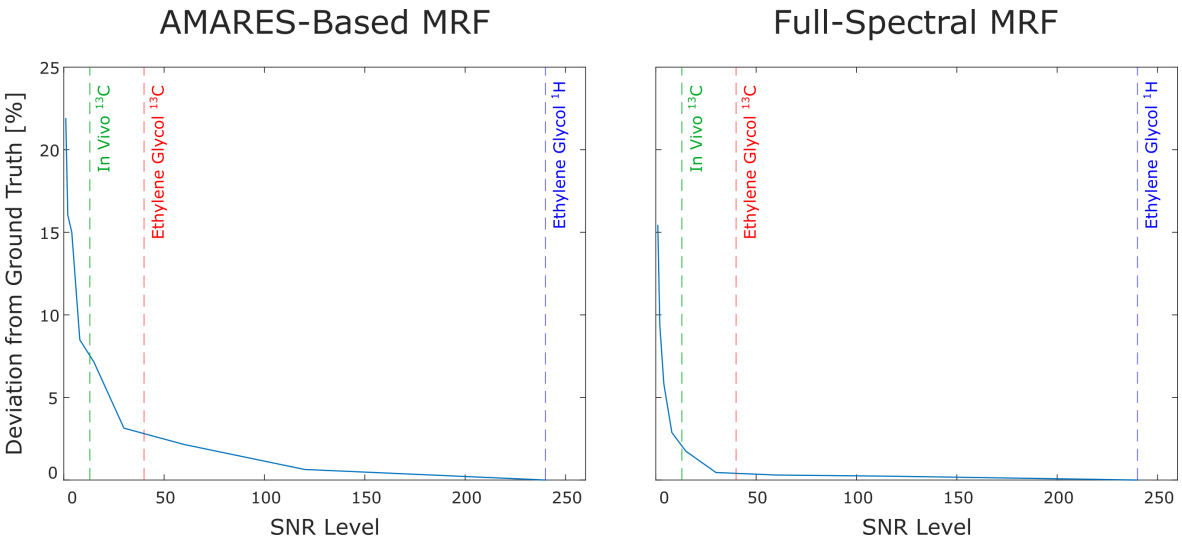


Figure 47: Deviation of $^{1}$H $B_1^+$ maps of the AMARES-based (left) and full-spectral MRF (right) in dependency on the SNR. The ground truth, i.e. the $^{1}$H data without added noise, is marked with the blue dashed line. The green and red dashed line indicate the SNR levels for the $^{13}$C in vivo and $^{13}$C EG data, respectively.

For the AMARES-based method, a noticeable increase of the deviation in estimated $B_1^+$ below an SNR of 100 can be seen, compared to the full-spectral approach. With a $^{13}$C SNR of EG of $\sim 40$, the average deviation in $B_1^+$ maps is $\sim 3\%$ and for in vivo data with an SNR of $\sim 10$ approximately $\sim 8\%$.
In contrast, the full-spectral method is more robust at lower SNR regimes, as the estimated $B_1^+$ only deviates for $\sim 1\%$ for the EG $^{13}$C data and only $\sim 2\%$ for the in vivo case.

Lastly, the advantages of a spectral acquisition for the presented MRF quantification are investigated and a potential threshold for the necessary spectral detail determined. To this end, a final analysis explores the influence of the number of acquired echoes for the full-spectral approach using the high SNR $^{1}$H data. Figure 48 displays the deviation from the ground truth, i.e. in this case 64 as the of the highest number of acquired echoes, as this data showed a high consistency to the DA technique.

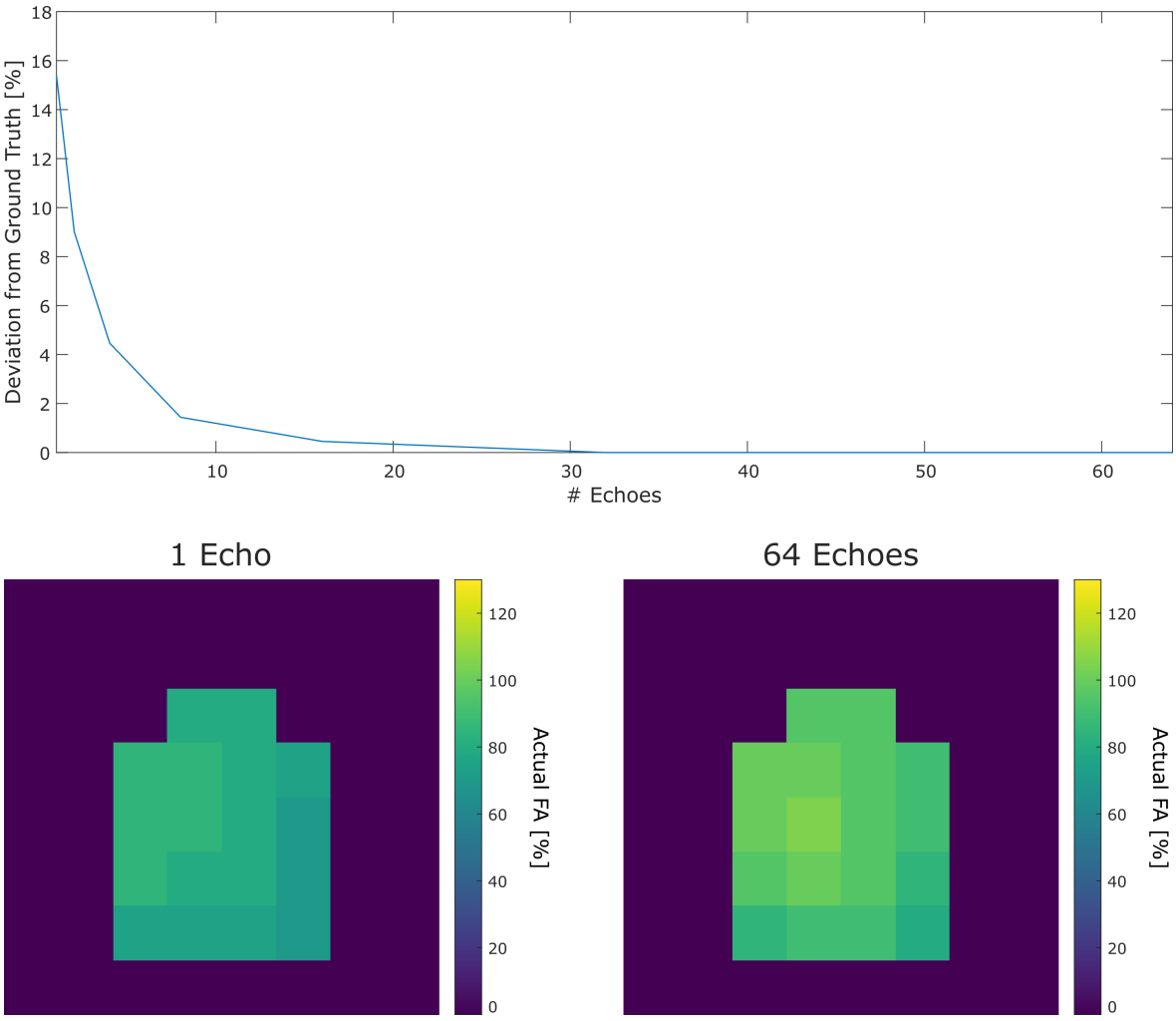


Figure 48: Deviation of $^1$H $B_1^+$ maps of the full-spectral MRF in dependency on the number of acquired echoes. The acquisition of 64 echoes served as ground truth. Additionally, representative $B_1^+$ maps from the reconstructions using 1 and 64 echoes are shown.

Below an echo number of 8, corresponding to a spectral resolution of $\sim$ 60 Hz, a strong increase of this deviation can be seen, also noticeable in the shown example maps. The data using only one echo, i.e. no spectral information, shows a strong underestimation of $\sim$ 16% for the whole $B_1^+$ map compared to the full use of all 64 echoes.

In summary, this confirmed the value of an acquisition of spatially and spectrally resolved data via rEPSI, as the full-spectral matching approach shows a high potential to deal with the low SNR in vivo, through exploiting the abundant spectral information at a spectral resolution of $\sim$ 60 Hz or higher.

### 4.3.4. In Vivo $^{13}$C $B_1^+$ Mapping

Finally, both $^{13}$C MRF $B_1^+$ mapping approaches were applied in vivo, in a healthy volunteer. The resulting actual FA maps are shown in Figure 49. For both methods, only a matching in the back of the head was possible. All other regions do not show reliable results.

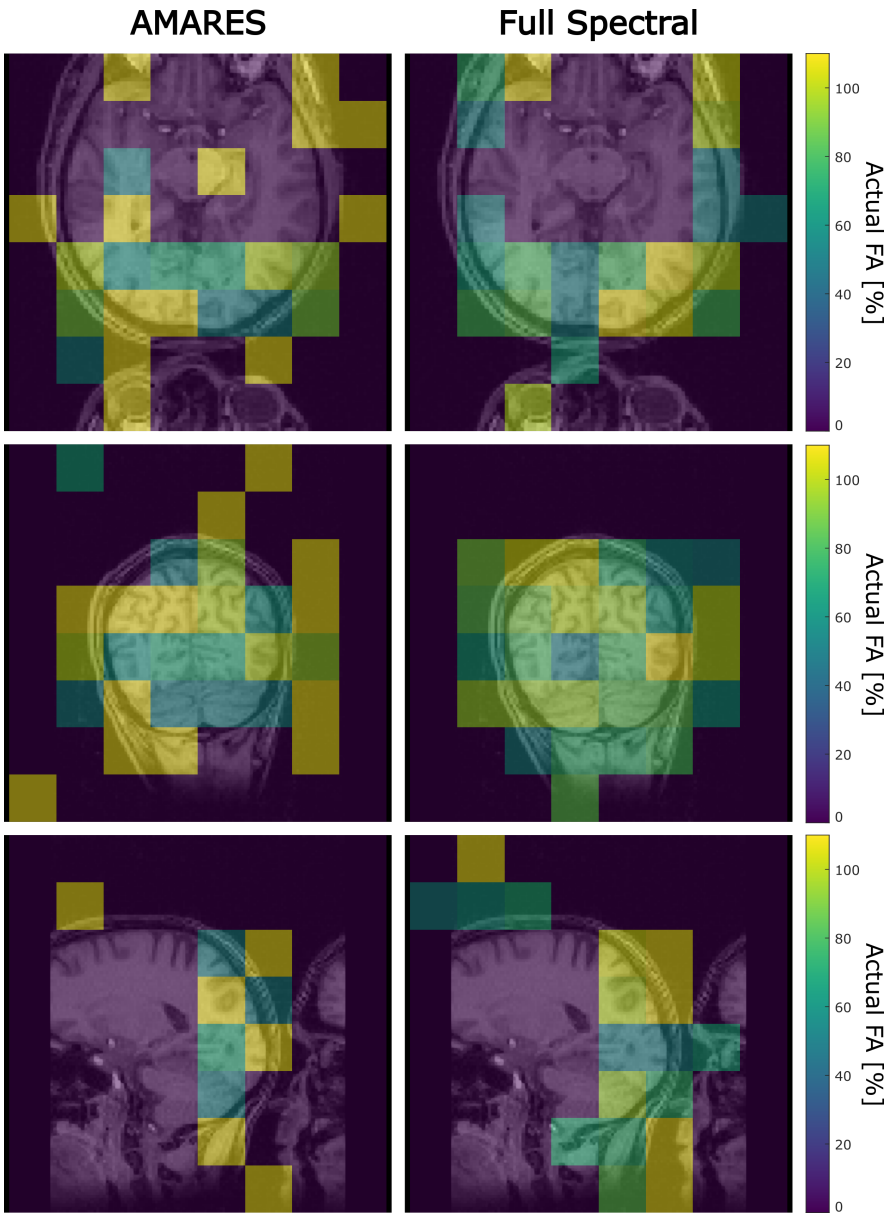


Figure 49: $B_1^+$ maps from the AMARES-based (left) and the full-spectral MRF (right) for the $^{13}$C in vivo data. For all data, a representative slice is shown in transversal (top), coronal (center) and sagittal (bottom) orientation and overlaid with an anatomical image.

The spectral quality of the $^{13}$C in vivo data is very low, as seen in Figure 50, where spectra for all applied FA show an extremely small SNR. This made robust fitting almost impossible, and therefore, resulted in very high fluctuations in the final matched FA patterns. The full spectral approach directly uses the acquired data without a fitting step, resulting in a slightly more recognizable FA pattern. However, due to the extremely low SNR, the spectral match cannot be verified visually.

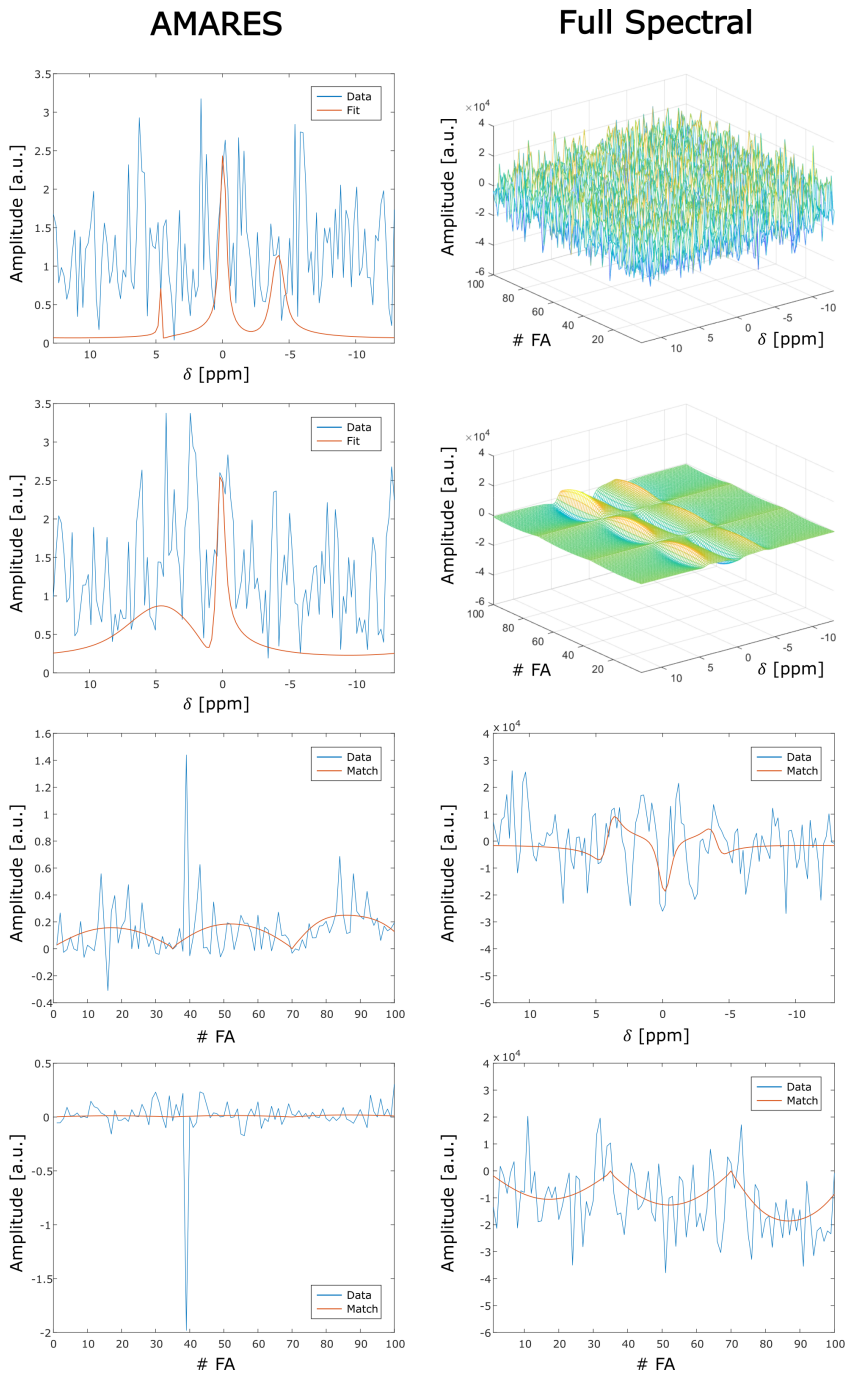


Figure 50: $^{13}$C in vivo spectral data of the AMARES-based (left) and full-spectral MRF (right). For the AMARES-based approach, spectrum and fit for the lowest FA of 1° (1st row) and the highest FA of 45° (2nd row) are presented. Moreover, the resulting signal of the applied FA pattern for the central peak (3rd row) and the downfield peak (4th row) is shown with the best match from the AMARES-based MRF. For the full-spectral approach, spectra over the whole FA pattern are presented (1st row) in comparison to the best match from the full-spectral MRF (2nd row). Moreover, the matched spectrum for the highest FA of 45° (3rd row) and the matched FA pattern at 0 ppm (4th row) are shown.

The other matched parameters are also more homogeneous for the full spectral approach, which consistently estimates $T_1 = 0.3$ s and $T_2 = 0.014$ s as the relaxation times and +6 Hz for $\Delta B_0$ in the middle of the shown coronal slice, while this value drops down to −2 Hz at the outer regions. In general, the fluctuation of parameters indicates that the matching process is not robust enough at the available SNR level.

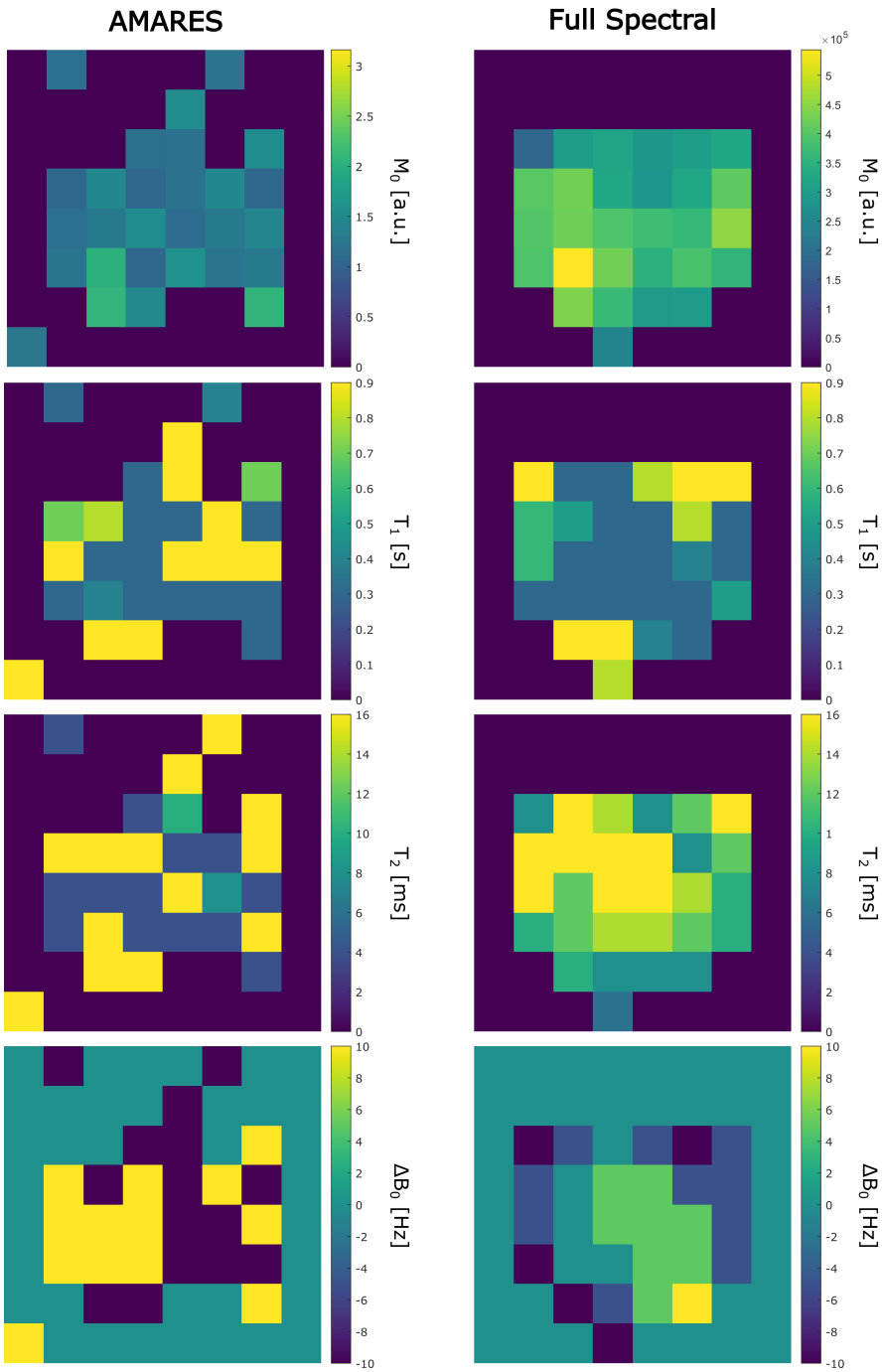


Figure 51: Representative coronal slice of the additional fingerprinting parameters from the AMARES-based (left) and full-spectral MRF (right) for the in vivo $^{13}$C data. The shown parameters are $M_0$ (1st row), $T_1$ (2nd row), $T_2$ (3rd row) and $\Delta B_0$ (4th row).

For the full spectral approach, the dataset was denoised using a low-rank estimation (see Section 3.3.6) and matched again, producing very similar $B_1^+$ maps, as shown in Figure 52. For the spectral quality, shown in Figure 53, the denoising allowed for more recognizable spectral information and, ultimately, also less noisy fingerprints.

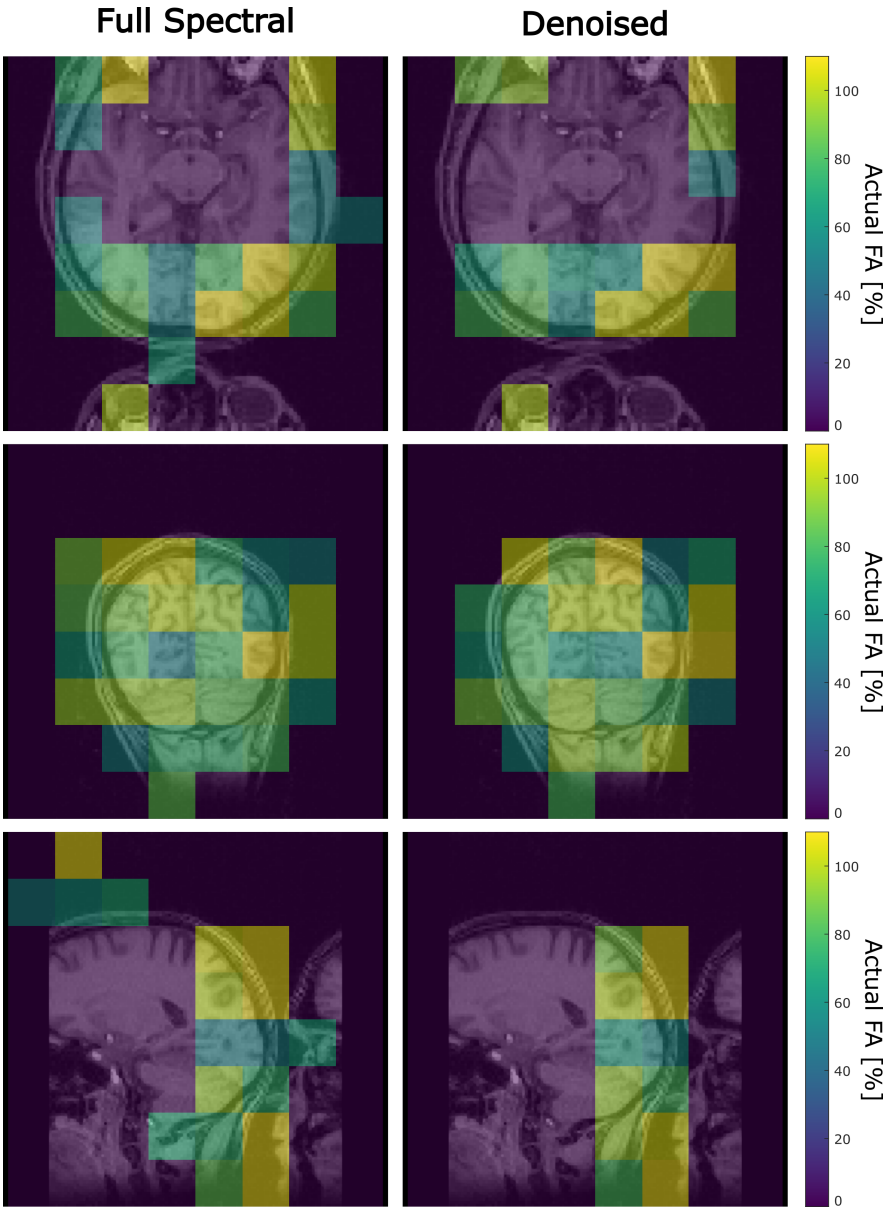


Figure 52: $B_1^+$ maps from the full-spectral MRF for the $^{13}$C in vivo data without (left) and with denoising (right). For all data, a representative slice is shown in transversal (top), coronal (center) and sagittal (bottom) orientation and overlaid with an anatomical image.

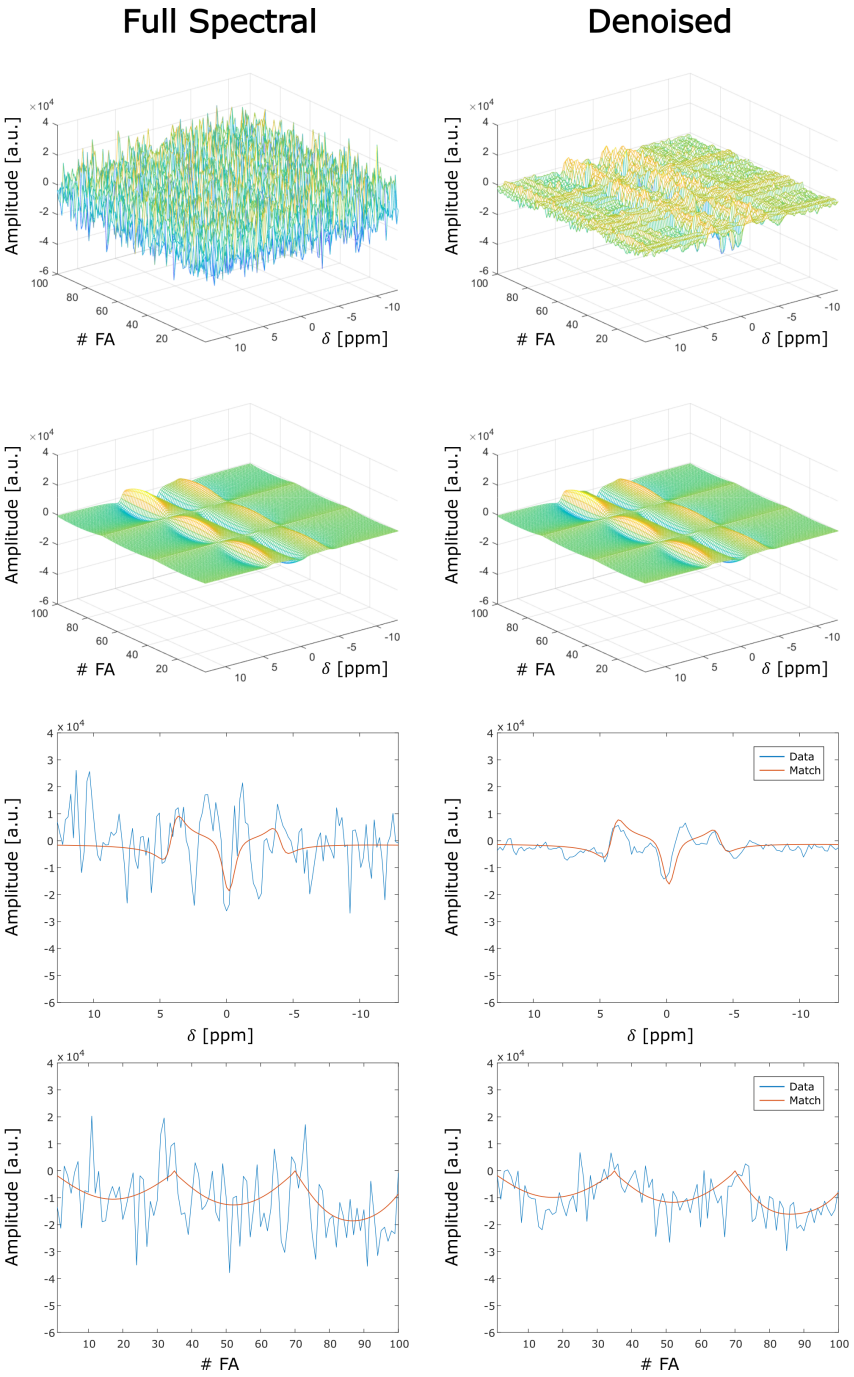


Figure 53: $^{13}$C in vivo spectral data of the full-spectral MRF with (left) and without denoising (right). The spectra over the whole FA pattern (1st row) are presented in comparison to the best match from the full-spectral MRF (2nd row). Moreover, the matched spectrum for the highest FA of 45° (3rd row) and the matched FA pattern at 0 ppm (4th row) are shown.

All other fingerprinting parameters agree to the non-denoised data, especially, the estimated $M_0$ distribution, which is strongly resembled. For all other parameters, $T_1$, $T_2$ and $\Delta B_0$, the maps are differing in some voxels, but agree on the overall estimated values.

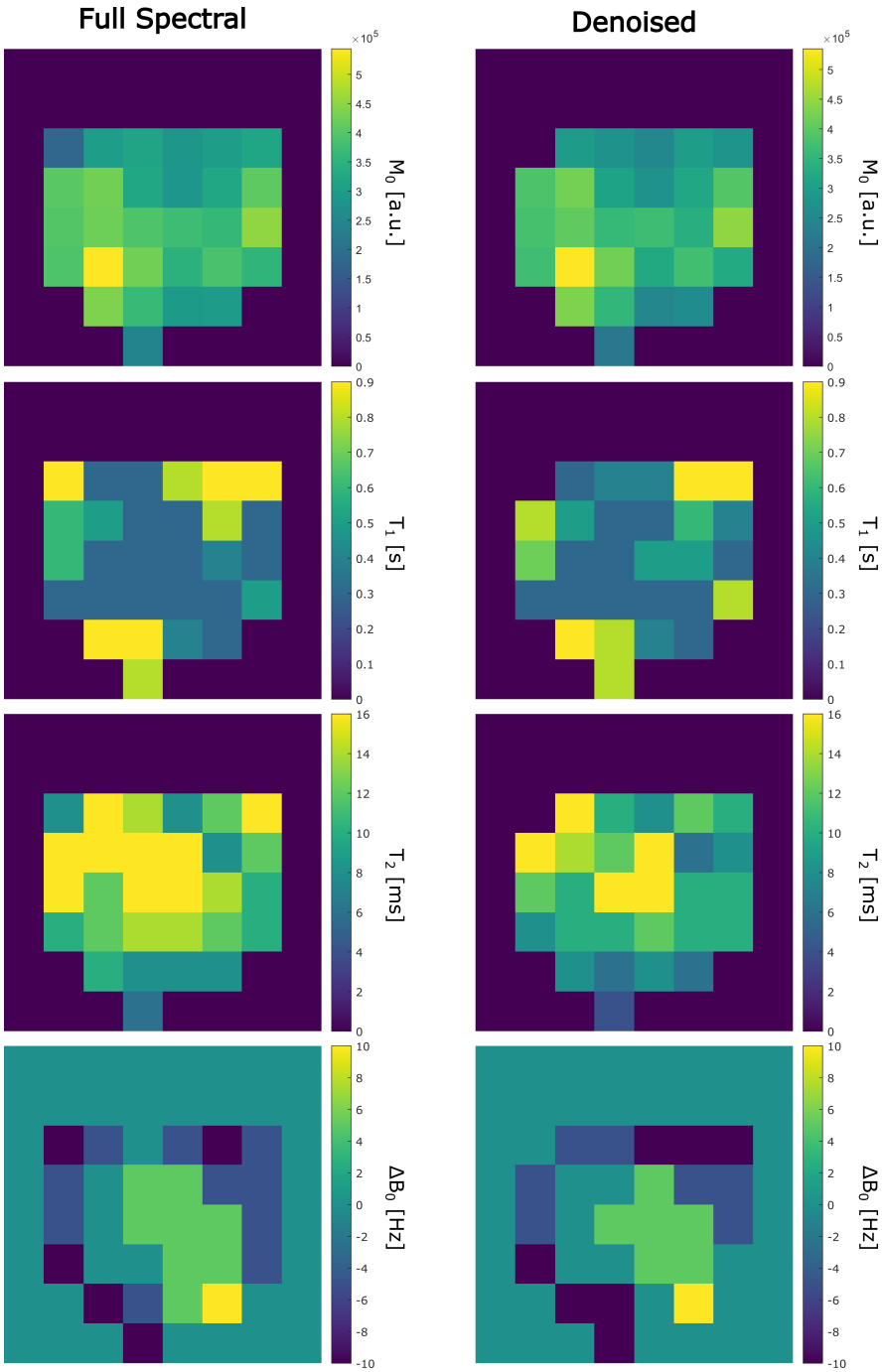


Figure 54: Representative coronal slice of the additional fingerprinting parameters from the full-spectral MRF for the in vivo $^{13}$C data with (left) and without denoising (right). The shown parameters are $M_0$ (1st row), $T_1$ (2nd row), $T_2$ (3rd row) and $\Delta B_0$ (4th row).

# 5. Discussion

HP experiments using $^{13}$C provide major clinical value through insights into the human metabolism and, hence, allow to investigate and assess various diseases [56]. This promising imaging modality, however, comes with great technical challenges, primarily, the short available measurement time, restricted by the rapid $T_1$ decay of the hyperpolarized state [57]. Therefore, a fast spectroscopic imaging sequence, namely radial echo-planar spectroscopic imaging (rEPSI), is presented to acquire high-quality spectral data with spatial resolution in a short amount of time. Additional advanced features, tailored to the time sensitivity of HP experiments and $T_1$-governed signal evolution, allow to extract maximum value out of a single data acquisition.

For comparison, typical acquisition parameters of the most commonly applied MR sequences in hyperpolarized $^{13}$C experiments are listed in the following:

| Sequence | TA | Spectral BW | Echo Number | Spatial Resolution | References |
|---|---|---|---|---|---|
| FID | 3 s | 10 kHz | 4096 | – | [17] |
| CSI | 25 s | 5 kHz | 512 | $(3.75\ \text{mm})^2$ | [18, 20, 58] |
| EPI | 3 s | – | – | $(5\ \text{mm})^3$ | [19] |
| bSSFP | 8 s | – | – | $(5.625\ \text{mm})^3$ | [20, 59] |
| EPSI | 13 s | 0.5 kHz | 32 | $(5\ \text{mm})^3$ | [58] |
| EPSI + CS | 2 s | 0.6 kHz | 32 | $(5\ \text{mm})^3$ | [60] |
| radial EPSI | 6 s | 1 kHz | 64 | $(15\ \text{mm})^3$ | [54, 61] |

Table 14: Comparison of the most commonly applied MR sequences in hyperpolarized $^{13}$C experiments. Listed are their acquisition time (TA), spectral bandwidth (BW), number of echoes and spatial resolution.

The most detailed spectral information is provided by free induction decay (FID) spectroscopy. Its acquisition time is very low, however, this comes at the cost of no spatial resolution. Chemical shift imaging (CSI) also allows for a high spectral detail but spatially resolved. However, especially when covering all three spatial dimensions, the measurement time is very high. Hence, CSI is mostly used for 2D measurements and in combination with acceleration techniques, like undersampling [62].
Sequences that are faster and spatially higher resolved, such as echo-planar imaging (EPI) or balanced steady state free precession (bSSFP), do not offer spectrally resolved data, but only metabolic maps for predefined resonances. Here, a distinction of resonance frequencies is only possible with the application of spectral-spatial excitation pulses or a multi-echo-based reconstruction. Both of these advanced acquisition techniques, however, require prior knowledge of a sparse number of

expected resonances, as well as a careful adjustment to the given experimental setting, such as $B_0$ inhomogeneity.
Lastly, echo-planar spectroscopic imaging (EPSI) is presented as a compromise between spectral and spatial sampling [63]. Just like CSI, an accelerated acquisition is necessary by usage of undersampling, also in combination with compressed sensing (CS) [60]. To achieve a high robustness against undersampling artifacts, a combination with a radial, spiral or concentric ring readout is recommended [54, 61, 64]. The downside is a broadened PSF, which on one hand increases the SNR, but on the other hand entails a lower actual spatial resolution and voxel-bleeding through a larger effective voxel size. Optimal application cases of the presented rEPSI sequence are, therefore, scenarios with (i) varying chemical shifts to determine pH in vivo [18, 65], (ii) tracers with manifold possible metabolic conversions, such as [1,2-$^{13}$C]pyruvate [66], and (iii) spectral matching of multiple resonances from the in vivo $^{13}$C lipid signals for MR fingerprinting.

# 5.1. Advancing Radial Echo-Planar Spectroscopic Imaging Towards a Versatile Imaging Tool

## 5.1.1. Advancing the Temporal Resolution

In order to be feasible in HP experiments, a significant acceleration of the rEPSI sequence is necessary. A straightforward approach to shorten the measurement time is the reduction of acquired $k$-space lines, also called spatial undersampling. The radial $k$-space coverage makes data more robust against undersampling and motion artifacts compared to the Cartesian one. This can be explained by the oversampling of the $k$-space center, which contain low spatial frequency components and, therefore, accounts for the overall shape of the measured geometry [8]. An undersampling, in the case of the rEPSI sequence, mostly affects outer $k$-space regions, as follows from eq. 58, leading to less defined structural edges in image space, what is not noticeable for the presented spatial resolution. However, as simulations revealed, the nominal voxel size is increased by a factor of approximately 1.5 compared to a Cartesian EPSI (see Appendix C).

Moreover, since each spoke means one additional excitation and the signal amplitude is proportional to the spoke number, the SNR is decreased with the undersampling factor, naturally yielding more pronounced undersampling patterns.

Qualitative observations of present artifacts were used to determine a threshold of five for the maximal possible undersampling factor. Furthermore, even above this threshold, artifact intensities were always about an order of magnitude below the signal amplitude, even in extreme undersampling cases with a factor of 20.

Using the undersampling factor of five, also reduces the total measurement time (TA) by the same factor with virtually no drawback. In the case of the used parameters with a matrix size of $16 \times 16 \times 16$, this brings the TA from 105 s down to only 21 s. Compared to a normally shorter Cartesian EPSI readout, where $16 \times 16$ $k$-space lines have to be acquired, a measurement time 67 s of would be needed, assuming identical TR.

Usually applied accelerated 3D sequences, like CSI, EPSI or bSSFP, range from 2 s to 8 s in TA (see Table 14), while relying on advanced reconstruction techniques, like CS or iterative decomposition with echo asymmetry and least squares estimation (IDEAL) [58–60]. In comparable in vivo settings, the presented rEPSI only took 6.3 s, through usage of simple undersampling and a lowered number of echoes.

This shortened measurement time, hence, enables not only to apply the rEPSI in HP experiments within the in vivo $T_1$ relaxation ($\sim$ 20 s), but also below that, accomplishing to capture dynamic metabolic information over a large spectral range.

This compatibility to undersampling could be even more exploited by the use of CS algorithms, which allow for higher undersampling factors and, therefore, even less measurement time.

Another challenge of the $T_1$ decay for the acquisition of hyperpolarized $^{13}$C data is that early acquired spokes are weighted with a higher intensity while the contribution of most later spokes are almost reduced to zero. Especially for a short $T_1$ time, like the simulated 13 s, a value extracted from prior rat measurements, this results in an uneven intensity distribution in $k$-space. In turn, signal is wrongly attributed to initially sampled directions in $k$-space, what produces blurring artifacts in the corresponding directions in image space.

Hence, a correction for this blurring effect is highly necessary, since most applied $^{13}$C substrates, have an in vivo $T_1$ time in that order [18, 54, 67]. The presented novel golden angle gapped arrangement (GAGA) [22] successfully removed $T_1$-based blurring by increasing the distance between successive acquired $k$-space lines and, therefore, achieving a more homogeneous signal distribution. Even though still present, this effect is now reduced significantly, providing much sharper and accurate intensity maps.

Additionally, the GAGA can, in principle, be easily implemented to all similar radial acquisitions [61, 62] without the need to modify the reconstruction pipeline.

In comparison to previous 2D golden-ratio-based methods [68, 69], the novel GAGA scheme enables not only to have a homogeneous $k$-space distribution in all three spatial dimensions, but also the division of one MRSI dataset into multiple undersampled subsets. Each of these subsets again have an optimized homogeneous $k$-space sampling [22]. Via sliding window (SW) reconstruction of these subsets, an investigation of metabolic dynamics becomes possible with a temporal resolution from $\Delta t = M_{\text{sub}} \times$ TR down to TR. Especially for in vivo applications this is of major interest, as it enables a more detailed analysis of the metabolic dynamics, possibly revealing processes on a smaller timescale that have not been resolved before.

This also allowed for a quantification of the $T_1$ decay, which was compared for the three shown cases of $\Delta t = [0.26, 2.60, 5.20]$ s. Here, no used $\Delta t$ showed a significant deviation for the fitted values $T_1 = [(12.80 \pm 0.27), (12.14 \pm 0.62), (11.47 \pm 0.62)]$ s from the true applied $T_1$ of 13 s.

Overall, the fit becomes more accurate and shows a smaller error by using a smaller window step size $\Delta t$, naturally resulting from a higher number of available datapoints.

Nevertheless, especially for the smallest $\Delta t =$ TR, a structured flickering in signal intensity is visible, due to an inherent signal distribution in $k$-space and its acquisition,

which depends on the spoke orientations. The reasoning that this flickering is connected to the covered $k$-space is especially supported by the in vivo data from Section 4.2.2. Here, the same GAGA scheme is applied multiple times and results in a very similar flickering pattern for each repetition, since the underlying geometry of the measured subject, and with that the signal distribution in $k$-space, does not change and the same spokes are sampled.
This means, in turn, that for a small subset spoke number $M_{\text{sub}}$ and small time steps $\Delta t$, each spoke sliding in and out of the observed reconstruction window, majorly contributed to the total signal, hence resulting in a larger flickering effect.
In conclusion, generally, a smaller window step size is favorable, since it provides more datapoints and shows to result in a more accurate $T_1$ estimation. However, this probably only holds to be true, if the investigated dynamics are covered over a significant time span, as in the presented EG data, where $T_1 = 13$ s $<$ TA $= 105$ s. With a decreasing total measurement time TA (or a longer $T_1$), the contribution of the flickering could overtake and possibly hinder quantification of $T_1$ or similar occurring dynamics.
Nevertheless, the flickering could be corrected, since for the EG phantom, also the underlying, non-$T_1$-weighted data exists, allowing to extract the aforementioned inherent signal distribution in $k$-space. As expected, an improvement of the $T_1$ estimation could be achieved, especially lowering the error. This is also reflected in the shown $T_1$ maps, which are much more smooth and closer to the true value of $T_1 = 13$ after applying the correction. Unfortunately for in vivo experiments, no such reference data can be acquired. Nonetheless, a correction is potentially possible by using regularization techniques in the temporal dimension [70].

### 5.1.2. Advancing Spectral Resolution

An accurate knowledge of the $T_1$ decay can be used for further advanced data acquisition schemes, like a $T_1$ compensation via VFAs. The in vivo data shows a successful compensation of the $T_1$ decay, using an predicted $T_1$ value, which was taken from prior executed in vivo HP measurements using [1,2-$^{13}$C]pyruvate. For the compensated data, an almost perfectly steady signal intensity over the full measurement time could be achieved. This techniques proved useful for either ensuring a complete and efficient usage of all available HP signal and, as presented in the following, allowed for application of echo-train shifting (ETS).
However, as it is noticeable for the slight overcompensation at the last 10% of acquired spokes, this technique is extremely sensitive to deviations from the estimated $T_1$. In cases without prior knowledge of the approximate $T_1$, the $T_1$-compensating VFA scheme

produced an overcompensation higher than the normally occurring intensity change due to the $T_1$ decay. This can proof problematic in vivo, where conditions are prone to large changes through different compartments. An example would be the time, in which the HP substrate is in the blood cycle, where the additional dipolar interactions with the iron result in a higher relaxation rate [71].
Moreover, this $T1$ compensation is primarily necessary, when high fluctuations in spoke intensities are present. This would be the case for experiments where $T_1 \ll$ TA. For all other cases, the fluctuations are expected to be rather small and hence, a possible overcompensation might result in higher artifacts than the original influence of $T_1$.
Overall, the $T_1$ compensation shows a good synergy with the presented rEPSI data, as it provides various ways of estimating the $T_1$ decay and therefore, allows a highly accurate compensation for future measurements.

Now, making use of the steady spoke intensities after $T_1$ compensation, ETS could be applied during HP experiments without major ghosting artifacts. An ETS factor of two resulted, as expected, in a doubled spectral bandwidth [26]. Its application resulted in less phasing, as well as virtually no ghost artifacts, compared to the interleaved recombination approach [51], since all spectral points $n$ can be sampled while traversing $k$-space in same direction. Additionally for the ETS data, a summation of the odd and even data is possible, increasing the SNR by a factor of $\sqrt{2}$.
Moreover, the results show that for non-steady spoke intensities, like in the case of a $T_1$ decay during HP experiments, it is favorable to acquire associated ETS directly after one another. This way, the additional signal oscillation caused by the $T_1$-based spoke intensity differences, which causes ghost artifacts, is minimized.
However, it should be noted that the downside of using ETS is the doubled measurement time, resulting in a strongly decreased intensity of later acquired spokes through the $T_1$ decay. With the use of $T_1$-compensating VFAs, this yields a lower overall signal amplitude, and without it, again stronger ghost artifacts.
For the in vivo experiments, the usage of ETS was combined with the $T_1$-compensating VFA scheme, since the complex spectral patterns for [1,2-$^{13}$C]pyruvate would be impossible to quantify when ghost artifacts are present.

## 5.2. Application of Radial EPSI to Metabolic Imaging of Hyperpolarized $^{13}$C-Pyruvate In Vivo

[1-$^{13}$C]Pyruvate represents the most widely used HP $^{13}$C tracer, as it is not only central in the human metabolism, but also provides a relatively long $T_1$ value [34]. In this work, a successful metabolic imaging of [1-$^{13}$C]pyruvate by the use of rEPSI is demonstrated in vivo. Moreover, the previously presented advanced acquisition and reconstruction schemes are applied to extract detailed spectral information with a high temporal resolution. This served as a proof-of-principle to prove the feasibility and stability regarding in vivo HP experiments. In a final application, [1,2-$^{13}$C]pyruvate was investigated, where the full spectral capabilities and advantages of the rEPSI could be demonstrated.

### 5.2.1. Metabolic Imaging with [1-$^{13}$C]Pyruvate

This work demonstrates the feasibility of the advanced rEPSI sequence for the use in HP experiments under in vivo conditions.

The intensity distributions show that all measured metabolites are most prominently found near the heart as [1-$^{13}$C]pyruvate is injected into the blood stream. Also the blood vessels connecting the heart with the injection site in the tail show a higher signal. For [1-$^{13}$C]lactate, the signal is slightly more spread along the coronal slice, suggesting a higher conversion within the muscle tissue of the hind legs.

Directly after injection, the [1-$^{13}$C]pyruvate signal is the highest, while the conversion into [1-$^{13}$C]lactate and [1-$^{13}$C]alanine can be observed as an initial build-up. The general timing of a maximal [1-$^{13}$C]lactate and [1-$^{13}$C]alanine signal after around 15 s was in line with literature [72–74]. Nevertheless, as this metabolic conversions happen within a very short time frame and the acquisition time of $\sim 6$ s cannot be neglected, already for the first timepoints signals from the downstream metabolites are present. This is especially observable for the abdominal area, in which a higher and faster perfusion with the metabolites was seen. Nevertheless, for peripheral structures, like the leg muscles, more of this build-up can be detected, since it took longer for the [1-$^{13}$C]pyruvate to arrive through the blood circulation and conversion started with a significant delay.

Moreover, for peripheral voxels, worse spectral quality can be observed. This can be explained by multiple phenomena, like lower SNR, voxel bleeding and susceptibility artifacts. The lower SNR is caused by the just described later arrival of the [1-$^{13}$C]pyruvate bolus, since that means more time for relaxation processes within the blood stream as well as a generally higher signal reduction through $T_1$ relaxation.

Voxel bleeding is especially relevant, when the MRSI data has a low spatial sampling, meaning larger voxels, as it is very much the case for $^{13}$C in vivo measurements. Therefore, the signal from neighboring voxels produces significant spectral contamination (see Appendix C), which results in broader peaks and even a peak doubling due to local changes in resonance frequency due to $B_0$ inhomogeneities.

Lastly, susceptibility changes arise at boarders of different materials, including tissue types and even air. Since every material effects the surrounding magnetic field through its magnetic properties, such as diamagnetism or paramagnetism, local changes in Larmor frequency and relaxation times can occur. These, in turn produce image artifacts through false spectral and spatial assignment of the MR signal.

As already discussed in Section 5.1.1, the additional timepoints from the SW reconstruction allow for a finer temporal evaluation of the dynamic processes. However, the presented data from the previous rat measurement does not come from subsets within one main dataset, but eight undersampled repetitions. Hence, the temporal flickering shows the exact same pattern, resulting from the same specific $k$-space signal distribution, since the GAGA is restarted and the same spokes are covered.

Within one acquisition (TA = 6.3 s $< T_1 \sim$ 13 s), this flickering hinders an accurate evaluation of the dynamics, like assessing $T_1$, but over the full eight repetitions ($8\times$TA = 50.4 s $> T_1 \sim$ 13 s), this effect is minimized.

Overall, the SW data resulted in a more precise determination of the $T_1$ time for [1-$^{13}$C]pyruvate, compared to just using the eight measurements. No only the error values from the evaluated coronal slice were smaller, but also the fitting uncertainty. The determination via the $k$-space center data proved to be the most precise, as it yielded not only the most datapoints, i.e. $8 \times 60$, one for each spoke, but also had the highest SNR from the whole volume. However, this also means loss of the spatial information.

All in all, the SW reconstruction is deemed most valuable, as it preserved all spatial information, but extends the temporal resolution for a more precise dynamic evaluation. In addition to the $T_1$ determination of [1-$^{13}$C]pyruvate, it also revealed more of the metabolic conversion into [1-$^{13}$C]lactate and [1-$^{13}$C]alanine making it a valuable extension of the reconstruction pipeline. All of these observed dynamic processes correspond to literature [20, 75, 76].

The acquired MRSI data for a small cohort of tumor-bearing rats, shows consistent results for the observed dynamics of metabolic conversion and $T_1$ decay of the injected [1-$^{13}$C]pyruvate, demonstrating the reliability and reproducibility of the rEPSI

acquisition in vivo.
During the time course of three weeks after applied radiation therapy to the tumors in the right hind leg, a decrease in lactate-to-pyruvate ratio was expected [72, 77, 78], based on a suppressed Warburg effect [36]. However, no significant therapy response could be detected based on the determined lactate-to-pyruvate ratios, even though the obtained values were in line with literature [20, 72, 73, 75].
Literature suggests that a single irradiation may not be sufficient to treat a tumor, as a fractionation approach has shown to be more successful [78]. In this regard, no other method was applied to check the tumor status, such as a biopsy to quantify LDH activity. Hence, it cannot be confirmed whether the applied treatment even caused positive effects.
Further reasons for no observable changes are the absence of the healthy reference group, as the metabolic activity within the healthy leg might still be affected by overall changes due to the tumor response of the irradiation itself. Hence the comparison within one rat might be insufficient.
Another potential reason why no response could be detected, is the large time steps between the control measurements of weeks (and not days or even hours) and the small sample size of six animals. To provide a higher statistical confidence, experiments have to be conducted on a smaller timescale and with a larger cohort.
Lastly, and most importantly, the spectral data is compromised by the previously mentioned factors, like voxel bleeding and susceptibility artifacts, especially because in most cases, the tumor volume was smaller than the actual voxel size of the rEPSI acquisition and localized at the very periphery of the rat's leg.
Overall comparison showed that the presented rEPSI sequence is as fast or even faster than the employed sequences in similar settings [72, 77, 78], allowing for a sufficient quantification of the metabolic dynamics. However, in most cases, additional non-localized FID data was used to supplement the investigation and, more importantly, a much smaller voxel size was chosen. In this work, due to gradient hardware limitations of the used clinical MR scanner, no higher spatial resolution was possible. This and the peripheral position of the tumor are the most likely reasons for no possible treatment response detection. However, in principle, with an adequate experimental set-up, a quantification of a treatment response via usage of the rEPSI should be possible.

### 5.2.2. Metabolic Imaging with [1,2-$^{13}$C]Pyruvate

This work presents the first MRSI acquisition of hyperpolarized [1,2-$^{13}$C]pyruvate, as prior investigation was conducted only using non-localized FID sequences [17, 66].
All expected peaks of the first label of [1,2-$^{13}$C]pyruvate could be detected, which

were already observed in the previously shown [1-$^{13}$C]pyruvate data. The second label produces resonances from the same molecules, but also potentially gives rise to further peaks of downstream metabolites from the citric acid cycle [10, 33]. Additional molecules for the first label, which were reported in literature, are $^{13}$C-bicarbonate and $^{13}CO_2$.
However, [2-$^{13}$C]lactate, [2-$^{13}$C]alanine and $^{13}CO_2$ occur at more than 50 ppm upfield and could not be captured [17, 79, 80]. The molecules of the citric acid cycle are already reported for low concentrations in the non-localized data, mostly overlap with the aforementioned high SNR metabolites and could therefore not be detected [17, 66]. Lastly, $^{13}$C-bicarbonate resonates at $\sim$ 10 ppm upfield from [1-$^{13}$C]pyruvate, but could also not be observed due to the low concentrations within the rat's metabolism [75].
The overall intensity distribution for [1,2-$^{13}$C]pyruvate shows similar behavior as for the previously presented [1-$^{13}$C]pyruvate data. The spectral quality after usage of ETS and $T_1$-compensating VFA is high, resulting in a reliable AMARES fitting for all observable metabolites and in all voxels, even in peripheral ones.
For the shown second [1,2-$^{13}$C]pyruvate label, a shift of the intensity maps regarding the underlying anatomy can be seen, although the same distribution as for the first [1,2-$^{13}$C]pyruvate label resonance is expected, since both signals stem from the same molecule. This can be explained by the distance in the spectral range, producing a chemical shift artifact. All measured first label metabolites are in close range (within 20 ppm or $\pm$300 Hz). The doublet of the second label [1,2-$^{13}$C]pyruvate is located about 40 ppm downfield, equal to approximately 1200 Hz in frequency. To calculate the chemical shift displacement $\Delta r$, eq. 39 can be used by inserting these frequency difference $2\pi\Delta f$ for the Larmor frequency $\omega_0 = \gamma B_0$:

$$\Delta r = \frac{2\pi\Delta f}{\gamma G_{\mathrm{Amp}}} \tag{76}$$

where the gradient amplitude $G_{\mathrm{Amp}}$ was 20.27 $\frac{\mathrm{mT}}{\mathrm{m}}$ for the settings used in this section. The resulting errors in the assigned spatial position $\Delta r$ are then $\pm$1.4 mm for the close-by first label metabolites, but 5.5 mm, when comparing the first to the second label of [1,2-$^{13}$C]pyruvate. With an zerofilling factor of two and a voxel size of 7.5 mm, this is almost a full voxel shift. Hence, this effect is not noticeable for all close-by resonances, but produces a significant shift for the second [1,2-$^{13}$C]pyruvate label.

## 5.3. Application to In Vivo $^{13}$C $B_1^+$ Mapping Using Magnetic Resonance Fingerprinting

As previously explained, an accurate knowledge of the actual transmitted FA is necessary for the conduction of HP experiments. However, achieving stable $B_1^+$ mapping is complicated by the extremely low SNR of the naturally abundant $^{13}$C MR signal, especially in body parts with low fat content, such as the human head.

Literature approaches, therefore, often measure a highly concentrated phantom prior to the in vivo experiments or use the signal of Sodium-23 ($^{23}$Na ) as an indirect calibration that requires a double-resonant $^{23}$Na /$^{13}$C coil [81]. Others apply the Bloch-Siegert shift method, which has been described as tedious and highly user-dependent for the low SNR from $^{13}$C [82]. Further methods are applied during the HP experiments themselves, which, therefore, do not allow for adjustments before acquisition and additionally drain the limited signal needed for the metabolic measurements [83, 84]. Moreover, all of the mentioned calibrations rely on a large FA $\geq 90°$, while the HP experiments usually employ very small FA.

In contrast, this work demonstrates $B_1^+$ mapping via magnetic resonance fingerprinting (MRF), allowing for a direct application before in vivo scans and more accurate predictions in low FA regimes [28]. The spectral complexity of the lipid signals could be used as an advantage, as the rEPSI sequence not only offers spatial, but also spectral analysis of the $^{13}$C data, leading to a more robust $B_1^+$ estimation.

Previously, the usage of MRF during hyperpolarized $^{13}$C experiments has already been demonstrated as a method for the estimation of kinetic rates of [1-$^{13}$C]pyruvate [85].

The first presented $B_1^+$ MRF mapping method uses the AMARES fits of multiple spectral resonances. As this depends on a stable fitting process, a higher SNR is beneficial, which is given for $^1$H and $^{13}$C measurements of the EG phantom, producing stable $B_1^+$ maps in both cases. However, simulation predicted an error of $\sim 8\%$ at the $^{13}$C in vivo SNR, which was also reflected in much more prominent fluctuations in the shown $^{13}$C EG maps, compared to a smoother DA mapping as reference.

The other matched parameters, i.e. $T_1$, $T_2$ and $\Delta B_0$, showed a similar effect. Prediction and consistency of the AMARES-based MRF worsened for the SNR of $^{13}$C EG. Only $T_1$ values were rather consistent, as the simulation omitted the FID evolution over time, which is mostly influenced by $T_2$ and $\Delta B_0$. $T_1$, next to $B_1^+$, is best reflected when only matching FA patterns.

Besides using the AMARES fits for the matching process, this thesis presents another novel MRF approach, which uses the full simulation of the complete spectral data.

Hence, this full-spectral method does not rely on the goodness of the fit and uses the full information of the spectral offsets within the acquired BW.

The resulting $B_1^+$ maps were comparable to the AMARES-based approach. Simulating a reduced SNR revealed that the predicted actual FA fluctuates much less, especially at very the low SNR values in vivo, i.e. only $\sim 2\%$.

Moreover, as this approach simulates the full spectral information with $T_2^*$ decay, it provides more reliable estimations for $T_2$ and $\Delta B_0$. Nevertheless, yet no detailed in-voxel $\Delta B_0$ distribution could be implemented, as this would add another fingerprinting parameter and increase the computation time. The used off-center frequency, therefore, only provides a $\Delta B_0$ estimation between neighboring voxels.

Additional caution is necessary for the assumed spectral pattern, i.e. the expected resonances as well as their relative amplitudes. The simulated fingerprints partially showed a higher deviation in amplitude for the matched FA pattern, since the full-spectral matching uses a combined objective between spectra and FA pattern. Hence, the match of the FA pattern amplitude can fluctuate depending of the provided spectral information. Note, that this does only affect $M_0$ through the amplitude, but not the other parameters, as they are dependent on the shape of the FA pattern [28].

Lastly, the effect of an increased acquired spectral information for the stability of the estimated actual FA was investigated. It could be demonstrated that below a certain number of echoes, a strong underestimation of the $B_1^+$ occurs. Especially, below a spectral resolution of $\sim 60$ Hz, the deviations from the DA reference maps increases significantly. This result underlines the importance of the spectral information, making the full-spectral MRF approach more stable than commonly used non-spectroscopic MRF acquisitions [28]. Moreover, through a combined matching of FA pattern and spectra, the full-spectral approach is robust enough to only rely on a coarse spectral sampling and therefore reduce the TA drastically.

The total measurement time in vivo was 17.4 min, as more echoes and spokes were acquired to ensure sufficient signal and information for a successful matching. However, prior results from phantom measurements suggest that a lower spectral resolution is sufficient for a stable matching and that this time could be shortened at least by a factor of four, or possibly even eight, by decreasing the TR. Lowering the TR to only 0.025 s would lead to a shortened TA of 2.2 min. This decrease in measurement time makes this approach an applicable calibration method in clinical settings, as comparable $B_1^+$ mapping methods for $^1$H take about $\sim$ 1 min [28]. Nevertheless, a longer measurement time might be needed to ensure stability in vivo. Also, all computation beyond the actual acquisition, i.e. the matching, can be done parallel to anatomical imaging, allowing for efficient time usage.

In conclusion, the full-spectral MRF approach is more promising for in vivo application, as it not only performs more stable under low SNR conditions, but also as this robustness allows for a decreased TA and with that, lowers the waiting time for patients.

In order to test the feasibility of the presented $^{13}$C $B_1^+$ mapping in vivo, the head of a healthy volunteer was measured with the rEPSI MRF sequence.
The complex spectral information of lipids in the human head are not resolvable with rEPSI at the employed excitation number and spectral resolution. Therefore, only a three peak model approximation was applied for the spectral matching. This was based on observations from prior rEPSI acquisitions and yielded a sufficient overlap for lower resolution data with a higher SNR.
Overall, the acquired in vivo $^{13}$C data was extremely noisy, not allowing to verify the fit and matched results visually below a voxel size of $(50\ \text{mm})^3$. In further analysis, only the full-spectral approach was used, since it demonstrated a higher reliability for low SNR data. The MRF algorithm is very stable against high noise levels by design [27]. This is supported by the denoised data, as the MRF results do not significantly change.
The final actual FA maps only achieved a sufficient matching accuracy in the periphery of the head, especially in the back. This could be caused by a higher lipid signal from the neck muscles, possibly in combination with voxel-bleeding. To have certainty over the origin of the $^{13}$C signal in the human head, a longer measurement with more averages and a higher spatial resolution is necessary. Moreover, all shown MRF results can be further improved by a finer step size for the fingerprinting parameters of the dictionary. In the shown study, the applied FA was only estimated in 5% steps, but, in principle, the only limit of lowering this accuracy is the increased dictionary size and, with that, the computation time. Especially in lower SNR scenarios, smaller estimation steps should be considered, as with an increased fluctuation of the acquired signal, the resulting fingerprint would only change with, for example, 1% instead of the shown 5%. However, as the full-spectral approach seems to have a higher sensitivity to the other matched parameters, e.g. the relaxation times, this would also demand finer matching of all other fingerprinting parameters, therefore, increasing the computation time drastically. A final decision over what the optimal estimation step size should be is dependent on the experiment itself and needs further investigation for a concrete answer.

# 6. Summary and Conclusion

Magnetic resonance (MR) spectroscopy using hyperpolarized $^{13}$C-labeled tracers enables the investigation and assessment of various metabolic diseases in real-time. However, due to the rapid decay of the hyperpolarized state, employed acquisition techniques are required to be fast and make the most efficient use of the available signal. In particular, achieving high spatio-spectral resolution in short measurement times remains challenging.
This thesis showcases radial echo-planar spectroscopic imaging (rEPSI) as a versatile imaging tool for the use in hyperpolarized $^{13}$C MR experiments in vivo. Through optimization to the specific needs of various use cases, rEPSI enables to acquire high-quality spectroscopic data, spatially resolved in 3D, within the short available measurement time. It not only enables the use of hyperpolarized $^{13}$C tracers, which are based on chemical shift information, but also to estimate experimental parameters like $T_1$ and $B_1^+$ through MR fingerprinting (MRF) of complex spectral data.

Starting from a basic sequence implementation on a clinical 3 T MR scanner, the radial EPSI approach was expanded by several features, such as (i) $k$-space undersampling, (ii) optimized $k$-space spoke ordering, (iii) sliding window (SW) reconstruction, (iv) variable flip angle (VFA) excitation, and (v) expansion of the acquired spectral bandwidth (BW) by echo-train-shifting (ETS). In the course of this work, these advances were employed in two very distinct scenarios: Metabolic imaging of hyperpolarized $^{13}$C MRSI with [1-$^{13}$C]pyruvate and [1,2-$^{13}$C]pyruvate in small-animal studies, and MRF using thermally-polarized $^{13}$C signals to estimate the $B_1^+$ field of $^{13}$C MR coils.

In order to accelerate the rEPSI for its use in hyperpolarized $^{13}$C experiments, the robustness against $k$-space undersampling was investigated. It was demonstrated that for an undersampling factor of up to five, no significant artifacts appeared, allowing to shorten the acquisition time accordingly. Additionally, a homogeneous coverage of $k$-space was implemented in form of a spoke reordering, namely golden angle gapped arrangement (GAGA). For hyperpolarization (HP) experiments, where the spoke intensities decrease with the $T_1$ relaxation time, GAGA successfully prevented blurring artifacts. Moreover, GAGA enabled an SW reconstruction, yielding multiple subsets from a single rEPSI measurement with a high temporal resolution.
Applying the described optimized rEPSI sequence to metabolic imaging in vivo using hyperpolarized [1-$^{13}$C]pyruvate, 4D MRSI data of a large matrix size could be acquired within only $\sim$ 6 s with a spatial resolution of (15 mm)$^3$ and spectral resolution of

$\sim$ 16 Hz over a BW of 1000 Hz. This very short acquisition (TA) time allowed the acquisition of multiple repetitions, resulting in a 5D dataset, which captures dynamic metabolic information over 50 s with a temporal resolution of TA $\sim$ 6 s. Through SW reconstruction, an even finer sampling of only $\sim$ 0.1 s could be achieved.

The reproducibility of the advanced rEPSI sequence was demonstrated in a study using hyperpolarized [1-$^{13}$C]pyruvate that was conducted in a cohort of six tumor-bearing rats. In all subjects, consistent observations of their metabolism were made, however, no tumor-specific response to the applied radiation therapy could be detected.

Next, volumetric data with 3D spatial resolution and complex spectral patterns from hyperpolarized [1,2-$^{13}$C]pyruvate was acquired in vivo. To this end, additional advanced rEPSI features were implemented, such as a $T_1$-compensating VFA scheme, which ensured a steady signal amplitude over all acquired $k$-space spokes. This, in turn, enabled the use of ETS to obtain a sufficient spectral BW without spectral ghost artifacts.

Through these advanced acquisition features, for the first time, 4D MRSI data of [1,2-$^{13}$C]pyruvate could be acquired during an in vivo HP experiment. The full TA was 17 s and showed a spatial resolution of (15 mm)$^3$ and a spectral resolution of $\sim$ 16 Hz over the increased BW of 2000 Hz.

For all aforementioned applications using transient HP, an exact knowledge of the applied actual flip angle (FA) is indispensable. The second presented use case for the rEPSI sequence covers this need by a restructuring of the acquisition scheme and usage of a $B_1^+$-sensitive VFA pattern to enable a novel MRF-based $B_1^+$ estimation for $^{13}$C. This not only proved the versatility of rEPSI once more, but also demonstrated the advantages of acquiring spectral information by exploiting the complex $^{13}$C spectra of lipids in vivo.

Two different novel MRF quantification methods were implemented, one using fitted spectral resonances and the other matching the complete acquired spectral information, as well as a double-angle mapping approach were compared. Herewith, the consistency in $B_1^+$ mapping via the rEPSI-based MRF could be demonstrated, as well as the advantages of a detailed acquisition of spectral data. Matching of the full acquired spectral BW made this $B_1^+$ mapping approach more stable in regards to low SNR, suggesting an uncertainty of only $\sim$ 2% for $^{13}$C in vivo data, while a low spectral resolution of only $\sim$ 50 Hz was deemed sufficient. The latter would enable a short acquisition time of only 2.2 min, sufficiently short for clinical settings, in which an accurate FA calibration prior to HP experiments would be possible, while using the

exact same coil and FA shape.
Finally, the in vivo application using the low $^{13}$C signal from lipids in the human head was successfully demonstrated, yielding estimated $B_1^+$ values in the back of head with a spatial resolution of $(25\ \text{mm})^3$.

In conclusion, this work demonstrates the various advantages of an MRSI acquisition via rEPSI for hyperpolarized $^{13}$C experiments, as it not only provides high-quality spectral information with 3D spatial resolution within a short measurement time, but also allows for an intra-acquisition investigation of $T_1$ decay and metabolic dynamics and even pre-scan $B_1^+$ estimation via MRF.
Possible future research of [1,2-$^{13}$C]pyruvate, especially in regards to a more detailed investigation of metabolites further downstream [66]. Moreover, an assessment of metabolism via pH sensors [65, 86] would be a target application, where a fast and detailed spectroscopic acquisition in three spatial dimensions is demanded as well. In both cases, the advanced rEPSI sequence is not only faster than currently applied methods, but provides detailed spatio-spectral information for a precise quantification of frequencies.
Lastly, the $B_1^+$ mapping via MRF could not only be applied as a calibration prior to hyperpolarized $^{13}$C experiments, but could also be extended to other X-nuclei. For example, experiments using Phosphorus-31 ($^{31}$P) could benefit from this method [87], as the sensitivity in the human head is considerably higher. This would enable a more stable $B_1^+$ estimation as well as potential mapping of further parameters, like $T_1$, $\Delta B_0$ and exchange rates [38].

As shown in this thesis, rEPSI was advanced as a versatile imaging tool with enormous potential in various settings for hyperpolarized $^{13}$C MRSI in vivo.

# Appendix

## A. Molecular Structure of Ethylene Glycol

In Figure 55, the molecular structure of ethylene glycol is shown. Through a high concentration, even at the low natural abundance of 1.1%, enough $^{13}$C nuclei are present to achieve a sufficient MR signal for measurements. The $J$-coupling with the neighboring $^{1}$H atom produces a spectral triplet.

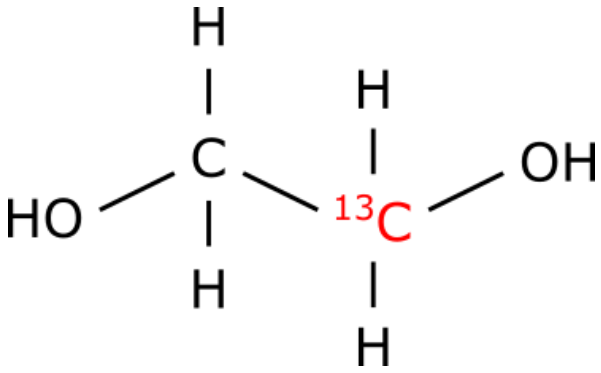


Figure 55: Molecular structure of ethylene glycol with a naturally occurring $^{13}$C nucleus.

# B. Injection through a Metal Syringe

To investigate the potential cause for the diminished polarization, which was observed in some measurements during the works of this thesis, an experiments was conducted with two 1.5 mL Eppendorf Safe-Lock® tubes (Eppendorf SE, Hamburg, Germany). Both tubes were filled with the same dissolution of hyperpolarized [1-$^{13}$C]pyruvate, which was injected through a syringe. Once a plastic cannula and once a metal cannula was used. The intensity maps of [1-$^{13}$C]pyruvate were acquired with the rEPSI sequence and are shown in Figure 56.

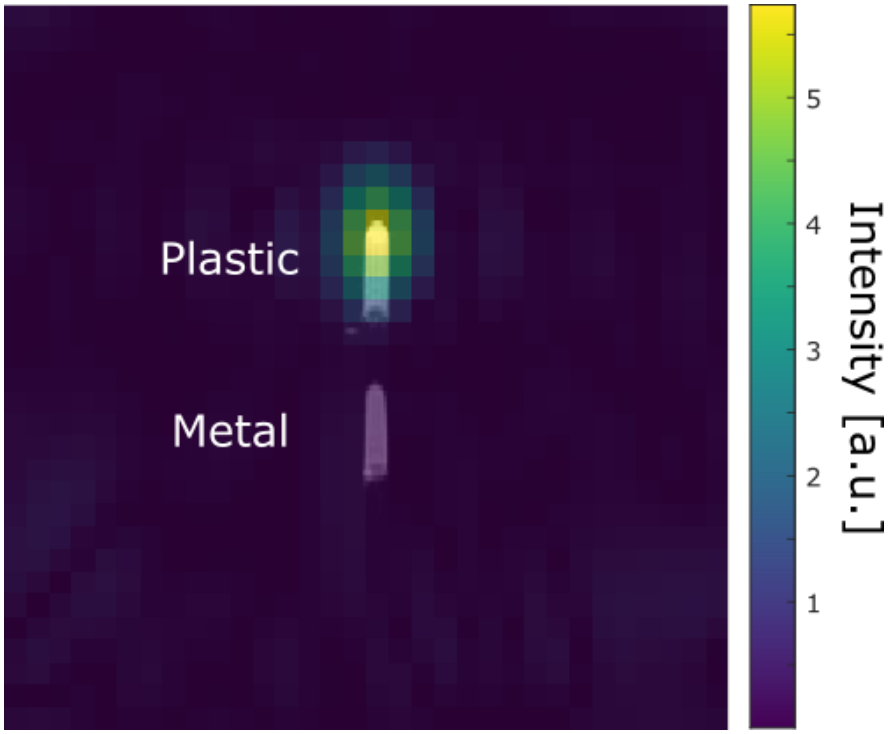


Figure 56: Comparison of the hyperpolarized [1-$^{13}$C]pyruvate signal after injection through a metal or a plastic cannula.

As it can be clearly seen, the injection with the plastic cannula successfully provided the increased $^{13}$C signal, whereas in the case of the metal cannula, no signal could be detected. This confirmed observations in prior in vivo experiments and also later published findings [44]. As a consequence, no metal components were used for any further injections.

# C. PSF Simulation

In order to compare the actual voxel size between a Cartesian EPSI and the presented radial version, the PSFs were simulated. For that purpose, a dataset with signal in only one point was created and accordingly reconstructed. The chosen parameters were taken from the conducted in vivo experiments, shown in Table 3. In Figure 57, the resulting PSFs are shown along one spatial dimension.

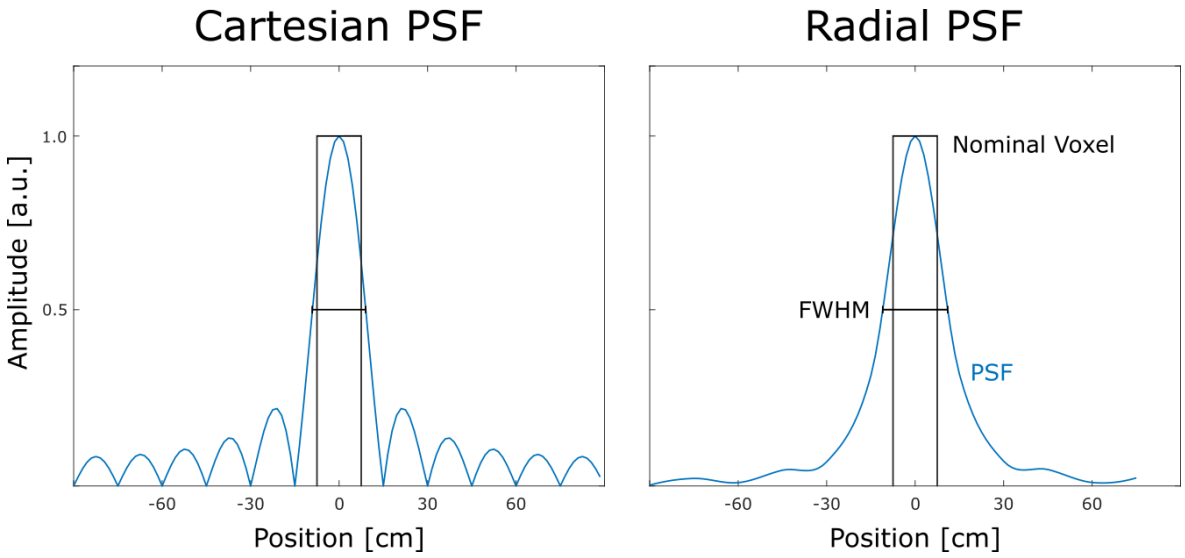


Figure 57: Comparison of simulated point spread functions (PSFs) of the EPSI with Cartesian (left) and radial sampling (right) along one dimension. The black rectangle indicates the nominal voxel, while the blue PSF displays the actual signal distribution.

The effective voxel size then corresponds to the FWHM of the shown signal distributions in 3D, which yields an almost 1.5-times larger voxel for the rEPSI compared to the Cartesian EPSI. Note that for the Cartesian version, no filter was applied, while for the rEPSI the gridding reconstruction was used (see Section 3.3.3). During the gridding algorithm, the $k$-space data is filtered through a Kaiser-Bessel function, what leads to an increased main lobe and suppressed sidelobes of the PSF.

# D. Singular Values of the In Vivo Denoising

In Figure 58, the trace entries of $S$ are plotted, which consists out of the singular values of the evaluated FID data. Extraction followed eq. (62) and was applied via the singular value decomposition function of MATLAB.

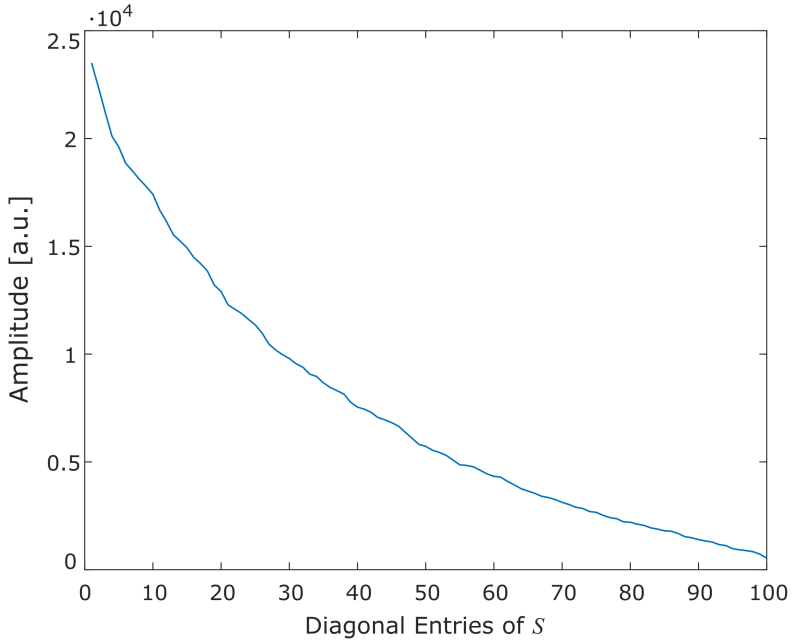


Figure 58: Amplitude of the singular values after decomposition of the FID data from the in vivo $^{13}$C MRF acquisition.

The applied denoising rank was $r = 1$, meaning all entries of $S$ except the first one were set to zero. Since no sharp drop-off after this first value can be seen, this suggests non-redundant information is being discarded. This was expected, as the noise level was high and the total spectral information with all resonances of the lipids abundant. However, this low-rank denoising was deemed feasible, as it was only performed as a qualitative comparison in context of the MRF stability in vivo. Higher denoising ranks could not achieve a sufficient improvement of the spectral information.

# List of Figures

# List of Tables

# List of Publications

In the following, a list of all my own scientific contributions is provided.
All publications whose content has been used in this thesis are marked with *.

## Journal Articles

*Awenius M, Abeln H, Müller M, Franke VL, Rincon GG, Glowa C, Schmitt M, Bangert R, Ludwig D, Schmidt AB, Kuder TA, Ladd ME, Bachert P, Biegger P, Korzowski A. "Three-Dimensional Radial Echo-Planar Spectroscopic Imaging for Hyperpolarized $^{13}$C MRSI In Vivo." *Magnetic Resonance in Medicine* 93.1 (2025): 31-41.

Wang Z, Grashei M, Fischer J, Sühnel S, Setzer N, Awenius M, Korzowski A, Özen AC, Zaitsev M, Bock M, Schilling F, Schmidt AB, Müller CA. "Radial Multi-Echo bSSFP and IDEAL Chemical Shift Separation in $k$-Space for High-Speed 3D Hyperpolarized $^{13}$C Metabolic MRI." *Magnetic Resonance in Medicine* 94.5 (2025): 2190-2200.

## Conference

Wang Z, Müller CA, Fischer J, Grashei M, Sühnel S, Setzer N, Schilling F, Awenius M, Korzowski A, Özen AC, Zaitsev M, Bock M, Schmidt AB. "Fast 3D Hyperpolarized Carbon-13 Metabolic MRI with Enhanced Spatio-Temporal Resolution using Radial Multi-Echo bSSFP and PSF Optimization." *Proceedings of the 33rd Annual Meeting of the ISMRM* (2025)

Wang Z, Müller CA, Fischer J, Grashei M, Sühnel S, Setzer N, Schilling F, Awenius M, Korzowski A, Özen AC, Zaitsev M, Bock M, Schmidt AB. "Fast 3D Hyperpolarized Carbon-13 Metabolic MRI with Enhanced Spatio-Temporal Resolution using Radial Multi-Echo bSSFP." *Proceedings of the 20th Annual Meeting of the EMIM* (2025)

*Awenius M, Abeln H, Müller M, Biegger P, Schmitt M, Bangert R, Rincon GG, Schmidt AB, Ladd ME, Bachert P, Korzowski A. "Three-Dimensional MRSI of Hyperpolarized [1,2-13C]Pyruvate In Vivo by Means of Radial EPSI at 3 T." *Proceedings of the 19th Annual Meeting of the EMIM* (2024)

*Rincon GG, Awenius M, Abeln H, Biegger P, Müller M, Franke VL, Schmidt AB, Ladd ME, Bachert P, Korzowski A. "GAGA: Gapped Arrangement of Golden Angles for Sliding Window Reconstruction of Hyperpolarized Dynamic $^{13}$C MRSI Data Acquired with 3D Radial EPSI." *Proceedings of the 32nd Annual Meeting of the ISMRM* (2024)

*Rincon GG, Awenius M, Abeln H, Biegger P, Müller M, Franke VL, Schmidt AB, Ladd ME, Bachert P, Korzowski A. "GAGA: Gapped Arrangement of Golden Angles for Sliding Window Reconstruction of Hyperpolarized Dynamic $^{13}$C MRSI Data Acquired with 3D Radial EPSI." *Proceedings of the 19th Annual Meeting of the EMIM* (2024)

Wang Z, Grashei M, Fischer J, Sühnel S, Setzer N, Awenius M, Korzowski A, Zaitsev M, Bock M, Schilling F, Schmidt AB, Müller CA. "Hyperpolarized 13C 3D MRSI using Radial Multi-echo bSSFP and k-Space-Based IDEAL." *Proceedings of the 32nd Annual Meeting of the ISMRM* (2024)

Wang Z, Grashei M, Fischer J, Sühnel S, Setzer N, Awenius M, Korzowski A, Zaitsev M, Bock M, Schilling F, Schmidt AB, Müller CA. "Radial and Cartesian Multi-Echo bSSFP for Hyperpolarized $^{13}$C 3D Metabolic MRI." *Proceedings of the 19th Annual Meeting of the EMIM* (2024)

*Awenius M, Biegger P, Glowa C, Müller M, Bangert R, Abeln H, Ludwig D, Kuder TA, Ladd ME, Bachert P, Korzowski A. "Three-Dimensional Radial Echo-Planar Spectroscopic Imaging for In Vivo Hyperpolarized $^{13}$C MRSI at 3 T." *Proceedings of the 31st Annual Meeting of the ISMRM* (2023)

# References


[1] T. E. Yankeelov, D. R. Pickens, and R. R. Price, *Quantitative MRI in Cancer*. Taylor & Francis, 2011.

[2] W. Gerlach and O. Stern, "Der Experimentelle Nachweis der Richtungsquantelung im Magnetfeld," *Zeitschrift für Physik*, vol. 9, no. 1, pp. 349–352, 1922.

[3] I. I. Rabi, J. R. Zacharias, S. Millman, and P. Kusch, "A New Method of Measuring Nuclear Magnetic Moment," *Physical Review*, vol. 53, no. 4, p. 318, 1938.

[4] F. Bloch, "Nuclear Induction," *Physical Review*, vol. 70, no. 7-8, p. 460, 1946.

[5] E. M. Purcell, H. C. Torrey, and R. V. Pound, "Resonance Absorption by Nuclear Magnetic Moments in a Solid," *Physical Review*, vol. 69, no. 1-2, p. 37, 1946.

[6] W. Proctor and F. Yu, "The Dependence of a Nuclear Magnetic Resonance Frequency upon Chemical Compound," *Physical Review*, vol. 77, no. 5, p. 717, 1950.

[7] W. Dickinson, "Dependence of the F 19 Nuclear Resonance Position on Chemical Compound," *Physical Review*, vol. 77, no. 5, p. 736, 1950.

[8] R. A. De Graaf, *In Vivo NMR Spectroscopy: Principles and Techniques*. John Wiley & Sons, 2019.

[9] P. Mansfield and P. K. Grannell, "NMR 'Diffraction' in Solids?," *Journal of Physics C: Solid State Physics*, vol. 6, no. 22, p. L422, 1973.

[10] K. R. Keshari and D. M. Wilson, "Chemistry and Biochemistry of 13C Hyperpolarized Magnetic Resonance Using Dynamic Nuclear Polarization," *Chemical Society Reviews*, vol. 43, no. 5, pp. 1627–1659, 2014.

[11] J. Kurhanewicz, D. B. Vigneron, K. Brindle, E. Y. Chekmenev, A. Comment, C. H. Cunningham, R. J. DeBerardinis, G. G. Green, M. O. Leach, S. S. Rajan, *et al.*, "Analysis of Cancer Metabolism by Imaging Hyperpolarized Nuclei: Prospects for Translation to Clinical Research," *Neoplasia*, vol. 13, no. 2, pp. 81–97, 2011.

[12] A. W. Overhauser, "Paramagnetic Relaxation in Metals," *Physical Review*, vol. 89, no. 4, p. 689, 1953.

[13] C. P. Slichter, *Principles of Magnetic Resonance*, vol. 1. Springer Science & Business Media, 2013.

[14] J. H. Ardenkjær-Larsen, B. Fridlund, A. Gram, G. Hansson, L. Hansson, M. H. Lerche, R. Servin, M. Thaning, and K. Golman, "Increase in Signal-to-Noise ratio of $> 10,000$ times in Liquid-State NMR," *Proceedings of the National Academy of Sciences*, vol. 100, no. 18, pp. 10158–10163, 2003.

[15] S. J. Nelson, J. Kurhanewicz, D. B. Vigneron, P. E. Larson, A. L. Harzstark, M. Ferrone, M. Van Criekinge, J. W. Chang, R. Bok, I. Park, *et al.*, "Metabolic Imaging of Patients with Prostate Cancer Using Hyperpolarized [1-13C]Pyruvate," *Science Translational Medicine*, vol. 5, no. 198, pp. 198ra108–198ra108, 2013.

[16] J. W. Gordon, H.-Y. Chen, N. Dwork, S. Tang, and P. E. Larson, "Fast Imaging for Hyperpolarized MR Metabolic Imaging," *Journal of Magnetic Resonance Imaging*, vol. 53, no. 3, pp. 686–702, 2021.

[17] A. P. Chen, R. E. Hurd, M. A. Schroeder, A. Z. Lau, Y.-p. Gu, W. W. Lam, J. Barry, J. Tropp, and C. H. Cunningham, "Simultaneous Investigation of Cardiac Pyruvate Dehydrogenase Flux, Krebs Cycle Metabolism and pH, Using Hyperpolarized [1,2-13C2]Pyruvate In Vivo," *NMR in Biomedicine*, vol. 25, no. 2, pp. 305–311, 2012.

[18] S. Düwel, C. Hundshammer, M. Gersch, B. Feuerecker, K. Steiger, A. Buck, A. Walch, A. Haase, S. J. Glaser, M. Schwaiger, *et al.*, "Imaging of pH In Vivo Using Hyperpolarized 13C-Labelled Zymonic Acid," *Nature Communications*, vol. 8, no. 1, p. 15126, 2017.

[19] J. Y. Lau, B. J. Geraghty, A. P. Chen, and C. H. Cunningham, "Improved Tolerance to Off-Resonance in Spectral-Spatial EPI of Hyperpolarized [1-13C]Pyruvate and Metabolites," *Magnetic Resonance in Medicine*, vol. 80, no. 3, pp. 925–934, 2018.

[20] C. A. Müller, C. Hundshammer, M. Braeuer, J. G. Skinner, S. Berner, J. Leupold, S. Düwel, S. G. Nekolla, S. Månsson, A. E. Hansen, *et al.*, "Dynamic 2D and 3D Mapping of Hyperpolarized Pyruvate to Lactate Conversion In Vivo with Efficient Multi-Echo Balanced Steady-State Free Precession at 3 T," *NMR in Biomedicine*, vol. 33, no. 6, p. e4291, 2020.

[21] D. Ludwig, *Radially-Sampled 31P Echo-Planar Spectroscopic Imaging In Vivo at 7 T*. Master Thesis, 2017.

[22] G. Rincon, M. Awenius, H. Abeln, P. Biegger, M. Müller, V. Franke, A. B. Schmidt, M. E. Ladd, P. Bachert, and A. Korzowski, "GAGA: Gapped Arrange-

ment of Golden Angles for Sliding Window Reconstruction of Hyperpolarized Dynamic 13C MRSI Data Acquired with 3D Radial EPSI," in *ESMI: Proceedings of the 19th Annual Meeting of the EMIM*, 2024.

[23] J. d'Arcy, D. Collins, I. Rowland, A. Padhani, and M. Leach, "Applications of Sliding Window Reconstruction with Cartesian Sampling for Dynamic Contrast Enhanced MRI," *NMR in Biomedicine: An International Journal Devoted to the Development and Application of Magnetic Resonance In Vivo*, vol. 15, no. 2, pp. 174–183, 2002.

[24] Y. Xing, G. D. Reed, J. M. Pauly, A. B. Kerr, and P. E. Larson, "Optimal Variable Flip Angle Schemes for Dynamic Acquisition of Exchanging Hyperpolarized Substrates," *Journal of Magnetic Resonance*, vol. 234, pp. 75–81, 2013.

[25] Y. Jiang, D. Ma, N. Seiberlich, V. Gulani, and M. A. Griswold, "MR Fingerprinting Using Fast Imaging with Steady State Precession (FISP) with Spiral Readout," *Magnetic Resonance in Medicine*, vol. 74, no. 6, pp. 1621–1631, 2015.

[26] L. Hilaire, F. Wehrli, and H. Song, "High-Speed Spectroscopic Imaging for Cancellous Bone Marrow R2 Mapping and Lipid Quantification," *Magnetic Resonance Imaging*, vol. 18, no. 7, pp. 777–786, 2000.

[27] D. Ma, V. Gulani, N. Seiberlich, K. Liu, J. L. Sunshine, J. L. Duerk, and M. A. Griswold, "Magnetic Resonance Fingerprinting," *Nature*, vol. 495, no. 7440, pp. 187–192, 2013.

[28] M. Lutz, C. S. Aigner, S. Flassbeck, F. Krueger, C. G. Gatefait, C. Kolbitsch, B. Silemek, F. Seifert, T. Schaeffter, and S. Schmitter, "B1-MRF: Large Dynamic Range MRF-Based Absolute B1+ Mapping in the Human Body at 7 T," *Magnetic Resonance in Medicine*, vol. 92, no. 6, pp. 2473–2490, 2024.

[29] L. Vanhamme, A. van den Boogaart, and S. Van Huffel, "Improved Method for Accurate and Efficient Quantification of MRS Data with Use of Prior Knowledge," *Journal of Magnetic Resonance*, vol. 129, no. 1, pp. 35–43, 1997.

[30] M. H. Levitt, *Spin dynamics: Basics of Nuclear Magnetic Resonance*. John Wiley & Sons, 2008.

[31] T. Maly, G. T. Debelouchina, V. S. Bajaj, K.-N. Hu, C.-G. Joo, M. L. Mak-Jurkauskas, J. R. Sirigiri, P. C. Van Der Wel, J. Herzfeld, R. J. Temkin, *et al.*, "Dynamic Nuclear Polarization at High Magnetic Fields," *The Journal of Chemical Physics*, vol. 128, no. 5, p. 02B611, 2008.

[32] T. Can, Q. Ni, and R. Griffin, "Mechanisms of Dynamic Nuclear Polarization in Insulating Solids," *Journal of Magnetic Resonance*, vol. 253, pp. 23–35, 2015.

[33] J. M. Park, S. Josan, T. Grafendorfer, Y.-F. Yen, R. E. Hurd, D. M. Spielman, and D. Mayer, "Measuring Mitochondrial Metabolism in Rat Brain In Vivo using MR Spectroscopy of Hyperpolarized [2-13C]Pyruvate," *NMR in Biomedicine*, vol. 26, no. 10, pp. 1197–1203, 2013.

[34] P. E. Larson, J. M. Bernard, J. A. Bankson, N. Bøgh, R. A. Bok, A. P. Chen, C. H. Cunningham, J. W. Gordon, J.-B. Hövener, C. Laustsen, *et al.*, "Current Methods for Hyperpolarized [1-13C]Pyruvate MRI Human Studies," *Magnetic Resonance in Medicine*, vol. 91, no. 6, pp. 2204–2228, 2024.

[35] J. M. Berg, J. L. Tymoczko, G. J. Gatto jr., and L. Stryer, *Biochemie*. Springer Spektrum, 2018.

[36] O. Warburg, F. Wind, and E. Negelein, "The Metabolism of Tumors in the Body," *The Journal of General Physiology*, vol. 8, no. 6, p. 519, 1927.

[37] C. Tippareddy, W. Zhao, J. L. Sunshine, M. Griswold, D. Ma, and C. Badve, "Magnetic Resonance Fingerprinting: An Overview," *European Journal of Nuclear Medicine and Molecular Imaging*, vol. 48, no. 13, pp. 4189–4200, 2021.

[38] M. Widmaier, S.-I. Lim, D. Wenz, and L. Xin, "Fast In Vivo assay of Creatine Kinase Activity in the Human Brain by 31P Magnetic Resonance Fingerprinting," *NMR in Biomedicine*, vol. 36, no. 11, p. e4998, 2023.

[39] M. Chmelík, M. Považan, F. Jír, I. J. Kukurová, M. Dezortová, M. Krššák, W. Bogner, M. Hájek, S. Trattnig, and L. Valkovič, "Flip-Angle Mapping of 31P Coils by Steady-State MR Spectroscopic Imaging," *Journal of Magnetic Resonance Imaging*, vol. 40, no. 2, pp. 391–397, 2014.

[40] A. Panda, S. Jones, H. Stark, R. S. Raghavan, K. Sandrasegaran, N. Bansal, and U. Dydak, "Phosphorus Liver MRSI at 3 T Using a Novel Dual-Tuned Eight-Channel 31P/1H Coil," *Magnetic Resonance in Medicine*, vol. 68, no. 5, pp. 1346–1356, 2012.

[41] E. Insko and L. Bolinger, "Mapping of the Radiofrequency Field," *Journal of Magnetic Resonance, Series A*, vol. 103, no. 1, pp. 82–85, 1993.

[42] G. R. Morrell, "A Phase-Sensitive Method of Flip Angle Mapping," *Magnetic Resonance in Medicine: An Official Journal of the International Society for Magnetic Resonance in Medicine*, vol. 60, no. 4, pp. 889–894, 2008.

[43] R. Pohmann and K. Scheffler, "A Theoretical and Experimental Comparison of Different Techniques for B1 Mapping at very High Fields," *NMR in Biomedicine*, vol. 26, no. 3, pp. 265–275, 2013.

[44] J. Eills, M. Azagra, D. Gómez-Cabeza, M. C. Tayler, and I. Marco-Rius, "Polarization Losses from the Nonadiabatic Passage of Hyperpolarized Solutions through Metallic Components," *Journal of Magnetic Resonance Open*, vol. 18, p. 100144, 2024.

[45] S. Posse, C. DeCarli, and D. Le Bihan, "Three-Dimensional Echo-Planar MR Spectroscopic Imaging at Short Echo Times in the Human Brain.," *Radiology*, vol. 192, no. 3, pp. 733–738, 1994.

[46] H. Nyquist, "Certain Topics in Telegraph Transmission Theory," *Transactions of the American Institute of Electrical Engineers*, vol. 47, no. 2, pp. 617–644, 2009.

[47] J. D. O'Sullivan, "A Fast Sinc Function Gridding Algorithm for Fourier Inversion in Computer Tomography," *IEEE Transactions on Medical Imaging*, vol. 4, no. 4, pp. 200–207, 1985.

[48] J. I. Jackson, C. H. Meyer, D. G. Nishimura, and A. Macovski, "Selection of a Convolution Function for Fourier Inversion Using Gridding (Computerised Tomography Application)," *IEEE Transactions on Medical Imaging*, vol. 10, no. 3, pp. 473–478, 1991.

[49] P. J. Beatty, D. G. Nishimura, and J. M. Pauly, "Rapid Gridding Reconstruction with a Minimal Oversampling Ratio," *IEEE Transactions on Medical Imaging*, vol. 24, no. 6, pp. 799–808, 2005.

[50] Q. Guo, C. Zhang, Y. Zhang, and H. Liu, "An Efficient SVD-Based Method for Image Denoising," *IEEE transactions on Circuits and Systems for Video Technology*, vol. 26, no. 5, pp. 868–880, 2015.

[51] M. Awenius, *Implementation of Radial Echo-Planar Spectroscopic Imaging for Hyperpolarized 13C MRSI at 3 T.* Master Thesis, 2022.

[52] L. Ruhm, *31P Magnetic Resonance Spectroscopic Imaging of the Human Brain at 7 Tesla: Reproducibility of Metabolic Imaging.* Master Thesis, 2017.

[53] A. Korzowski, N. Weinfurtner, S. Mueller, J. Breitling, S. Goerke, H.-P. Schlemmer, M. E. Ladd, D. Paech, and P. Bachert, "Volumetric Mapping of Intra- and Extracellular pH in the Human Brain Using 31P MRSI at 7 T," *Magnetic Resonance in Medicine*, vol. 84, no. 4, pp. 1707–1723, 2020.

[54] M. Awenius, H. Abeln, M. Müller, V. L. Franke, G. Rincon, C. Glowa, M. Schmitt, R. Bangert, D. Ludwig, A. B. Schmidt, *et al.*, "Three-Dimensional Radial Echo-Planar Spectroscopic Imaging for Hyperpolarized 13C MRSI In Vivo," *Magnetic Resonance in Medicine*, vol. 93, no. 1, pp. 31–41, 2025.

[55] M. Awenius, H. Abeln, M. Müller, P. Biegger, M. Schmitt, R. Bangert, G. G. Rincon, A. B. Schmidt, M. E. Ladd, P. Bachert, and A. Korzowski, "Three-Dimensional MRSI of Hyperpolarized [1,2-13C]Pyruvate In Vivo by Means of Radial EPSI at 3 T," in *ESMI: Proceedings of the 19th Annual Meeting of the EMIM*, 2024.

[56] Z. J. Wang, M. A. Ohliger, P. E. Larson, J. W. Gordon, R. A. Bok, J. Slater, J. E. Villanueva-Meyer, C. P. Hess, J. Kurhanewicz, and D. B. Vigneron, "Hyperpolarized 13C MRI: State of the Art and Future Directions," *Radiology*, vol. 291, no. 2, pp. 273–284, 2019.

[57] C.-Y. Hsieh, Y.-C. Lai, K.-Y. Lu, and G. Lin, "Advancements, Challenges, and Future Prospects in Clinical Hyperpolarized Magnetic Resonance Imaging: A Comprehensive Review," *Biomedical Journal*, vol. 48, no. 3, p. 100802, 2025.

[58] Y.-F. Yen, S. Kohler, A. Chen, J. Tropp, R. Bok, J. Wolber, M. Albers, K. Gram, M. Zierhut, I. Park, *et al.*, "Imaging Considerations for In Vivo 13C Metabolic Mapping Using Hyperpolarized 13C-Pyruvate," *Magnetic Resonance in Medicine: An Official Journal of the International Society for Magnetic Resonance in Medicine*, vol. 62, no. 1, pp. 1–10, 2009.

[59] R. Chowdhury, C. A. Mueller, L. Smith, F. Gong, M.-V. Papoutsaki, H. Rogers, T. Syer, S. Singh, G. Brembilla, A. Retter, *et al.*, "Quantification of Prostate Cancer Metabolism Using 3D Multiecho bSSFP and Hyperpolarized [1-13C]Pyruvate: Metabolism Differs between Tumors of the Same Gleason Grade," *Journal of Magnetic Resonance Imaging*, vol. 57, no. 6, pp. 1865–1875, 2023.

[60] H.-Y. Chen, P. E. Larson, J. W. Gordon, R. A. Bok, M. Ferrone, M. van Criekinge, L. Carvajal, P. Cao, J. M. Pauly, A. B. Kerr, *et al.*, "Technique Development of 3D Dynamic CS-EPSI for Hyperpolarized 13C Pyruvate MR Molecular Imaging of Human Prostate Cancer," *Magnetic Resonance in Medicine*, vol. 80, no. 5, pp. 2062–2072, 2018.

[61] M. S. Ramirez, J. Lee, C. M. Walker, V. C. Sandulache, F. Hennel, S. Y. Lai, and J. A. Bankson, "Radial Spectroscopic MRI of Hyperpolarized [1-13C]Pyruvate at 7 Tesla," *Magnetic Resonance in Medicine*, vol. 72, no. 4, pp. 986–995, 2014.

[62] D. Mayer, Y. S. Levin, R. E. Hurd, G. H. Glover, and D. M. Spielman, "Fast Metabolic Imaging of Systems with Sparse Spectra: Application for Hyperpolarized 13C Imaging," *Magnetic Resonance in Medicine: An Official Journal of the International Society for Magnetic Resonance in Medicine*, vol. 56, no. 4, pp. 932–937, 2006.

[63] M. Durst, U. Koellisch, A. Frank, G. Rancan, C. V. Gringeri, V. Karas, F. Wiesinger, M. I. Menzel, M. Schwaiger, A. Haase, *et al.*, "Comparison of Acquisition Schemes for Hyperpolarised 13C Imaging," *NMR in Biomedicine*, vol. 28, no. 6, pp. 715–725, 2015.

[64] W. Jiang, M. Lustig, and P. E. Larson, "Concentric Rings k-Space Trajectory for Hyperpolarized 13C MR Spectroscopic Imaging," *Magnetic resonance in medicine*, vol. 75, no. 1, pp. 19–31, 2016.

[65] M. Grashei, P. Wodtke, J. G. Skinner, S. Sühnel, N. Setzer, T. Metzler, S. Gulde, M. Park, D. Witt, H. Mohr, *et al.*, "Simultaneous Magnetic Resonance Imaging of pH, Perfusion and Renal Filtration Using Hyperpolarized 13C-Labelled Z-OMPD," *Nature Communications*, vol. 14, no. 1, p. 5060, 2023.

[66] A. P. Chen, A. Z. Lau, Y.-p. Gu, M. A. Schroeder, J. Barry, and C. H. Cunningham, "Probing the Cardiac Malate–Aspartate Shuttle Non-Invasively Using Hyperpolarized [1,2-13C2]Pyruvate," *NMR in Biomedicine*, vol. 31, no. 1, p. e3845, 2018.

[67] F. A. Gallagher, M. I. Kettunen, and K. M. Brindle, "Imaging pH with Hyperpolarized 13C," *NMR in Biomedicine*, vol. 24, no. 8, pp. 1006–1015, 2011.

[68] S. Winkelmann, T. Schaeffter, T. Koehler, H. Eggers, and O. Doessel, "An optimal Radial Profile Order Based on the Golden Ratio for Time-Resolved MRI," vol. 26, no. 1, pp. 68–76, 2006.

[69] C. Laustsen, S. Ringgard, H. Birn, M. Pedersen, and J. Ardenkjaef-Larsen, "Radial Golden Angle Fast Spin Echo: a Hyperpolarized 13C Multi Contrast Method," in *Proceedings of the 21st Annual Meeting of ISMRM*, p. 1928, 2013.

[70] E. J. Candes and Y. Plan, "A Probabilistic and RIPless Theory of Compressed Sensing," *IEEE Transactions on Information Theory*, vol. 57, no. 11, pp. 7235–7254, 2011.

[71] S. Ogawa, T.-M. Lee, A. R. Kay, and D. W. Tank, "Brain Magnetic Resonance Imaging with Contrast Dependent on Blood Oxygenation," *proceedings of the National Academy of Sciences*, vol. 87, no. 24, pp. 9868–9872, 1990.

[72] S. E. Day, M. I. Kettunen, M. K. Cherukuri, J. B. Mitchell, M. J. Lizak, H. D. Morris, S. Matsumoto, A. P. Koretsky, and K. M. Brindle, "Detecting Response of Rat C6 Glioma Tumors to Radiotherapy Using Hyperpolarized [1-13C]Pyruvate and 13C Magnetic Resonance Spectroscopic Imaging," *Magnetic Resonance in Medicine*, vol. 65, no. 2, pp. 557–563, 2011.

[73] I. Park, P. E. Larson, M. L. Zierhut, S. Hu, R. Bok, T. Ozawa, J. Kurhanewicz, D. B. Vigneron, S. R. VandenBerg, C. D. James, *et al.*, "Hyperpolarized 13C Magnetic Resonance Metabolic Imaging: Application to Brain Tumors," *Neuro-Oncology*, vol. 12, no. 2, pp. 133–144, 2010.

[74] K. Golman, R. in 't Zandt, and M. Thaning, "Real-Time Metabolic Imaging," *Proceedings of the National Academy of Sciences*, vol. 103, no. 30, pp. 11270–11275, 2006.

[75] M. Marjańska, I. Iltis, A. A. Shestov, D. K. Deelchand, C. Nelson, K. Uğurbil, and P.-G. Henry, "In Vivo 13C Spectroscopy in the Rat Brain Using Hyperpolarized [1-13C]Pyruvate and [2-13C]Pyruvate," *Journal of Magnetic Resonance*, vol. 206, no. 2, pp. 210–218, 2010.

[76] S. Kohler, Y. Yen, J. Wolber, A. Chen, M. Albers, R. Bok, V. Zhang, J. Tropp, S. Nelson, D. Vigneron, *et al.*, "In vivo 13carbon metabolic imaging at 3t with hyperpolarized 13c-1-pyruvate," *Magnetic Resonance in Medicine: An Official Journal of the International Society for Magnetic Resonance in Medicine*, vol. 58, no. 1, pp. 65–69, 2007.

[77] "Probing Early Tumor Response to Radiation Therapy Using Hyperpolarized [1-13C]Pyruvate in MDA-MB-231 Xenografts, author=Chen, Albert P and Chu, William and Gu, Yi-Ping and Cunnhingham, Charles H," *PLoS One*, vol. 8, no. 2, p. e56551, 2013.

[78] K. Saito, S. Matsumoto, Y. Takakusagi, M. Matsuo, H. D. Morris, M. J. Lizak, J. P. Munasinghe, N. Devasahayam, S. Subramanian, J. B. Mitchell, *et al.*, "13C-MR Spectroscopic Imaging with Hyperpolarized [1-13C]Pyruvate Detects Early Response to Radiotherapy in SCC Tumors and HT-29 Tumors," *Clinical Cancer Research*, vol. 21, no. 22, pp. 5073–5081, 2015.

[79] M. T. Huynh, Z. Erfani, Z. Kovács, and J. M. Park, "Hyperpolarized [2-13C, 3-2H3]Pyruvate Detects Hepatic Gluconeogenesis In Vivo," *ACS Sensors*, vol. 9, no. 6, pp. 2801–2805, 2024.

[80] B. T. Chung, H.-Y. Chen, J. Gordon, D. Mammoli, R. Sriram, A. W. Autry, L. M. Le Page, M. M. Chaumeil, P. Shin, J. Slater, *et al.*, "First Hyperpolarized [2-13C]Pyruvate MR Studies of Human Brain Metabolism," *Journal of Magnetic Resonance*, vol. 309, p. 106617, 2019.

[81] I. Hancu, R. Watkins, S. J. Kohler, and R. P. Mallozzi, "Accurate Flip-Angle Calibration for 13C MRI," *Magnetic Resonance in Medicine: An Official Journal of the International Society for Magnetic Resonance in Medicine*, vol. 58, no. 1, pp. 128–133, 2007.

[82] R. F. Schulte, L. Sacolick, M. H. Deppe, M. A. Janich, M. Schwaiger, J. M. Wild, and F. Wiesinger, "Transmit Gain Calibration for Nonproton MR Using the Bloch–Siegert Shift," *NMR in Biomedicine*, vol. 24, no. 9, pp. 1068–1072, 2011.

[83] A. Z. Lau, A. P. Chen, and C. H. Cunningham, "Integrated Bloch-Siegert B1 Mapping and Multislice Imaging of Hyperpolarized 13C Pyruvate and Bicarbonate in the Heart," *Magnetic Resonance in Medicine*, vol. 67, no. 1, pp. 62–71, 2012.

[84] G. Giovannetti, F. Frijia, A. Flori, D. De Marchi, G. D. Aquaro, L. Menichetti, and J. H. Ardenkjaer-Larsen, "A Fast and Simple Method for Calibrating the Flip Angle in Hyperpolarized 13C MRS Experiments," *Concepts in Magnetic Resonance Part B: Magnetic Resonance Engineering*, vol. 45, no. 2, pp. 78–84, 2015.

[85] A. Bennett Haller, X. Liu, A. Sinha, S. Sahin, P. E. Larson, and C. Y. Wang, "A Flexible MRF Approach to Improve Kinetic Rate Estimation with bSSFP-Based Hyperpolarized [1-13C]Pyruvate MRI," *Magnetic Resonance in Medicine*, vol. 93, no. 6, pp. 2263–2277, 2025.

[86] C. Hundshammer, S. Düwel, and F. Schilling, "Imaging of Extracellular pH Using Hyperpolarized Molecules," *Israel Journal of Chemistry*, vol. 57, no. 9, pp. 788–799, 2017.

[87] M. S. Widmaier, A. Kaiser, S. Baup, D. Wenz, K. Pierzchała, Y. Xiao, Z. Huang, Y. Jiang, and L. Xin, "Fast 3D 31P B1+ Mapping with a Weighted Stack of Spiral Trajectory at 7 T," *Magnetic Resonance in Medicine*, vol. 93, no. 2, pp. 481–489, 2025.

# Acknowledgments - Danksagungen

Ich möchte mich ganz herzlich bei allen bedanken, die mich im Laufe meiner Promotion unterstützt haben.

Ich danke Ihnen, Prof. Ladd, dafür, dass Sie mir die Möglichkeit gegeben haben in Ihrer Abteilung zu forschen und für Ihren Rat in den TAC Meetings.
Ich danke Ihnen, Prof. Schröder, dass Sie sich die Zeit genommen haben mein Zweitgutachter zu sein und ebenfalls für Ihre Unterstützung als TAC Mitglied.
Ich danke Ihnen, Prof. Bachert, dass Sie mich schon im Bachelor für die medizinische Physik begeistert haben und so den Grundstein meiner wissenschaftlichen Karriere legten.

Ich danke dir, Andi, für alles. Ohne dich wäre ich sicher im $k$-Space verloren gegangen. Deine Begeisterung für die Wissenschaft motiviert so unglaublich und mit dir zu forschen macht einfach Spaß. Ich kann nicht beschreiben, wie dankbar ich für deine Hilfe bin. Danke!

Für all die zahllosen Stunden bei der Durchführung von Hyper-Experimenten danke ich dem gesamten Hyper-Team:
Helen, Philipp, Melanie, Renate, Alex, Anton und Gino. Auch wenn die Geräte es uns schwer gemacht haben, hatte ich immer Spaß mit euch zusammen zu hypern.
Natürlich danke ich auch der kompletten SpectroCESTler-Gruppe, mit der besten Dynamik, die man sich wünschen kann:
Vanessa, Justyna, Jan-Philipp und Bela, als Spectro-Team.
Philip, Flo, Petr, Neele, Jannis und Jana, als CEST-Team.
Und auch Julian aus der Diffusionsgruppe.

Nochmal ganz besonders möchte ich Helen und Justyna danken. Gerade die finale Zeit habt ihr, auch wenn es anstrengend war, wirklich verschönert.

Ich danke meinen Eltern. Ihr steht immer hinter mir und ohne euch wäre ich sicher nie so weit gekommen. Ich hab euch lieb.
Auch danke ich allen Freunden, die mich in der Zeit begleitet haben.
Maja, ich danke dir von ganzem Herzen. Ich liebe dich.